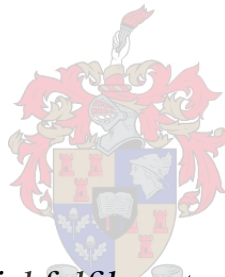


Three Phase Rotary Transformer for a Rotor Tied Doubly fed Induction Machine

by

Stefan Botha



*Thesis presented in partial fulfilment of the requirements for the
degree of Master of engineering in the Faculty of Engineering
at Stellenbosch University*

Supervisor:

Dr N. Gule

April 2022

Declaration

By submitting this thesis electronically, I declare that the entirety of the work contained therein is my own, original work, that I am the sole author thereof (save to the extent explicitly otherwise stated), that reproduction and publication thereof by Stellenbosch University will not infringe any third party rights and that I have not previously in its entirety or in part submitted it for obtaining any qualification.

Date:April 2022.....

Copyright © 2022 Stellenbosch University
All rights reserved.

Abstract

With the rising demand for renewable energy sources, wind energy has emerged as a very popular alternative to the use of fossil fuels. The growth in this sector has led to an increased emphasis on the reliability of the generating units. The most widely used generator in wind turbines is the doubly fed induction generator (DFIG). Its advantages such as variable speed makes it well suited. The brushless doubly fed induction generator (BDFIG) offers superior reliability due to the replacement of the slip ring assemblies from the standard DFIG. The current employed BDFIG topology results in a more complex machine. In order to retain the simplicity that the DFIG offers, other brushless topologies have to be explored.

The rotor-tied, rotary transformer (RT) is one of the proposed alternative topologies. It can be utilized with a standard DFIG and retain the simplicity of the machine. The purpose of this study is to determine the effectiveness of the topology when utilized with a rotor-tied DFIG (RDFIG). The study aims to develop a design methodology that considers the unique layout of the RT, while optimizing the RT for efficiency and minimizing size. An analytical model is used in conjunction with finite element analysis (FEA) to improve on the design while taking into account the non-idealistic nature of the RT.

A prototype RT is designed using the proposed analytical model, constructed and practically tested. The resultant efficiency is higher at a smaller size a prototypes built with conventional transformer design. The RT is tested and compares favorably against the FEA and analytical models. It is able to exceed its design rating for short periods but cooling is a limiting factor. The proposed RT is then tested rotor-tied to a RDFIG, and the RT enables the RDFIG to operate without a slip ring and brush assembly. The proposed RT-RDFIG was able to maintain high levels of efficiency and proves that the solution could be viable.

Uittreksel

Met die toenemende vraag na hernubare energiebronne, het windenergie na vore gekom as 'n baie gewilde alternatief vir die gebruik van fossielbrandstowwe. Die groei in hierdie sektor het gelei tot 'n groter klem op die betroubaarheid van die opwekkingseenhede. Die mees gebruikte kragopwekker in windturbines is die dubbel gevoede induksie generator (DGIG). Sy voordele soos veranderlike spoed maak dit goed geskik. Die borsellose dubbel gevoede induksie generator (BDGIG) bied hoer betroubaarheid as gevolg van die vervanging van die sleepring en borsels van die standaard DGIG. Die huidige aangewende BDFIG-topologie lei tot 'n meer komplekse masjien. Om die eenvoud wat die DFIG bied te behou, moet ander borsellose topologieë ondersoek word.

Die rotorgebonde roterende transformator (RT), is een van die voorgestelde alternatiewe topologieë. Dit kan met 'n standaard DGIG gebruik word en behou die eenvoudigheid van die masjien. Die doel van hierdie studie is om die doeltreffendheid van die topologie te bepaal wanneer dit gebruik word met 'n rotor-gebinde DGIG (RDGIG). Die studie mik om 'n ontwerpmetodologie te ontwikkel wat die unieke uitleg van die RT in ag neem, terwyl die RT geoptimaliseer word vir doeltreffendheid en om grootte te minimaliseer. 'n Analitiese model word saam met eindige element analise (EEA) gebruik om die ontwerp te verbeter terwyl die nie-idealitiese aard van die RT in ag geneem word.

'n Prototipe RT word ontwerp deur die voorgestelde analitiese model te gebruik, en is gebou en prakties getoets. Die gevolglike doeltreffendheid is hoër by 'n kleiner grootte as 'n prototipe wat met konvensionele transformator ontwerp gebou is. Die RT word getoets en vergelyk gunstig met die EEA en analitiese modelle. Dit is in staat om sy ontwerpgradering vir kort tydperke te oorskry, maar verkoeling is 'n beperkende faktor. Die voorgestelde RT word dan getoets rotor-gebind aan 'n RDGIG, en die RT stel die RDFIG in staat om sonder 'n sleepring en borsel samestelling te werk. Die voorgestelde RT-RDGIG was in staat om hoër vlakke van doeltreffendheid te handhaaf en bewys dat die oplossing lewensvatbaar kan wees.

Acknowledgments

I would like to thank the following people for their contributions to the project:

- My supervisor, Dr. Nathie Gule, for his support and guidance throughout the project.
- My parents and family, for their continuous emotional and financial support.
- My EMLab colleagues for their advice, support and friendship.
- Mr Pietro Petzer, Andre Swart, Howard Koopman, Andrew Loubser and Keanan for their assistance during the construction of the prototype, equipment setup and testing.

Contents

Declaration	ii
Abstract	iii
Uittreksel	iv
Acknowledgments	v
Contents	vi
List of Figures	x
List of Tables	xiv
Nomenclature	xviii
1 Introduction	1
1.1. Literature review	4
1.1.1. Brushless doubly fed induction generator	4
1.1.2. Synchronous generators with fully rated converter	5
1.1.3. The brushless doubly fed reluctance generator	6
1.1.4. The rotor-tied DFIG	6
1.1.5. DFIG with rotary transformer	7
1.1.6. Rotary transformer implementations	8
1.2. Research objectives	11
2 Rotary transformer design considerations	13
2.1. RT topology configuration	13
2.2. Power rating	16
2.3. Winding configuration	17
2.4. Operating frequency and size	18
2.5. Losses in a RT	20
2.6. Efficiency	21
2.8. The air gap	22
2.9. Rotational effects	24

2.10. Rotor cooling	25
2.11. Summary	25
3 Three-phase RT design methodology	27
3.1. Transformer design and loading parameters	29
3.2. Single phase transformer equivalent model	31
3.2.1. Winding resistances	32
3.2.2. Single phase RT Inductances	33
3.2.2.1. Magnetizing inductance	33
3.2.2.2. Axial air gap RT reluctance model	35
3.2.2.3. Fill factor correction for radially laminated cores	37
3.2.2.4. Leakage inductance	40
3.3. Single phase RT core configurations	40
3.3.1. Radially laminated single phase core dimensions	40
3.3.2. Combined lamination core dimensions	43
3.4. Three-phase RT core configurations	46
3.4.1. Three single phase RT's in a three-phase system	46
3.4.2. Single core RT with three-phase windings	46
3.5. Material selection	48
3.5.1. Lamination selection	48
3.5.2. Winding material	50
3.6. Core loss model for the three-phase RT	51
3.7. Thermal design	52
3.7.1. Natural convection	52
3.7.2. Radiation heat transfer	53
3.7.2. Radiation heat transfer	53
3.7.4. Internal forced convection	54
3.7.5. Combined heat transfer	55
3.8. Vibration	57
3.8.1. Rotating unbalance	57
3.8.2. Natural and induced resonance	58
3.8.3. Noise	58
3.8.4. Air gap harmonics	59
3.9. Mechanical stability	59
3.10. Summary	60
4 Design and FEA analysis of a 6kVA three-phase RT	63
4.1. RT design outline and requirements	63
4.2. Single phase 2kVA RT design and analysis	64
4.2.1. Single phase design dimensions and parameters	64
4.2.2. Single phase 2D analysis	64
4.2.3. 3D Analysis of the single phase radially laminated RT	68
4.2.3.1. 3D Model without filler laminations	68
4.2.3.2. 3D Model with filler laminations	69

4.2.4. Rolled and stacked lamination layout	71
4.2.5. Comparison of the different single phase FEA models	73
4.3. Three-phase 6kVA RT design and analysis	75
4.3.1. Shared inner limb three-phase RT	76
4.3.2. Separated limb three-phase RT	77
4.3.3. Comparison and model selection of the three-phase RT	78
4.4. Three-phase RT mechanical design	81
4.4.1. Material selection	81
4.4.2. Layout and assembly of the RT	82
4.5. Summary	83
5 Prototype manufacturing	85
5.1. Primary (rotor) portion of the RT	86
5.2. Secondary (stator) portion of the RT	89
5.3. Full assembly of the RT	91
5.4. Summary	92
6 Three-phase RT measurements	94
6.1. Rotary transformer no-load tests	95
6.1.1 Resistance and Inductance tests	95
6.1.2. Open circuit tests	97
6.1.3. Short circuit tests	102
6.2. Full load RT testing	105
6.3. RDFIG coupling tests	110
6.3.1. RDFIG no-load and blocked rotor tests	110
6.3.2. RDFIG equivalent circuit parameters	111
6.3.3. RDFIG load tests	113
6.4. Thermal results	116
6.5. Summary	118
7 Conclusion	119
Bibliography	121
A Transformer equations	126
A.1. General transformer theory	126
A.2. Inductance of a transformer	127
A.2.1. Magnetizing inductance	127
A.2.1. Leakage inductance	128
B RT coupled RDFIG	130
B.1. RDFIG testing procedure	130
B.2. RDFIG parameter calculations	131
C Thermal design	133

<i>CONTENTS</i>	ix
C.1. Natural convection	133
C.2. Radiation heat transfer	133
C.3. Internal forced convection	134
D RDFIG vs conventional DFIG operation	136
E Mechanical drawings	140

List of Figures

1.1	Wind installations by country.	1
1.2	Current wind turbine generator topologies	3
1.3	Slip rings with brushes vs brushless topology	8
1.4	Combination of axially and radially laminated core	9
1.5	Combination of axially and radially laminated core	10
1.6	Proposed CET solution for brushless SG	10
2.1	The two core topologies: (a) Radial and (c) Axial air gap. The flux path through the core is shown in (b) and (d).	14
2.2	Three-phase configuration with radial air gap stacked along on the shaft	15
2.3	Three-phase RT with a single shared core in the (a) Radial air gap, and (b) Axial air gap configuration	15
2.4	The winding layout for the radial air gap topology: (a) Adjacent and (b) Coaxial, and the axial air gap topology: (c) Adjacent and (d) Coaxial	17
2.5	Space in the nacelle of a wind turbine	19
2.6	Axial lamination spacing due to different diameters	19
2.7	Eddy currents in a solid core vs laminated core	20
2.8	The hysteresis loop	21
2.9	Efficiencies of the standard transformer and RT as a function of output power	21
2.10	BH curve for a transformer with no air gap and one with a 0.07mm air gap	23
2.11	The effect that the air gap has on (a) Magnetizing inductance, (b) Primary leakage inductance and (c) Secondary leakage	23
2.12	(a) Magnetizing inductance and (b) Leakage inductance of the RT as a function of air gap distance for the three-phase, radially laminated, 6kVA RT	24
2.13	Effect of rotation on (a) Magnetising and (b) Leakage inductance	24
3.1	Iron and copper losses at different frequencies and their corresponding optimal flux densities	28
3.2	Flow chart illustrating the initial RT design outline	30
3.3	Reluctance model for single phase shell type rotary transformer	31

<i>LIST OF FIGURES</i>	xi
3.4 Equivalent single phase electrical circuit for RT	32
3.5 Axis-symmetrical reluctance model of the single phase (a) Axial air gap RT and (b) Radial air gap RT	34
3.6 Representation of the flux path in the RT. (a) 3D section of the core indicating the flux path (1),(3) parallel to the shaft and (2) radial path across the air gap and (b) 2D cross section of flux path (2).	35
3.7 The decreasing fill factor of the laminations on the rotor for the radially stacked RT	38
3.8 Flux vector plot of the radially stacked core (a) Without filler laminations and (b) With filler laminations	39
3.9 Geometry of the axial air gap single-phase RT with adjacent windings	41
3.10 The outer dimensions of a 1.2kVA single phase RT with the change in shaft diameter	42
3.11 Proposed three-phase Rt with combined laminations	43
3.12 Geometry of the axial air gap RT with combined rolled and stacked laminations, in the adjacent winding topology	44
3.13 Three-phase configuration of single-phase RTs with radial air gap stacked along on the shaft	46
3.14 Three-phase configuration of single-phase RTs with axial air gap stacked along on the shaft	47
3.15 Three-phase RT with a single shared core in the (a) Radial air gap, and (b) Axial air gap configuration	47
3.16 M400-50A electrical steel (a) Flux density vs field intensity, (b) Relative permeability vs flux density	49
3.17 Thermal resistance model	55
3.18 Thermal analysis method	56
3.19 Rotating unbalance of a 0.5kg material loss on one side of the rotor of the RT vs speed	58
3.20 Flow chart illustrating the final RT design outline	61
4.1 The layout of the single phase axial air gap RT with adjacent windings	65
4.2 Flux distribution in the RT during a axis-symmetric 2D analysis .	66
4.3 Voltage and current waveforms for the open circuit 2D model . .	67
4.4 Flux distribution in the radially stacked RT without filler laminations during a 3D analysis	68
4.5 Lamination size difference for the rotor (a) and rotor filler (b) lamination	69
4.6 Flux distribution in the RT with filler laminations during a 3D analysis	70
4.7 Flux in the air gap for RT (a) Without filler laminations and (b) With filler laminations	71
4.8 3D representation of the rolled and stacked RT	72

4.9	Flux density of the rolled and stacked design during an axis-symmetric analysis	72
4.10	Magnetizing currents of the radial RT with and without filler laminations and the alternative configuration	73
4.11	External circuit parameters for ANSYS Maxwell	75
4.12	Primary lamination size for the shared limb configuration	76
4.13	Flux density plot of the shared limb radially stacked three-phase RT with filler laminations	76
4.14	Primary lamination size for the separated limb configuration	77
4.15	Flux density plot of the separated limb radially stacked three-phase RT with filler laminations	77
4.16	Magnetizing currents for the three-phase RT with and without the shared inner limb	78
4.17	The (a) Primary filler and (b) Secondary laminations for the separated limb, radially stacked, axial air gap three-phase RT	79
4.18	Primary and secondary voltage of the three-phase separate limb RT at maximum load with additional cooling	80
4.19	Primary and secondary current of the three-phase separate limb RT at maximum load with additional cooling	80
4.20	Three-phase RT connected to the DFIG shaft	81
4.21	Three-phase RT physical layout as mounted	83
5.1	(a) The stator assembly and (b) the rotor assembly	85
5.2	Cross-sectional view of the complete three-phase RT assembly	86
5.3	Laminations (a) Stator, (b) Rotor primary, (c) Rotor filler	87
5.4	Rotor filler lamination on primary lamination	88
5.5	(a) Rotor laminations without end plate, (b) Rotor laminations with end plate	88
5.6	Rotor during winding	88
5.7	Completed rotor	89
5.8	Stator without laminations test fitted onto rotor	90
5.9	Assembly of the stator (a) End plate and lamination end plate, (b) Stacked stator half, (c) Coil before cloth and resin, (d) The coils in one half of the stator	91
5.10	Complete assembly of the RT (a) Rotor in stator half, (b) Full assembly, (c) Inspection of the air gap, (d) RT mounted in testing	92
6.1	Single phase RT equivalent circuit	96
6.2	Equivalent test setup for the stationary open and short circuit RT tests	98
6.3	Equivalent per phase open circuit electrical model of the three-phase RT	98
6.4	Per phase open circuit magnetization curve	100

6.5	Measured and simulated phase voltage and current waveforms for phase A at no-load	101
6.6	The measured and simulated current waveforms at no-load	101
6.7	Open circuit output voltages	102
6.8	Short circuit equivalent circuit	103
6.9	Three-phase RT Rated output short circuit currents	104
6.10	Equivalent test setup for the stationary RT load tests	105
6.11	The input and output Voltage (a,b) and Current (c,d) waveforms for the three-phase RT as measured	107
6.12	Full-load measured voltage (phase) and current waveforms for Phase A	108
6.13	Total RT losses as a function of function of load current at rated input voltage	108
6.14	Efficiency of the three-phase RT as a function of output power at 400V L-L input voltage	109
6.15	FFT of the per phase output voltage of the RT during stationary testing	109
6.16	Rotor tied DFIG setup with RT on the left	110
6.17	Equivalent parameter estimation test setup of RDFIG with RT	110
6.18	RDFIG with RT per phase full equivalent circuit	112
6.19	RDFIG with RT per phase simplified equivalent circuit	113
6.20	Output voltage of the rotor tied to RT-RDFIG	114
6.21	Output current of the RT coupled RDFIG	115
6.22	FFT of the output voltage (L-L) during DFIG coupled tests	115
6.23	Simulated rotor shaft temperature at steady state without a fan for a given output current	116
6.24	Measured and simulated rotor shaft temperature without a fan over time	117
6.25	Thermal testing results of the RT after 2.5 hours at 6A	117
B.1	RDFIG equivalent circuit	132
D.1	Operating regions of a 50Hz, 4 pole DFIG	137
D.2	The operating regions of a 4 pole, 50 Hz RDFIG, with the field and mechanical rotation in opposite directions	137
D.3	The operating regions of a 4 pole, 50 Hz RDFIG, with the applied field and mechanical rotation in the same direction	138

List of Tables

1.1	Operating regions for a 50Hz 4 pole machine in both the stator- and rotor-tied configurations	7
3.1	Winding material comparison	50
4.1	6kVA three-phase RT design requirements	63
4.2	2kVA single phase RT design dimensions as shown in Figure 4.1	65
4.3	Inductances of the different proposed single phase RT	74
6.1	Inductance and resistance measurements per phase for the 0.6mm air gap RT at 25°C	97
6.2	No-load measurements with calculated core parameters	99
6.3	Three-phase RT short circuit parameters	103
6.4	Full-load test at (a) Rated input voltage, (b) Rated output voltage, (c) Maximum loading of 1.3PU. Voltage and currents are averaged between phases	106
6.5	RDFIG-RT No-load tests	111
6.6	RDFIG-RT Blocked rotor tests	111
6.7	DFIG with RT equivalent circuit parameters	112
6.8	DFIG with RT equivalent circuit parameters	113
6.9	RDFIG coupled testing	114

Nomenclature

Variables

a	Turns ratio	$[\]$
$A_{e_{ag}}$	Effective air gap area	$[m^2]$
A_{wp}	Area of primary conductor	$[m^2]$
A_{ws}	Area of secondary conductor	$[m^2]$
AG_f	Air gap correction factor	$[\]$
A_c	Cross sectional area of the RT	$[cm^2]$
A_p	Area product	$[cm^4]$
A_w	Cross sectional window area of the RT	$[cm^2]$
B_o	Operating flux density	$[T]$
D_{pi}	Inner diameter of primary core	$[m]$
D_{po}	Outer diameter of primary core	$[m]$
D_{si}	Inner diameter of secondary core	$[m]$
D_{so}	Outer diameter of secondary core	$[m]$
E_t	EMF per turn	$[V/turn]$
\mathcal{F}	Magnemotive force	$[A \cdot turns]$
f	Frequency	$[Hz]$
f_m	Rotor mechanical frequency	$[Hz]$
f_r	Rotor frequency	$[Hz]$
f_s	Stator frequency	$[Hz]$
H	Magnetic field intensity	$[A/m]$

NOMENCLATURE

xvi

i_p	Primary current	[A]
i_s	Secondary current	[A]
I_{mag}	Magnetizing current	[A]
K_f	Waveform coefficient	[]
K_u	Window utilization	[]
l	Length	[m]
L_{11}	Primary winding self inductance	[H]
L_{12}	Mutual inductance	[H]
L_{22}	Secondary winding self inductance	[H]
l_{ag}	Air gap length	[m]
L_{lkp}	Primary leakage inductance	[H]
L_{lks}	Secondary leakage inductance	[H]
L_{lk}	Leakage inductance	[H]
L_{mp}	Magnetizing inductance	[H]
L	Inductance	[H]
MLT_p	Primary mean length of turn	[m]
MLT_s	Secondary mean length of turn	[m]
N	Number of turns	[]
N_p	Primary number of turns	[]
N_s	Secondary number of turns	[]
n_m	Mechanical speed	[rpm]
n_s	Synchronous speed	[rpm]
ρ	Resistivity of winding material	[Ω/m]
P_m	Mechanical power	[W]
P_r	Rotor power	[W]
P_s	Stator power	[W]
P_t	Apparent power	[VA]

NOMENCLATURE

xvii

p	Number of poles	[]
\mathcal{R}	Reluctance	[A· turns/Wb]
R_p	Primary resistance	[Ω]
R_s	Primary resistance	[Ω]
s	Slip	[]
T_e	Turn per EMF	[turn/V]
$T_e m$	Induced electromagnetic torque	[Nm]
T_m	Mechanical torque	[Nm]
μ_o	Permeability of free space	[H/m]
μ_r	Relative permeability	[]
ϕ	Magnetic flux	[Wb]
ϕ_m	Mutual magnetic flux	[Wb]
ϕ_p	Primary winding flux	[Wb]
ϕ_s	Secondary winding flux	[Wb]
ϕ_{lkp}	Primary leakage flux	[Wb]
ϕ_{lks}	Secondary leakage flux	[Wb]
ϕ_{lk}	Leakage flux	[Wb]
ω_m	Mechanical speed	[rad/s]
ω_s	Synchronous speed	[rad/s]

Abbreviations

BDFIG Brushless Doubly Fed Induction Generator

BDFRG Brushless Doubly Fed Reluctance Generator

DD Direct Drive

DFIG Doubly Fed Induction Generator

FEA Finite Element Analysis

FFT Fast Fourier Transform

LVRT Low Voltage Ride-Through

NOMENCLATURE

xviii

MLT Mean Length of Turn

MMF Magnemotive Force

PM Permanent Magnet

PMSG Permanent Magnet Synchronous Generator

RDFIG Rotor-tied Doubly Fed Induction Generator

RT Rotary Transformer

SG Synchronous Generator

THD Total Harmonic Distortion

Chapter 1

Introduction

With the increase of global power demands, an increased focus has been on alternative solutions to alleviate the problem. One of the most popular alternatives is the use of renewable energy sources [1]. In recent years wind energy generation has become very popular in countries that do not have the geographic locations for other renewable sources such as solar power or hydroelectric generation. At the end of 2020 the Global Wind Energy Council (GWEC) reported an installed capacity of 743GW making it the second largest renewable energy source after hydroelectric [2]. The total world-wide generation capacity has increased by 14% from 2019 [2].

China has the largest total installed capacity of 206 GW and a growth of 10.3% from 2017-2018. Denmark is still a global leader with 47% of their total capacity being generated from wind energy [3, 4]. South Africa has seen an increase in wind generation with the current installed capacity of 2078MW in

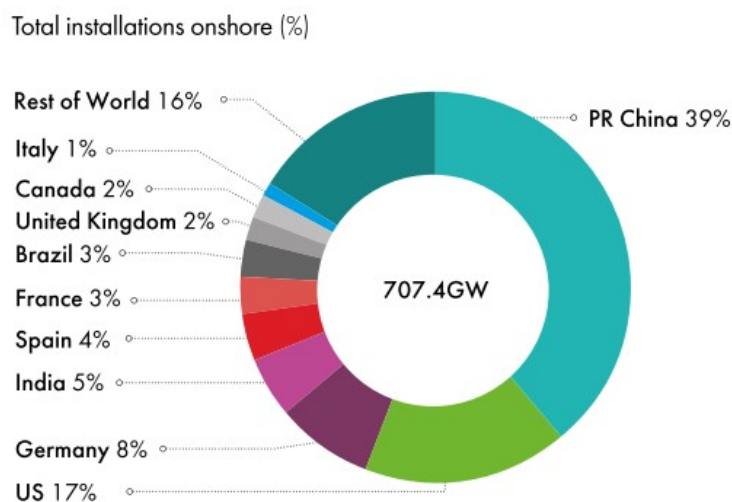


Figure 1.1: Wind installations by country. [2]

2019 [5], which is set to increase to 11442 MW in 2030 through commitments made by their integrated resource plan [6]. The distribution of wind installations can be seen in Figure 1.1.

The growth in this sector is negatively impacted by the high cost of developing new technologies and infrastructure. This is more pronounced in less developed countries. The electrical generators that are used in these wind turbines need to be as efficient and reliable as possible. Currently research into improving these two key factors is being done [7].

The generators that are used in these turbines fall into two main categories, fixed or variable speed. Constant speed generators such as permanent magnet synchronous generators (PMSG) are not as common, as the variable speed setups provide more flexibility and a wider speed range without the use of fully rated converters. The three most common types of variable speed generator topologies are

- Brushless permanent magnet (PM) or IG with a full converter
- Direct drive (DD) systems such as a synchronous generator (SG)
- Doubly fed induction generator (DFIG)

The variable speed brushless generator is designed with the use of a gearbox and a fully rated converter. This allows the use of either a squirrel cage induction machine or a permanent magnet machine. Both types of machines avoid using slip rings and have decreased maintenance costs. The downside is that the fully rated converter increases the total losses and decreases the efficiency of the solution [7].

In recent years the use of DD system has become much more popular. It allows for the removal of the gearbox, which is a common point of failure [8]. It incorporates a SG that is directly connected to the output of the turbine. These SGs can either be permanent magnet, or a wound rotor that requires external excitation [9]. The SG still requires a fully rated converter in order to be connected to the grid. Since the SG is directly connected to the turbine, it needs to withstand the full torque output of that turbine. This leads to larger machines that are much more expensive to manufacture and maintain [7, 8, 10, 11].

To overcome the limitations imposed by these types of drives, various hybrid drive trains have been investigated. The most popular among these is the DFIG. It consists of a partially rated converter, a gearbox and a wound rotor induction machine as shown in Figure 1.2d. The DFIG has a speed range of $\pm 30\%$ of the synchronous speed. The DFIG has windings on both the stator

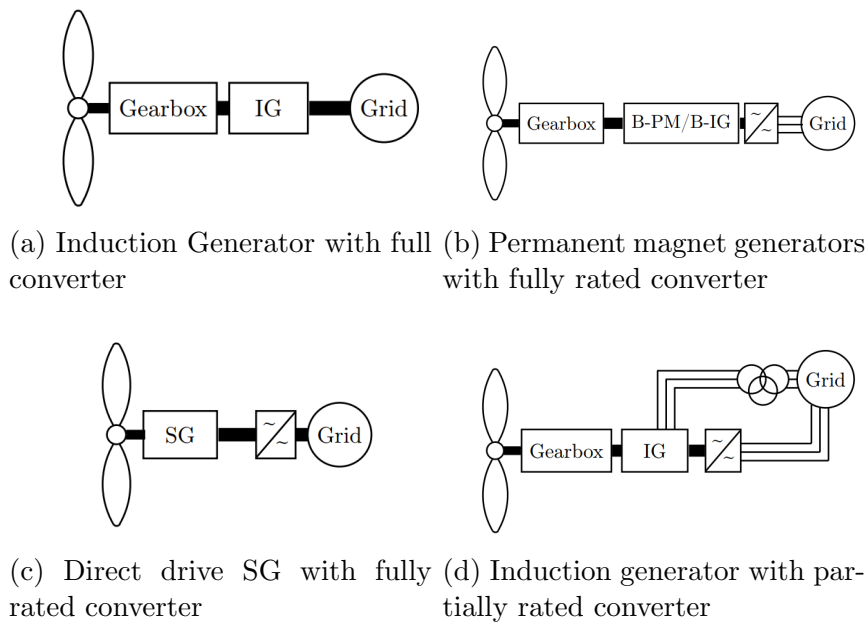


Figure 1.2: Current wind turbine generator topologies

and the rotor. Current and frequency control on the rotor is done through the power converter, and this requires access to the rotor windings. The advantage of this is that the power converter only needs to be rated for a fraction of the mechanical power, typically only a quarter. The advantages that this brings is lower initial cost and a smaller converter, making this the most employed system in wind electricity generation [7, 9].

The current DFIG system is however not without flaws and has two main disadvantages. First the rotor needs to be accessed and this is done with slip ring and brush assemblies. In DFIG systems, the slip ring and brush assemblies was the most common type of failure in the system due to worn brushes [8]. Second, the DFIG has poor grid-fault ride-through capabilities. Significant research has already been done to improve the DFIG's fault ride-through capabilities [12–15]. One of the proposed solutions is the use of a brushless doubly fed induction generator (BDFIG) as they typically have better fault ride-through capacities compared to standard DFIGs [16]. A BDFIG consists of two sets of 3-phase windings on the stator, each with a unique number of poles. A special rotor cage is required to couple both windings. The BDFIG addresses both the poor fault ride-through and reliability of the DFIG but is considerably more complicated to manufacture and maintain, increasing the initial and operating cost of the system.

Recently an alternative was proposed for the BDFIG, which is to use a

normal DFIG with a rotary transformer (RT) to access the rotor windings. The RT replaces the slip rings and works by inductively connecting the two circuits to each other. To facilitate rotation, this RT needs a small air gap between the stationary and rotating side. Since this is a contactless solution, the reliability issues of slip rings can be overcome [17–23].

1.1. Literature review

The DFIG is a well-researched and widely used type of generator in wind energy conversion systems. Recently there have been numerous studies into the concept of replacing the DFIG with a BDFIG [17–22]. The BDFIG is an attractive alternative to the DFIG since it removes the need for slip rings, while still maintaining the advantages associated with the DFIG. The following section discusses the studies done on BDFIG concepts.

1.1.1. Brushless doubly fed induction generator

Due to the advantages discussed in the previous section, the DFIG is a very appealing option due to its low initial cost and only partially rated converter. There are various concepts on eliminating the need for slip ring and brush assemblies, with one of the proposed options being the BDFIG, as it aims to keep the advantages from the DFIG while eliminating the use of brushes.

The BDFIG consists of two windings on the stator, the control winding that is handled by the converter and the power winding. These two windings have different number of poles in order to avoid coupling between the two. Each of these windings produces a separate magnetic field that couples with a specially designed rotor. The generator operates in synchronous mode and the frequencies of the power and control windings determine the rotor speed. There is a higher number of poles in the BDFIG, so the machine is usually limited to medium speed operation. This allows the use of a single or double stage gearbox to achieve the required speed from the turbine. This is the first advantage over the DFIG which it requires a multi-stage gearbox that is more complex and expensive [7].

The second advantage that the BDFIG offers is improved low voltage ride-through (LVRT). In a DFIG the stator is directly connected to the grid, and any drop in grid voltage could lead to decreased or loss of magnetization. This results in current surges on the rotor which leads to additional losses. A standard DFIG is usually fitted with a crowbar circuit or additional current control to overcome this issue. The BDFIG has a much larger series inductance which limits the transient current of the subsequent voltage drop [12–15].

Despite these advantages that a BDFIG offers, the machine is much more complex. Having two separate excitation windings on the stator, it makes the machine more difficult to design and simulate. The machine is also larger than an equivalent DFIG, approximately 30% higher according to a study done in Lipo et al for the same power density [24]. Several medium rating machines have been developed [25–27] and designs for a 6MW machine is presented by [28]. Such large BDFIG machines are still in the design phase and need to be demonstrated practically.

Other brushless technologies should be explored, specifically setups that do not change the fundamentals of the machines and allow them to remain relatively simple in their design. The performance of these setups can be compared to the BDFIG as to develop an improved drive train.

Synchronous generators with fully rated converters are one of the ways that a brushless system can be obtained. In the following section, the two methods that have been proposed are discussed.

1.1.2. Synchronous generators with fully rated converter

Many different forms of synchronous generators (SG) exist, but they all lack the ability to have speed control. A fully rated converter is needed to connect the generator to the grid. The advantage of this type of generator is that it can be used as a direct drive and by removing the need for a gearbox, the reliability is improved. The SG becomes much larger since it must handle the full torque output from the turbine [7].

Two alternative topologies have been proposed to create a fully brushless SG. The first is the permanent magnet (PM) SG. In this configuration the rotor of the SG does not need excitation, completely removing the need for brushes and slip rings. A disadvantage of this system is that PMs are very expensive, especially at the size required for large scale wind farms. The other downside is that with a PM the flux within the SG cannot be reduced if the machine is overloaded, which can cause mechanical breakages or over-voltage if the turbine cannot be braked in any other way [7,9].

The second method is replacing the slip rings of the SG with a single-phase rotary transformer. Since the excitation current required is DC, several solutions have been explored by [29,30] to increase the driving frequency and reduce the size of the transformer required. The main disadvantages of this system are that it has an increased amount of electronics that can fail, and

the efficiency of the system is lower than with a conventional PM SG.

Another type of machine that can be investigated is the DFIG with a three-phase rotary transformer. It keeps the simplicity of the DFIG but removes the need for brushes. The following section introduces the DFIG with a RT concept.

1.1.3. The brushless doubly fed reluctance generator

The brushless doubly fed reluctance generator (BDFRG) is a machine very similar to the BDFIG. The main difference between the two is that the BDFIG has a winding on the rotor, where the BDFRG has all of its windings on the stator side. The advantage of this is that the secondary winding only requires a partially rated converter and is situated on the stator side. Compared to traditional designs, the BDFRG has a lower power factor but can be designed to have a high torque density, with the added advantage of having a rotor that is much easier and cheaper to manufacture [31–34]. Dorrell et al investigates the possibility of using a 2MW BDFRG in a wind turbine to replace the DFIG [35]. They concluded that the machine cannot be used without active power factor control.

1.1.4. The rotor-tied DFIG

Conventional DFIGs have their stator connected directly to the grid and their rotor connected to a partially rated converter. A novel doubly fed induction machine concept was proposed by [36] in which the stator is connected to the partially rated converter and the rotor directly connected to the grid. This topology has shown to have lower core losses than that of the conventional DFIG. This has to do with the higher frequency windings being on the rotor core which is typically smaller than stator cores. This also allowed for a reduction in overall machine weight. The machine was tested as a motor, and it achieved an efficiency of 90.5%. The model was not demonstrated as a generator and efficiency when operated as a DFIG was not analyzed.

Olubamiwa [37], designed and built a 5.5kW rotor-tied DFIG (RDFIG). It features a standard 132m frame with a pre-designed rotor. The generator was tested using slip rings that are placed outside of the machine due to a lack of space. The rotor is connected to a transformer before it connects to the grid. The generator was able to deliver 4.9kW of power to a load at an efficiency of 87% when the DFIG was run at or below synchronous speed, but only 81% at super-synchronous speed.

1.1.5. DFIG with rotary transformer

The idea of rotary transformers has been around since 1961 [38] and have been implemented in various applications [39–41]. In recent years, commenced into using a RT for replacing the slip rings in a DFIG [17–22]. The RT is placed on the rotor shaft and has direct access to the rotor windings. The proposed RT coupled to the induction machine shaft is shown in Figure 1.3b. For a normal DFIG the frequency of this transformer is equal to the slip frequency of the machine. This frequency is quite low and since transformer size is inversely proportional to the frequency, a large RT with laminations must be used. This results in a much lower efficiency of the transformer and increases the complexity of the design and manufacturing.

The RDFIG reduces the need for a very low frequency RT due to the rotor being at grid frequency (50-60 Hz). Since the size of the RT is inversely proportional to the frequency, the proposed solution of the RT coupled, RDFIG as a type of BDFIG is more feasible. The RT can be constructed using standard lamination thicknesses that are readily available.

The RDFIG has a different operation characteristics with regards to the conventional DFIG. This changes the expected operation regions of the RT, both in terms of frequency and power. The operating region for the RDFIG can be such that the power flow on the rotor can either be in or out of the machine, at a wide speed range. This requires the RT to maintain the same parameters irrespective of speed and allow for magnetization and power from both sides. At synchronous speed, the RT is expected to handle the most power, therefore this is usually set as the design point. The operation regions for the RDFIG can be seen in Table 1.1 and is derived in Appendix D.

Table 1.1: Operating regions for a 50Hz 4 pole machine in both the stator- and rotor-tied configurations

Stator tied		Rotor tied			
		Opposite direction		Same direction	
Slip	Power flow	Slip	Power flow	Slip	Power flow
$s > 0$	Stator delivers Rotor draws	$s < 0$	Stator delivers Rotor delivers	$2.5 > s > 2$	Stator delivers Rotor delivers
$s < 0$	Stator delivers Rotor delivers	$S > 0$	Stator draws Rotor delivers	$2 > s > 1.75$	Stator draws Rotor delivers

1.1.6. Rotary transformer implementations

Techniques for dividing the rotor and stator of the RT into segments has been discussed in [18, 42]. This would greatly aid in the assembly and maintenance of the RT. Guidelines for the sizing of the segments are also proposed, but the design in [18] was not practically implemented, so it is unclear which material would be the most suited for such a design.

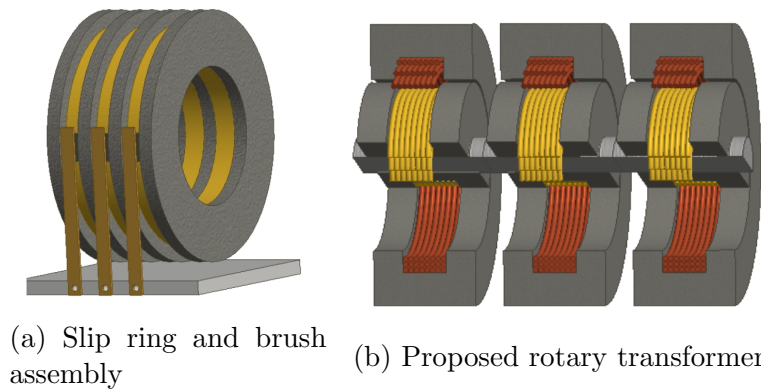


Figure 1.3: Slip rings with brushes vs brushless topology

To design the RT, an important consideration is the lamination layout. Several different lamination directions are discussed in literature. The use of segmented lamination sections is presented by [22] and uses a combination of axial and radial laminations to limit eddy currents in the core. The limbs around the windings are radially laminated while the connecting part is axially laminated. This improves the fill factor of the laminations as there is no need for air gaps between laminations. Since the magnetic flux flows approximately in the direction of the lamination in each section, eddy currents will be induced in those sections. To mitigate these, the radial laminations contain gaps that act as high resistance eddy current barriers to reduce the magnetic flow.

An alternative proposed idea of lamination directions is presented by [18] but achieves it by manufacturing each radial and axial piece on its own. This allows the flux to always flow in the direction of the lamination which is joined at the end. This method requires complex machining and assembly and results in closer tolerances [18].

To reduce the overall size of the transformer, Lipo et al proposed a two-phase RT [24]. This requires a three-phase to two phase conversion on both ends using the RT as a Scott T transformer. The proposed solution allows for a 35% reduction in total volume. The disadvantage is that this can result in an

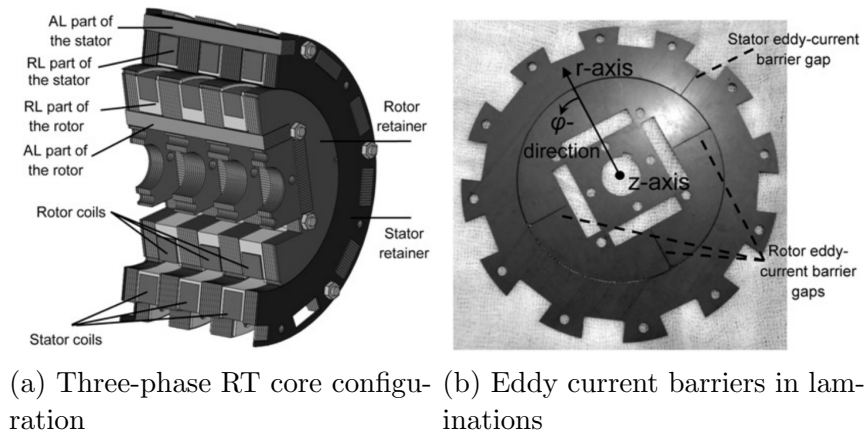


Figure 1.4: Combination of axially and radially laminated core [22]

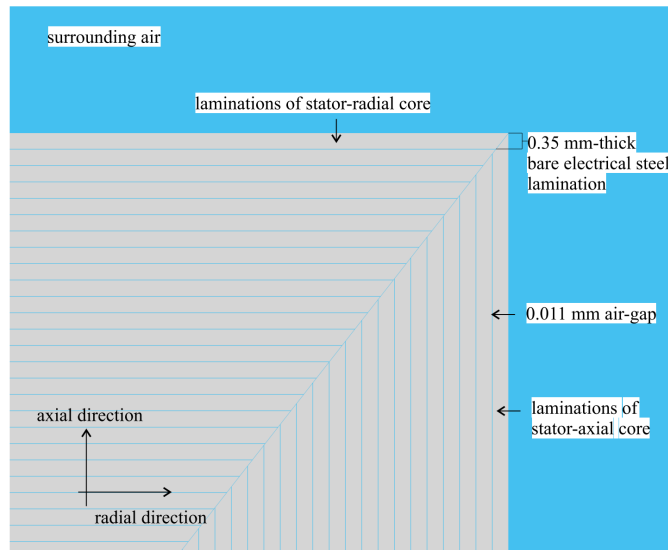
unbalanced system that require a more complex control to stabilize the phases.

A study conducted in [17, 42] illustrates the large size that a 50Hz transformer must be for a given power rating. In DFIG drive trains, the weight of the RT is an important factor to consider. The weight and size of the RT must be addressed when discussing the suitability of the application. The prototype developed in this study was only able to deliver 1kW of power at 90% efficiency (single phase). The conclusion was drawn that for a large through-bore RT there is an inefficient use of core material.

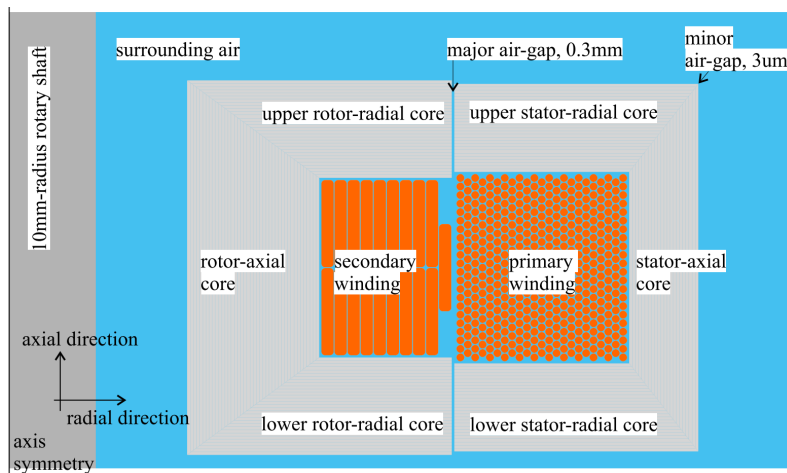
The transformer that was constructed by WEG for both the 90kW and 350kW DFIGs had sizes that was comparable to the generator itself. The implementation tested on the 90kW DFIG resulted in the system having an efficiency of 94.8%. This is comparable to the efficiency that can be obtained by the DFIG on its own (95.7%). The power factor of such a system is lower than in comparable DFIG systems due to the inductive nature of the DFIG [20, 43].

The alternative to laminated RTs is using a high frequency core with a converter [44]. This requires power electronics on both sides of the RT which means that there will be electronics on the rotor. The proposed system is shown in Figure 1.6 For single phase setups this is much more beneficial. The design of a RT for synchronous generators are discussed in [29]. Due to using higher frequencies and electronic components on both the stator and rotor side, a much smaller transformer was designed. This type of design allows for a much more power-dense RT, which costs less and is easier to manufacture than a laminated core. By using pot cores and axial air gap topologies very high efficiencies was obtained, 98.9% and 99.2% respectively. The main disadvantages of using the concept proposed are the use of driving circuitry

and converters which lowered the efficiency of the entire system to just 61% and 67% respectively. There is also the issue of reliability when using electric components on both the stator and especially the rotating side.



(a) Lamination layers



(b) Cross-section of RT concept

Figure 1.5: Combination of axially and radially laminated core [18]

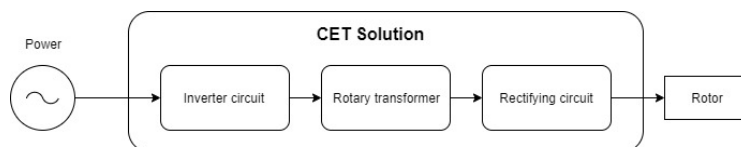


Figure 1.6: Proposed CET solution for brushless SG [44]

1.2. Research objectives

Due to the popularity and implementation of the DFIG in medium to large wind turbines, studies into a brushless solution are important. The low initial cost and only partly rated converter make this type of machine very attractive. The reliability of this type of generator is still a major issue and to mitigate it, the BDFIG was proposed. The double stator BDFIG has no brush and slip ring assembly, so it is more reliable over a long period.

An alternative to the double stator BDFIG is the use of a DFIG coupled through a RT. [17–22]. This allow for the brushless operation of the DFIG while keeping all of its advantages such as the variable speed. The RT-coupled RDFIG further improves on this concept as it allows for the use of smaller RTs. There are still several challenges that the design procedure of the RT has, namely size, complexity, and magnetic coupling stability.

The aim of this research is to develop a design procedure in which the following issues are addressed:

- Low efficiency of proposed RTs
- The magnetic coupling stability
- The cooling on the rotor of a RT
- The large size and low power density of RTs

The design aims to increase efficiency while still maintaining an acceptable overall size of the RT. The designed model will be manufactured and tested on a RDFIG. This allows for a higher frequency on the RT, which should reduce its size significantly.

The proposed research is aimed at achieving the following:

- Develop an analytical model of a single RT to compare against an optimized 2D and 3D FEA model
- Compare performance for different three-phase core layouts
- Develop a thermal model for the proposed RT
- Manufacture and test the RT with a minimum efficiency of 90%
- Compare the operation of the RDFIG with and without the RT

By achieving these expectations, the effectiveness of such a proposed solution can be evaluated and a comparison can be made against other brushless topologies. The RT will enable the RDFIG to operate without the need for a slip ring and brush assembly, reducing the time and cost of maintenance.

Chapter 2

Rotary transformer design considerations

The rotary transformer is uniquely different from a normal transformer in many ways. For the transformer to rotate, there needs to be an air gap. The air gap combined with the geometry of the RT leads to a design process different than that of a standard transformer and shares many similarities to DFIG design. The efficiency and size of the RT are of particular interest in the proposed RDFIG application. In this chapter, the most important design considerations of the RT are discussed. Different aspects are explained about the design of the RT.

2.1. RT topology configuration

One of the most important constraints in designing a RT is the ability to rotate freely and maintain electrical coupling during operation. The rotation should not affect the transformer's performance and the only way to ensure that is by having a constant flux path over the full rotation. There are two primary single core configurations proposed by Landsman to facilitate this constant flux path [39]. The configurations are axial where the air gap is along the length of the shaft and radial where the air gap is in the radial direction. The axial air gap configuration can be seen in Figure 2.1a and consists of a larger outer core and a smaller inner core. The radial air gap configuration, which can be seen in Figure 2.1c, consists of two halves that are identical and facing each other.

In an integrated machine, the RT must be mounted onto the same shaft as the DFIG, so the inner diameter is restricted to the shaft dimensions. This increases the diameter of the transformer which affects the total size of the core and the mean length of turn (MLT). The increase in size and MLT has resulted in the inefficient use of both the core and winding material [45]. The

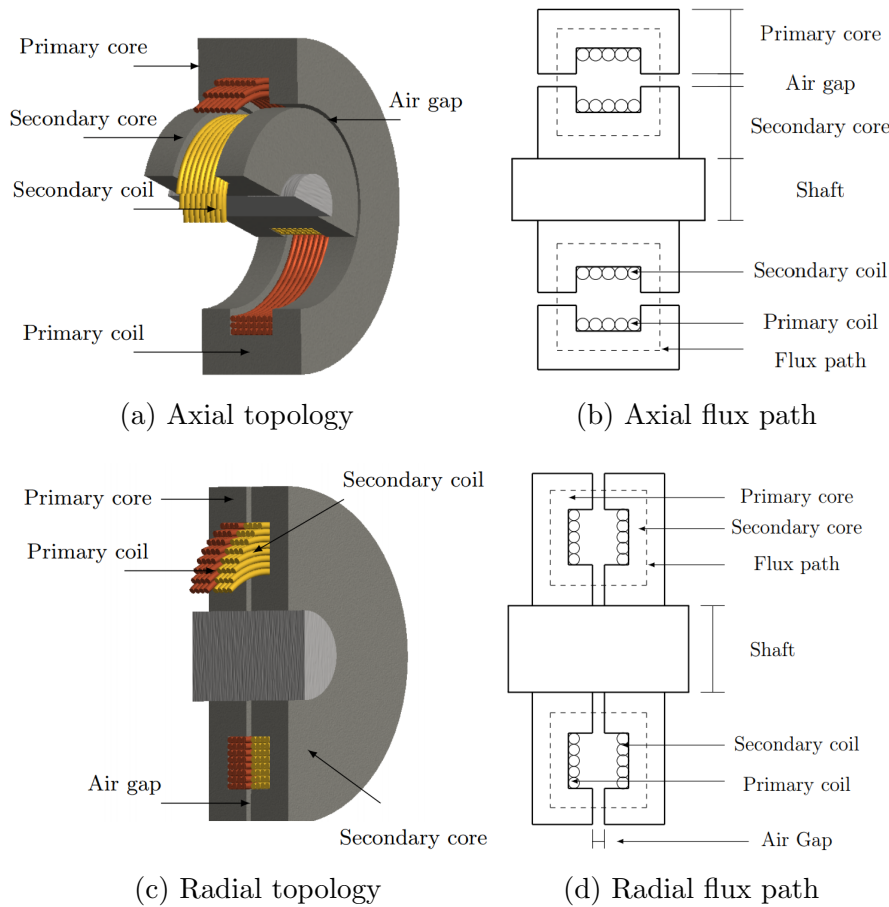


Figure 2.1: The two core topologies: (a) Radial and (c) Axial air gap. The flux path through the core is shown in (b) and (d).

shaft diameter can be decreased but depending on the configuration of the machine, this could reduce the structural integrity of the machine, especially if the weight of the RT is large in comparison to the machine. A larger RT will have increased inductance and inertia that could be beneficial for grid-tied applications due to the filtering and longer fault ride-through capabilities during short circuits.

The topology of the RT is a choice based on the trade-offs that each setup offers and the requirements of the application. Both topologies shown in Chapter 2 have windings that are permanently aligned during operation. This result in no additional torque being applied to the rotor shaft. An axial force is applied to the shaft in the radial configuration due to the magnetic force that exist between the two windings [20].

For high-frequency RTs the best magnetic coupling for a ferrite-based core

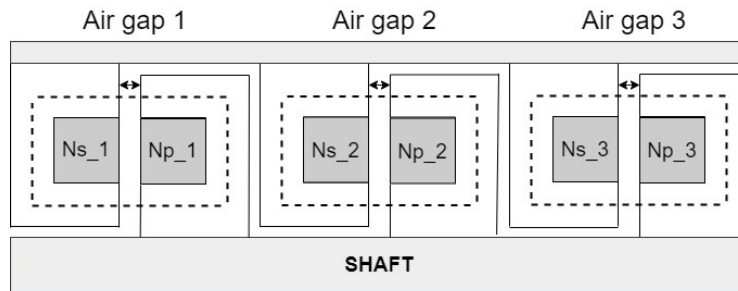


Figure 2.2: Three-phase configuration with radial air gap stacked along on the shaft

is offered by the radial setup, and this lead to designs that utilize pot cores as RT [46–48]. This configuration takes advantage of the low flux leakage of pot cores and the simplicity of construction due to the availability of the cores. For low frequency laminated RTs, this is not the case due to the increased core counts in a multi-phase system.

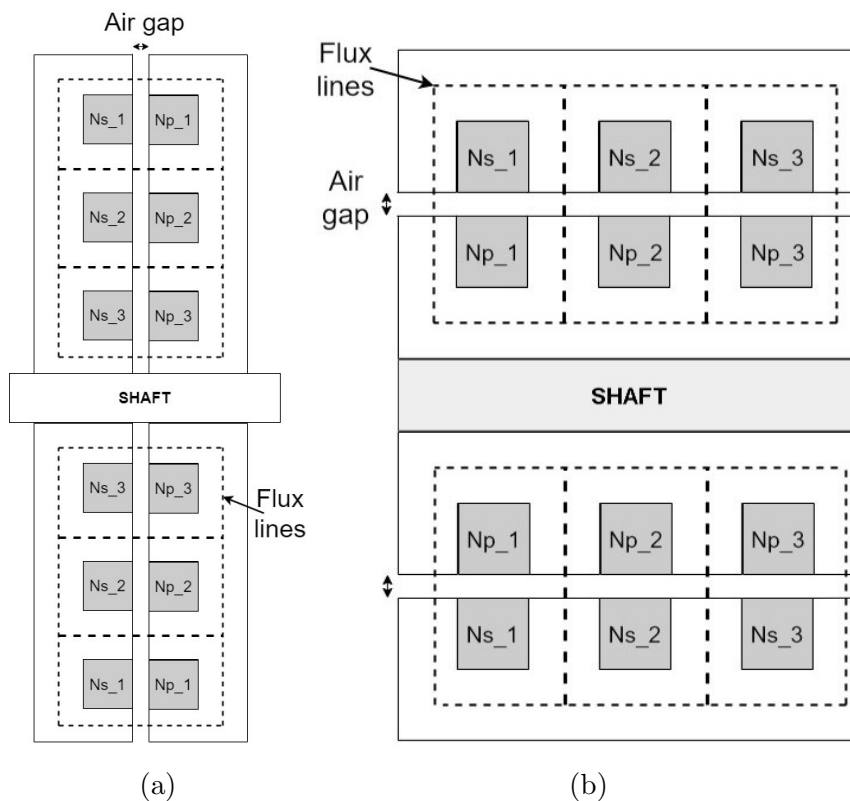


Figure 2.3: Three-phase RT with a single shared core in the (a) Radial air gap, and (b) Axial air gap configuration

In three-phase systems there are two primary options when selecting the core layout. Three single core configurations were proven to work by [49], and offer advantages such as easier maintenance and better isolation from each other. They can be separated as either three axial air gap cores along the length of the shaft. This is the easiest to manufacture and is in a similar configuration to Figure 2.3b but with space between the cores, or three radial air gap cores along the length of the shaft as shown in Figure 2.2. For very large machines this spacing could be beneficial due to the cooling requirements.

The second type of RT is the single core, three winding setup, similar to conventional power transformers. Its advantage is that it saves space and reduces the overall cost of manufacturing. The single core can be arranged in an axial or radial air gap orientation as shown in Figure 2.3. The main disadvantage of the radial air gap configuration is that each phase is at a different radial distance from the shaft, and it becomes more difficult to balance the phases. The axial air gap configuration does not suffer from the same unbalanced phase layout but could present problems in terms of cooling. This type of core is well suited to stationary transformers, but in the RT the design has to be cylindrical in shape to ensure constant magnetic coupling while rotating.

2.2. Power rating

In any transformer the total power rating is very important in determining the size of the transformer. The power rating is a function of the operating frequency, apparent power, and geometry. The transformers area product A_p , is a representation of its power handling and is a function of its core cross-sectional area A_c and the window area A_w . The required area in cm^4 is given by

$$A_p = A_c \times A_w \quad (2.1)$$

$$A_p = \frac{P_t \times 10^4}{K_u K_f B_o J f} \quad (2.2)$$

where P_t is the apparent power of the transformer, K_u is the window utilization factor, K_f is the waveform coefficient (4.44 for a sine wave), B_o is the flux density in the core, J is the current density in the wire and f is the frequency.

Both conventional and rotary transformers have two loading variables: magnetic and electrical loading. The magnetic loading of the transformer is in the form of the operating flux density (B_o) in the core material. The flux density is dependent on the core material and the total amount of induced flux from the windings. At saturation, an increase in field current will result in a small

increase in flux, which leads to higher conduction and core losses. The electrical loading is the current density (J) in the winding material, and it is directly related to the conduction losses.

The total power rating for the RT is determined by the system in which it is installed. For a RDFIG, the transformer power rating should be equal to rotor power of the generator, and match the phase voltage and line current to be directly coupled to the grid.

2.3. Winding configuration

For each RT topology, there is more than one winding configuration. When the system is designed as a single phase, there are two winding topologies for both axial and radial air gap configurations. The first is the adjacent winding topology, where the primary and secondary winding is in their respective half of the core. The second is the coaxial winding topology where both the wind-

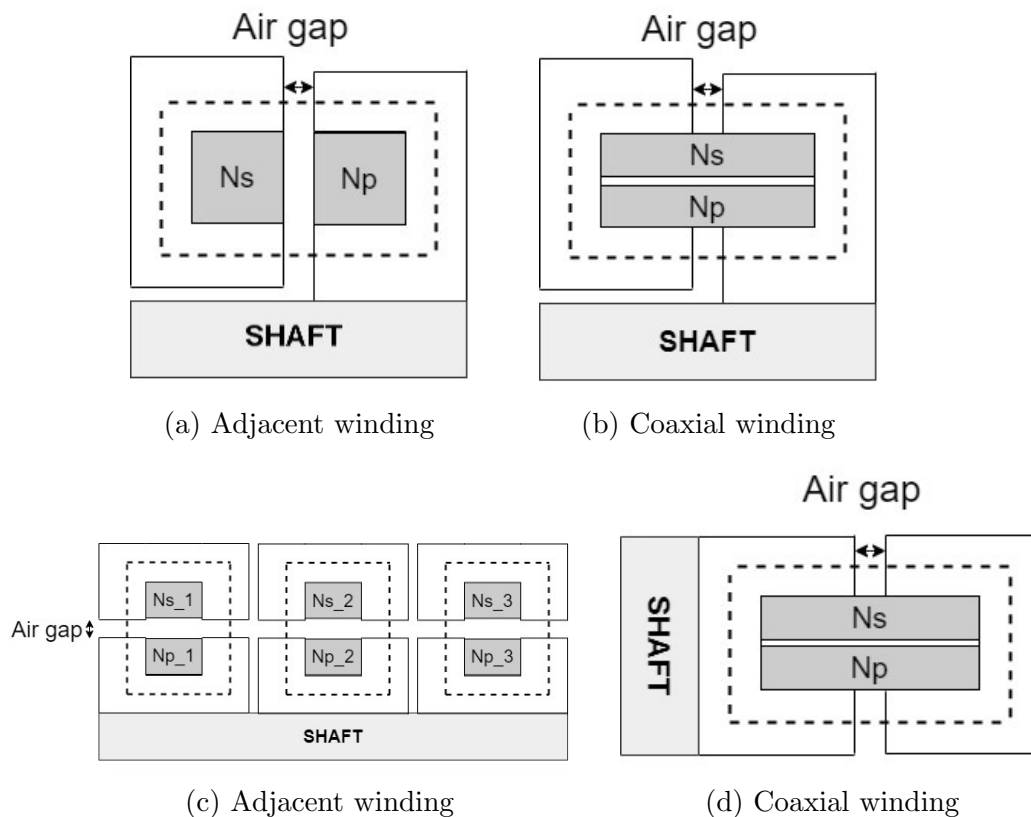


Figure 2.4: The winding layout for the radial air gap topology: (a) Adjacent and (b) Coaxial, and the axial air gap topology: (c) Adjacent and (d) Coaxial

ings occupy space in each half of the core. This reduces the distance between the windings and subsequently increase the coupling at the cost of complexity of construction and maintenance. The configurations are shown for the axial and radial air gap topology in Figure 2.4.

For the topology with all three phases sharing the same core, there are two methods of winding; adjacent and coaxial. The adjacent winding configuration has the advantage of being easier to construct. While the coaxial windings offer better magnetic coupling, they could be too costly to manufacture due to the low tolerances required. The type of winding chosen will depend on a combination of the topology of the core and the achievable winding fill factor.

2.4. Operating frequency and size

The operating frequency for the RT will depend on the rotor frequency of the DFIG. For standard DFIGs, this is proportional to the slip frequency, which is around 2-5Hz. In standard DFIGs the rotor frequency is so low that the size of the RT is comparable to the size of the DFIG [43]. Since the size of the RT is inversely proportional to the frequency by

$$A_p = \frac{P_t \times 10^4}{K_u K_f B_o J f}, \quad (2.3)$$

higher frequencies will lead to a lower size. At lower frequencies the efficiency of the transformer decreases from three factors namely: higher eddy currents, increased copper losses due to a longer mean length of turn, and increased hysteresis losses. The increased size can also increase the leakage inductance which reduces the power factor of transformers.

The proposed alternative is to use a rotor tied DFIG. Its main advantage for the use with a RT is that the operating frequency of the RT will be at the grid frequency of 50/60Hz. This decreases the size of the RT significantly even though the RT will have to handle more power [42]. Most wind turbines have limited space in the nacelle, thus space is essential in choosing a generator solution. A smaller size also leads to a reduction in manufacturing cost. Replacing the conventional transformer in the nacelle shown in Figure 2.5 with a RT could be a viable option.

At such low frequencies the core will have to be laminated to reduce the eddy currents. The lamination thickness will depend on the frequency of the transformers. The laminations need to be placed in such a way as to guide the flux as much as possible, while still limiting eddy currents. This poses a problem as the flat laminations will have to be around the wire direction, which is around the shaft. When these type of axial laminations are used the

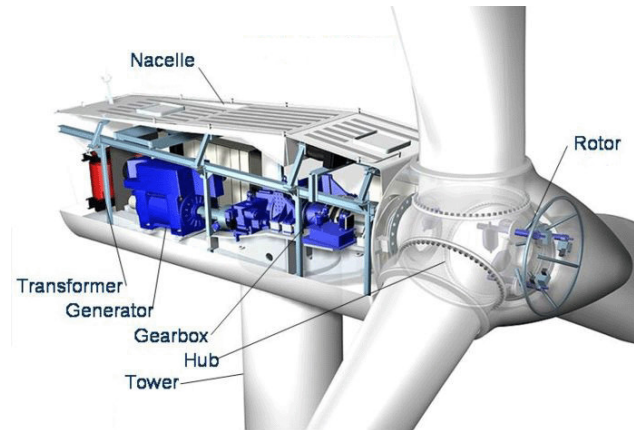


Figure 2.5: Space in the nacelle of a wind turbine [50]

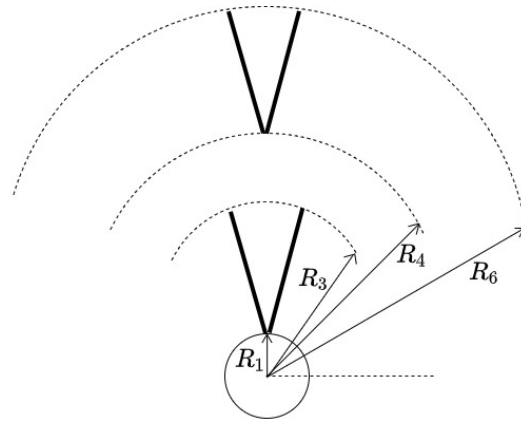


Figure 2.6: Axial lamination spacing due to different diameters

fill factor of the laminations decrease because the laminations have a constant thickness, but the inner and outer diameters differ. This spacing is shown in Figure 2.6. spaces between the laminations on the outer diameter decreases the total core material which makes the RT more susceptible to saturation at a given voltage rating. This spacing needs to be accounted for when designing the RT. The laminations can also be a combination of rolled and stacked laminations which will increase the fill factor and therefore reduce size, at the expense of complex and expensive manufacturing.

2.5. Losses in a RT

The losses of an RT consists of three main components: conduction loss, core loss and mechanical loss. Conduction losses in the windings are proportional to the square of the current that flows in the winding. Reducing the current density by choosing the appropriate cross-sectional conductor will minimize the conduction losses. The mechanical losses are a combination of friction losses on the bearings, wind resistance loss, and torque exerted on the shaft from the mechanical flux. Choosing a topology that does not exert a torque on the shaft is of vital importance in the design of an RT, as to keep the efficiency of the DFIG high.

The time-varying electric fields result in core losses within the ferromagnetic material as hysteresis and eddy current losses. The first type of loss is induced eddy currents that flow perpendicular to the direction of the flux. The energy of these currents is dissipated as heat. Since the power loss is proportional to the area of the loop, using thin laminations that are insulated from each other decreases this type of loss. The effect of the eddy currents is illustrated in Figure 2.7.

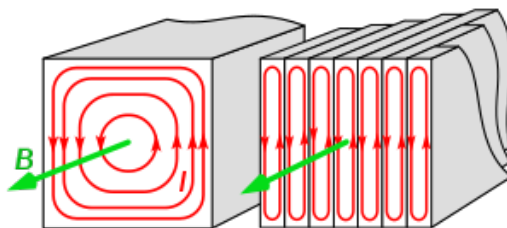


Figure 2.7: Eddy currents in a solid core vs laminated core

The second type of core loss is hysteresis loss. Hysteresis occurs when an external magnetic field is applied to a ferrite material and the magnetic domains align with the magnetic flux. To obtain the hysteresis loop, the flux in the core can be plotted against the magnemotive force (mmf). In most materials the hysteresis is not a linear relationship as the flux in the core is not only a function of applied current but also of residual flux in the core. The area of the hysteresis loop relates directly to the amount of energy dissipated in a cycle and is shown in Figure 2.8.

When the flux in a ferromagnetic material does not increase with the increase of mmf, the core is saturated. Increasing the input current to the RT will not increase the output current, thus operation in or close to the saturation region lowers the efficiency of the transformer.

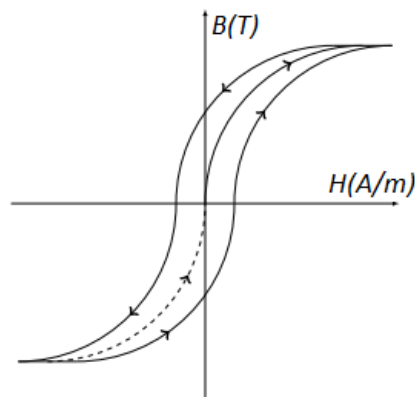


Figure 2.8: The hysteresis loop

2.6. Efficiency

In a conventional DFIG the slip ring and brushes offer superior efficiencies. In order for an RT to be a viable solution, the overall system efficiency should be comparable to that of a system that employs a slip ring and brush assembly.

Standard transformers can offer efficiencies in excess of 98%. In conventional transformers the efficiency increases as the power rating increases, a characteristic shared with RTs. In [51] a comparison is done between an RT and a conventional transformer when used with a DC-DC conversion system. The overall system efficiency difference is less than 2% when both of the transformers are loaded equally. The efficiency curve for these transformers is given in Figure 2.9.

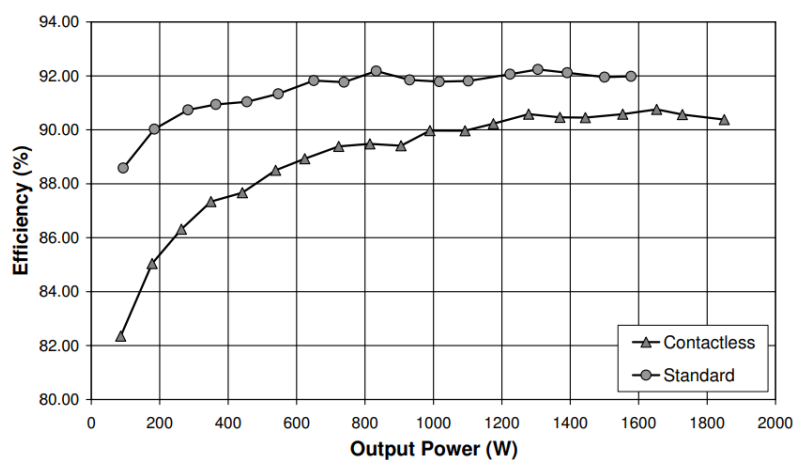


Figure 2.9: Efficiencies of the standard transformer and RT as a function of output power [51]

WEG manufactured an RT for use in a 90kW DFIG [43,49]. The DFIG had its rotor connected to external resistors to limit the current on the rotor. This allowed Ruviaro et al to achieve an efficiency 94.7% when running the system as a generator, compared to an obtained efficiency of 95.5% when the DFIG is used with slip rings. The disadvantage is that the added impedance from the RT caused a lower power factor.

To maximize the total system efficiency, the losses in the RT must be kept to a minimum as discussed in the previous section.

2.8. The air gap

To facilitate rotation of the transformer, an air gap must be present between the two halves. The first effect due to the air gap having a much larger reluctance than the core, the magnetizing inductance will be lower. The second effect that the air gap will have is an increase in leakage flux. The reluctance of the core is directly related to the relative permeability μ_r as well as the length (l) and area (A_e). The relationship is described by

$$\mathcal{R} = \frac{l}{\mu_r \mu_o A_e}, \quad (2.4)$$

with μ_o being the permeability of free space. The magnetizing inductance (L) is dependent on the reluctance of the entire core as well as the number of turns that

$$L = \frac{N^2}{\mathcal{R}}. \quad (2.5)$$

The electrical steel that transformers are usually constructed with have a relative permeability of around 4000 times that of air. The reluctance of the air gap will have a great effect on the inductance in the RT. With the same number of turns the magnetizing current will have to increase to achieve the same flux density as a non-gapped core.

The effect can be demonstrated using the BH curve of a transformer with an air gap. As the air gap increases, the slope of the curve decreases. The BH curve is the relationship between induced flux (B) and magnetic field intensity (H). The effect of the air gap can be seen in Figure 2.10. The energy loss was nearly the same (1.49W/Kg for no air gap and 1.45W/Kg for the 0.07mm AG) for both setups [52].

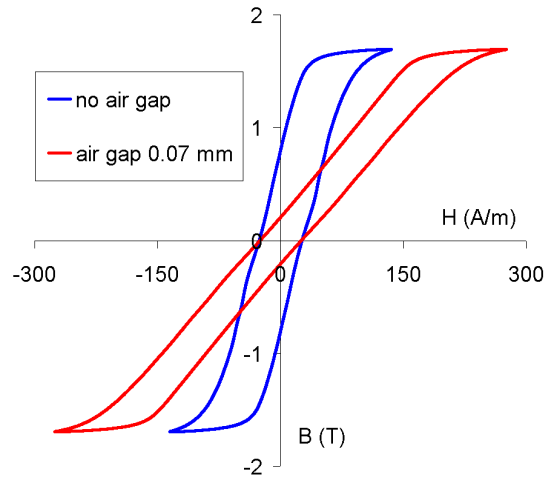


Figure 2.10: BH curve for a transformer with no air gap and one with a 0.07mm air gap [52]

With the separation of the two halves of the transformer, the distance between the coils increases. This separation results in a higher leakage inductance. Research done by [48] show the magnetizing and leakage inductance as a function of the air gap length for an adjacent pot core transformer. This can be seen in Figure 2.11. The leakage inductance is not affected significantly by the increase in air gap (both primary and secondary leakages), but the magnetizing inductance decreases with the increase in air gap.

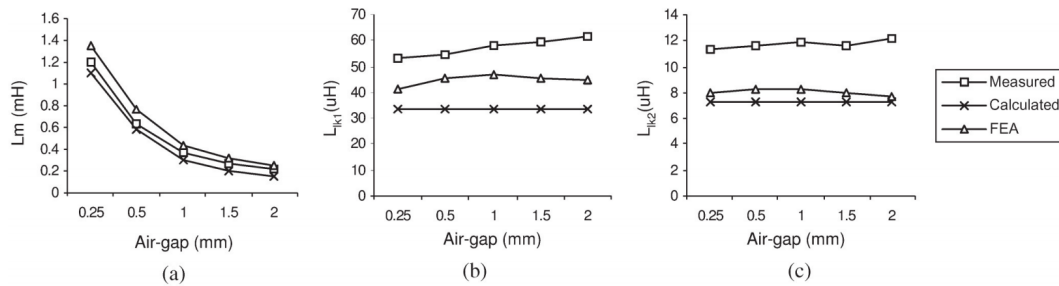


Figure 2.11: The effect that the air gap has on (a) Magnetizing inductance, (b) Primary leakage inductance and (c) Secondary leakage [48]

For the three-phase, radially laminated RT presented, the effect of the air gap is shown in Figure 2.12. The leakage inductance does not increase significantly when a change in the air gap is observed. This indicates that the RT will not be very sensitive to coupling changes when fully loaded.

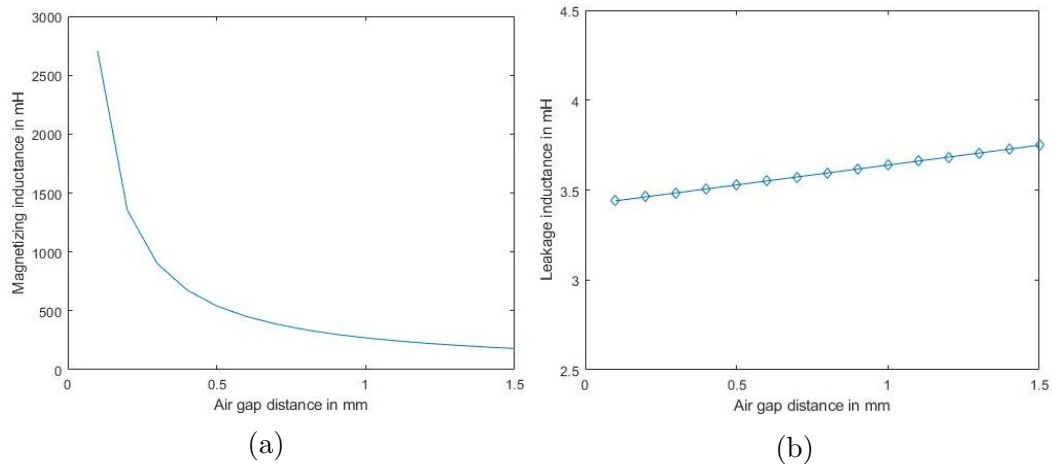


Figure 2.12: (a) Magnetizing inductance and (b) Leakage inductance of the RT as a function of air gap distance for the three-phase, radially laminated, 6kVA RT

2.9. Rotational effects

The rotation can have a large effect on the inductances of the RT, especially if the air gap distance is not maintained. When the air gap distance remains constant, there can still be changes in inductance such as when the end windings of the coils line up. The effect of the rotation was tested in [53] for an RT. The magnetizing inductance remains relatively constant under rotation, but the leakage inductance varies. This can be seen in Figure 2.13. The large variation in the leakage inductance is a result of the way that the end windings are removed from the coil [53].

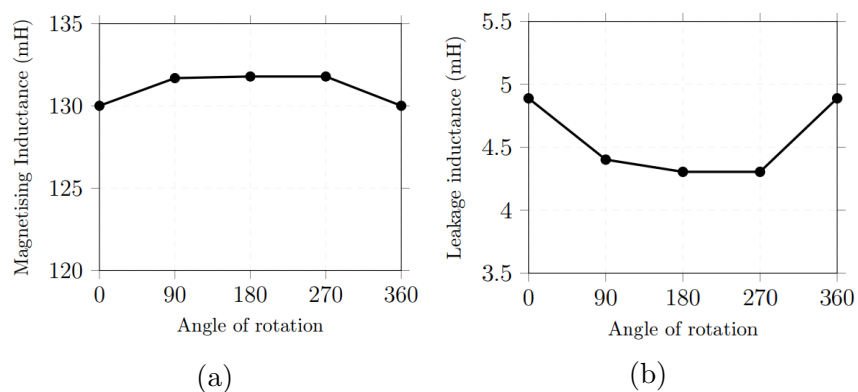


Figure 2.13: Effect of rotation on (a) Magnetising and (b) Leakage inductance [53]

The effect of rotation on the RT can vary between setups and construction methods. Additional care has to be taken when running a finite element analysis (FEA) to include the construction method to get the most accurate results.

2.10. Rotor cooling

In a conventional DFIG, most of the losses occur on the primary (stator) side. This allows for external cooling solutions such as large fin arrays, external fans, or liquid cooling [54]. In the rotor-tied DFIG the majority of the losses now occur on the rotor. Forced convection by a fan is a solution for small enough machines. The increase in rotor length for large machines, combined with the small air gap distance between the rotor and the stator, makes the rotor much more challenging to cool. The heat needs to be moved from the center to the outside of the rotor.

With the addition of an RT the removal of heat is even more crucial. Regular (stationary) power transformers are usually cooled with oil which is not a viable option for rotating machines due to the additional friction losses. The rotor shaft will now also be heated up by the losses of the transformer if they share the same shaft. If the RT and DFIG are two separate units, both will require active cooling when the machine's rating gets large enough. Detailed thermal modeling will be required before the rotor-tied DFIG and RT can be scaled up in size.

2.11. Summary

In this chapter the various design considerations and their effect was investigated. High efficiencies can be achieved as long as the losses in the RT are addressed. With the introduction of an air gap, the magnetizing inductance is lower which results in a higher magnetization current and increased conduction losses. The magnetizing inductance stays constant during rotation provided the air gap distance is maintained. The leakage inductance varies during rotation due to the increased separation of the primary and secondary windings. By utilizing a small enough air gap, the adverse effects on the inductances can be reduced.

To minimize the size of the RT, it is proposed to increase the transformer's frequency by changing the machine to a rotor-tied configuration. This allows for the removal of the power transformer between the grid and the DFIG, and subsequently increasing the overall efficiency of the system. Care must be

taken when a topology is chosen for the RT so that no additional torque is exerted onto the shaft. The combination of laminations and round geometry results in a non-optimal use of material, resulting in increased core volume. The DFIG in the rotor-tied configuration has to be cooled due to the increased power density on the rotor and the added RT.

Chapter 3

Three-phase RT design methodology

During the design stage of this study, it is necessary to develop an accurate analytical model of the RT. An accurate model will assist in prediction the RT performance and will result in an improved analysis when used in conjunction with an FEA model. The RT poses several design challenges such as the geometry and air gap. These design challenges are highlighted in Chapter 2.

A rotary transformer functions on the same basic principle as a standard transformer, namely inductive power transfer. The same conventional design process that is used in standard power transformers can be adapted and utilized on an RT. Due to the unique nature of the RT, it has specific characteristics which it does not share with a conventional transformer, such as an air gap. This air gap is required for the RT to rotate. The geometry of the RT has to be of such a nature that the rotation does not influence its capacity to transfer power efficiently. The rotation of a gapped core transformer can impact the dynamic characteristics of the power transfer and needs to be addressed in the design process.

The primary purpose of the RT is to replace the slip-ring and brush assemblies and make the power transfer contactless. The main constraints of such a contactless solution is size and efficiency. The design methodology discussed in this chapter aims to both minimize the size and maximize the efficiency of the RT. The framework of this method is based on conventional transformer design and optimization strategies, with additional measures to mitigate the effects as discussed in Chapter 2. To evaluate the design parameters and effects of the air gap, an analytical model which is described in this chapter is used in combination of a Finite Element Method (FEM) analysis.

Initial studies done on RTs [18, 23, 42, 43] shows that it is indeed possible to achieve acceptable levels of efficiency and stability during rotation. While

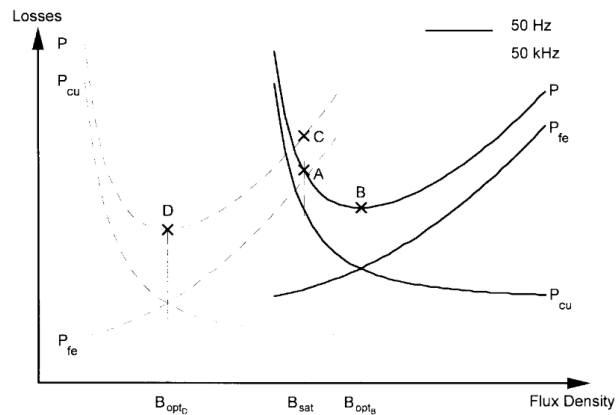


Figure 3.1: Iron and copper losses at different frequencies and their corresponding optimal flux densities. [55]

these studies indeed show that an RT can be used in a laboratory environment, continued development is required to overcome several effects. These effects are unique to the topology of the RT and mitigation methods need to be investigated. The most important effects that need to be considered during the design and optimization phase are:

- Low magnetization inductance due to the air gap
- Saturation of the core material at low frequencies
- High leakage inductance
- Non-optimal core size

The principle of maximizing a transformer's efficiency is based on selecting an operating point where both the core and copper losses are mitigated. Such a strategy is presented by Hurley [55] for both high and low frequency transformers. Figure 3.1 illustrates the effect that flux density has on the total power loss of the transformer. The method proposed is to choose the operating flux density as the saturation flux density. This allows for the maximum use of the core material while still retaining the highest efficiency even if the loading of the transformer is reduced.

The following sections present an analytical design methodology for the RT. It aims to mitigate the aforementioned effects during the design process.

3.1. Transformer design and loading parameters

Any transformer design starts with the required power rating and parameters. The transformer is designed initially when the loadings are set to a maximum. The minimum area product of the RT can be obtained from Equation (3.1), and it corresponds with the smallest size. To keep the transformer within an acceptable range of efficiency, the maximum current density is typically set between 3-5 A/mm^2 . To determine the initial magnetic loading, it is set to the saturation flux density of the material.

The steps that follow are an iterative process of lowering the loadings until an acceptable level of efficiency and size is obtained. This process can be automated and a multi-variable optimization like Pareto can be used to determine the optimal point where both size and efficiency are balanced. The general design steps that would be used to design a transformer are shown in Figure 3.2.

To optimize for efficiency, the size and loadings of the transformer need to be considered first. To minimize the size, the relevant parameters needs to be chosen for the transformer. To determine the transformer's power handling capability, the transformer's area product A_p is used

$$A_p = \frac{P_t \times 10^4}{K_u K_f B_o J f}, \quad (3.1)$$

where P_t is the apparent power of the transformer, K_u is the window utilization factor, K_f is the waveform coefficient (4.44 for a sine wave), B_o is the flux density in the core, J is the current density in the wire and f is the frequency.

From Equation (3.1) it can be seen that the size of the transformer is inversely proportional to the frequency (f), as well as the magnetic (B_o) and electric (J) loadings. Upon the selection of the main design and loading parameters, analytical solutions can be utilized to determine the remaining variables. Using Equation (3.1) the required area product A_p can be calculated, and it represents the core cross sectional area A_c and the window area A_w ,

$$A_p = A_c \times A_w. \quad (3.2)$$

Since both of these dimensions are unknown, an approximation must be used to set one of the constraints. The method discussed in [45] presents an empirical relation between emf/turn E_t and the output power of a set of standard transformers in the form of

$$E_t = K \sqrt{P_o}, \quad (3.3)$$

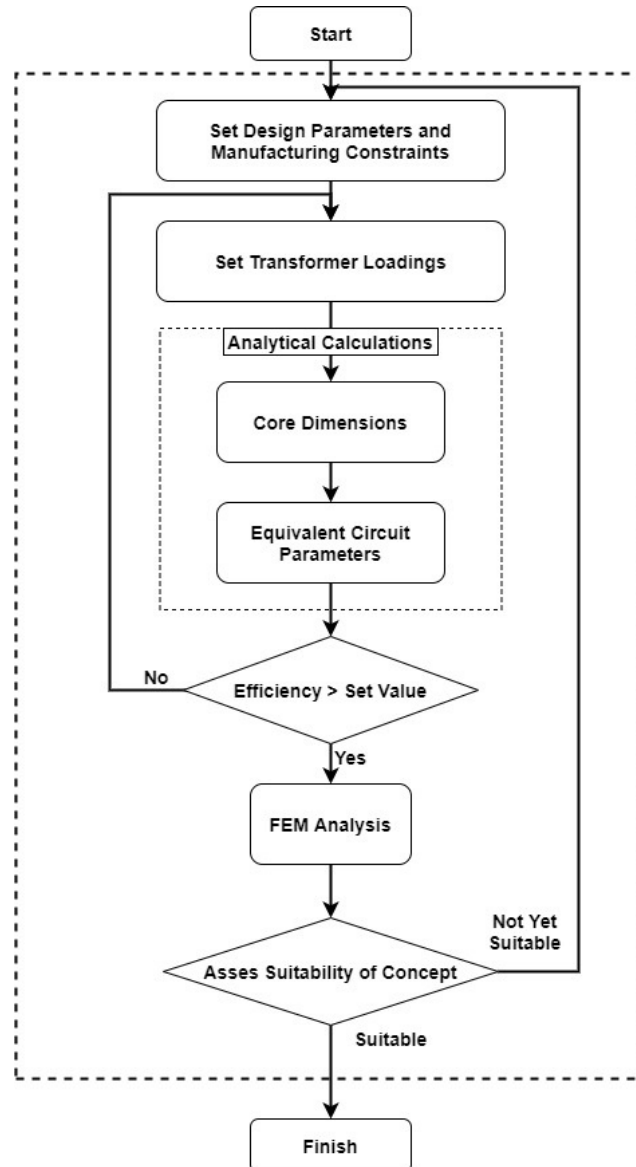


Figure 3.2: Flow chart illustrating the initial RT design outline

where $K = 1.0 - 1.2$ for a single-phase shell type transformer. This method is not the most reliable but gives a reasonable starting point for the design. Using the rearrangement of Faraday's law for the formula of the area of a core

$$A_c = \frac{1}{K_f B_o f, T_e} \quad (3.4)$$

with T_e being the amount of turns per volt (turn/emf), Equation (3.3) can be substituted to obtain the area of the core as

$$A_c = \frac{E_t}{K_f B_o f}. \quad (3.5)$$

The transformer window area A_w can be calculated by dividing the area product by the core area. The minimum number of primary turns can then be calculated by

$$N_p = \frac{V_p}{K_f B_o f A_c}. \quad (3.6)$$

Obtaining the secondary number of turns can simply be determined by the turns ratio of the transformer.

3.2. Single-phase shell type transformer equivalent model

To design a three-phase RT, the analytical model for a single phase has to be developed first. The chosen analytical model is one that is widely used in transformer design, namely the duality principle. The basis of the principle is the ability to represent a magnetic circuit as an equivalent electrical circuit. This allows for electrical analysis and optimization based on conventional methods.

The magnetic model of the RT can be built by determining the flux lines. The magnetizing and leakage inductances can be determined from the geome-

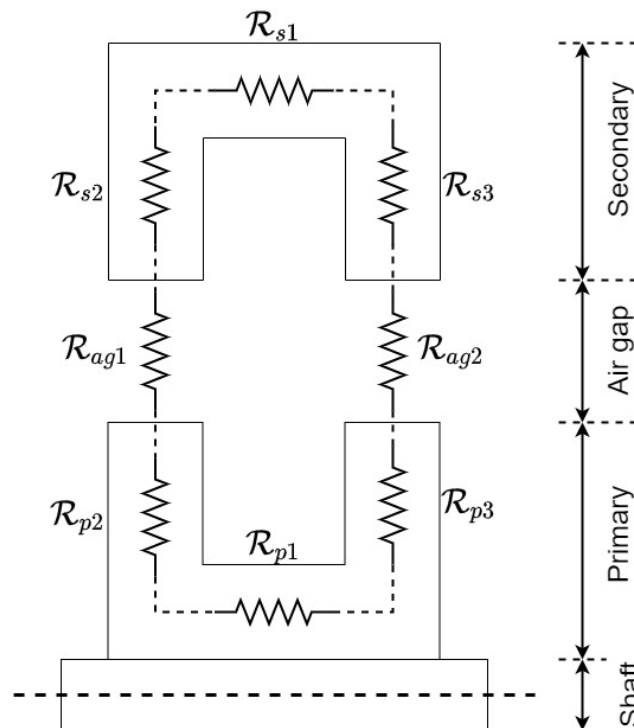


Figure 3.3: Reluctance model for single phase shell type rotary transformer

try of the transformer. The RT can be modeled in a similar manner to regular transformers with the inclusion of an air gap. The model can be used for any configuration of the air gap as long as the fundamental equations are derived for the specific geometry of the design. In this section we are looking at the single-phase shell type transformer with an air gap. The equivalent magnetic model is shown in Figure 3.3 with the flux lines shown as a dashed line.

To allow for electrical analysis, this circuit can be represented by an equivalent electrical circuit. This allows for design changes and optimization based on the electrical properties that is desired from the transformer. The resultant electrical circuit for the single phase, shell type RT is shown in Figure 3.4.

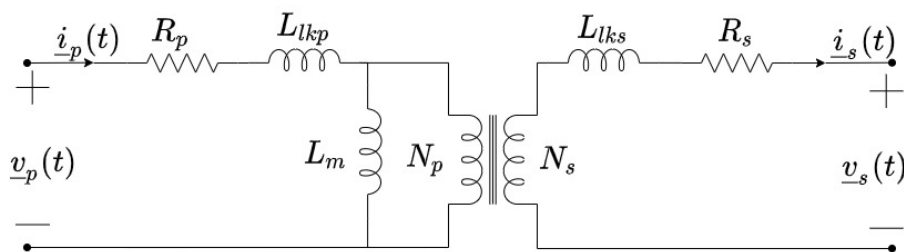


Figure 3.4: Equivalent single phase electrical circuit for RT

The electrical circuit consists of the winding resistance for the primary (R_p) and secondary (R_s) coils, the magnetizing inductance L_m and the primary ϕ_{lkp} and secondary ϕ_{lks} leakage inductance. The leakage induction represents the fraction of induced flux that does not reach the secondary coil. For transformers, this is affected the most by the distance between the primary and secondary coils. In a RT this is of particular importance as there needs to be an air gap to facilitate rotation between the two coils.

3.2.1. Winding resistances

The winding resistances are the easiest to determine. The resistance of the conductor is dependent on the length, resistivity, and area. For AC conduction through a wire, the resistance increases if skin effects are present. To determine the maximum conductor diameter that can be used and still neglect skin effect δ is

$$\delta = \frac{1}{\sqrt{\pi f \mu_o \sigma}}, \quad (3.7)$$

with f being the frequency, μ_o being the permeability of free space and σ being the conductivity of the material.

For a 50Hz current and a round single strand wire, the thickness needs to be less than around 20mm. If wire smaller than that is used the resistances can be determined by using the properties of the coil so that the resistance for the primary (R_p) and secondary (R_s) coils respectively becomes

$$R_p = \frac{N_p M L T_p \rho}{A_{wp}}, \quad (3.8)$$

$$R_s = \frac{N_s M L T_s \rho}{A_{ws}}, \quad (3.9)$$

with N_p and N_s being the primary and secondary number of turns, $M L T_p$ and $M L T_s$ are the primary and secondary mean length of turn. A_{ws} and A_{wp} are the cross-sectional areas of the conductors in the primary and secondary windings respectively and ρ is the resistivity of the winding material. For bundled wires this resistance can be worked out for a single strand and all of the strands can be assumed to be in parallel. Unlike standard electric machines there is no end winding calculation as it would only be a fraction of the total resistance.

3.2.2. Single phase RT Inductances

The inductance parameters of the RT are of significant importance as it will greatly effect the operating characteristics. To complete the equivalent circuit shown in Figure 3.4, the magnetizing and leakage inductances must be calculated. The magnetizing inductance can be computed by utilizing a reluctance network that is dependent on the geometry of the transformer. The reluctance model for the shell type RT is shown in Figure 3.3. The leakage inductance can be calculated from the energy stored in the windings and in the air gap. The following sections outline the procedure followed.

3.2.2.1. Magnetizing inductance

Using the principle of inductance of a coil discussed in Equation (A.8), the magnetizing inductance can be computed by

$$L_{mp} = \frac{N_p^2}{\mathcal{R}_{total}}. \quad (3.10)$$

The total reluctance \mathcal{R}_{total} in the network can be seen in Figure 3.5 and described by

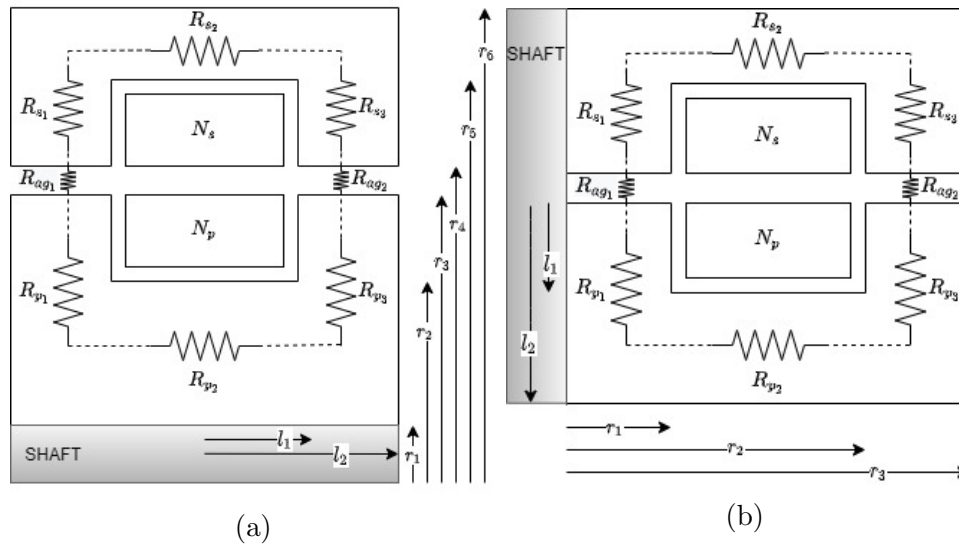


Figure 3.5: Axis-symmetrical reluctance model of the single phase (a) Axial air gap RT and (b) Radial air gap RT

$$\mathcal{R}_{total} = \mathcal{R}_{p1} + \mathcal{R}_{p2} + \mathcal{R}_{p3} + \mathcal{R}_{s1} + \mathcal{R}_{s2} + \mathcal{R}_{s3} + \mathcal{R}_{ag1} + \mathcal{R}_{ag2}. \quad (3.11)$$

The magnetization inductance of the transformer is almost entirely controlled by the air gap. Changes in the air gap distance will result in significantly affected reluctance, and in turn the magnetizing inductance and current. The magnetizing current can be estimated from the expected field intensity in the air gap. The field intensity will be subjected to fringing in the air gap that also has to be considered. The effective air gap area is also constrained by the topology of the RT and the layout of the laminations, considering that for certain configurations the core area on the primary side of the air gap does not equal that of the secondary core side. The estimated magnetizing current I_{mag} for a given field intensity in the air gap is presented by [45] as

$$I_{mag} = \frac{H\ell}{0.4\pi N_p}. \quad (3.12)$$

The core is separated into two sections, the rotor (primary) and stator (secondary), with each section consisting of three subsections each as shown in Figure 3.5. The reluctance of each subsection is dependent on the length of that section, its cross-sectional area and permeability. In a standard transformer the cross-sectional areas are usually rectangular and constant throughout the length of the element. Due to the unique nature and geometry of the RT's core, the geometric equations need to be considered carefully.

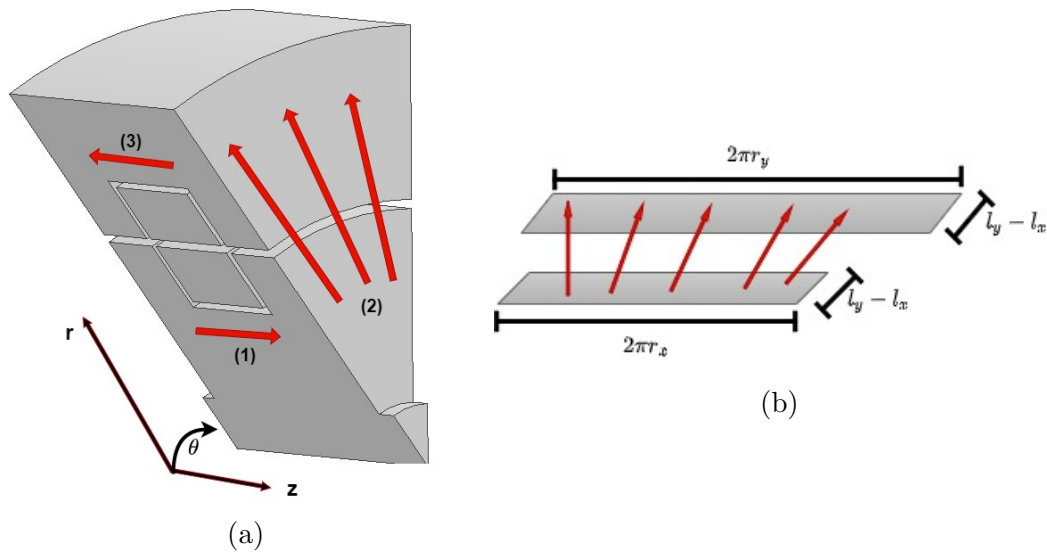


Figure 3.6: Representation of the flux path in the RT. (a) 3D section of the core indicating the flux path (1),(3) parallel to the shaft and (2) radial path across the air gap and (b) 2D cross section of flux path (2).

3.2.2.2. Axial air gap RT reluctance model

If the axial air gap topology is utilized by the design, the geometry that is used to evaluate the RT is in cylindrical coordinates. The cylindrical axis z is the axial component, r is the radial component and θ is the angle of rotation around the z axis.

The areas of the circular cross section in Figure 3.6 are a function of the primary and secondary window height and is given by

$$A_{p1} = \pi(r_2^2 - r_1^2), \quad (3.13)$$

$$A_{s1} = \pi(r_6^2 - r_5^2). \quad (3.14)$$

The primary and secondary window reluctances can be seen in Figure 3.5b. The reluctances can be calculated by substituting Equation (3.13) into Equation (A.6) to obtain

$$\mathcal{R}_{p1} = \frac{2l_1}{\mu_r \mu_o \pi (r_2^2 - r_1^2)} \quad (3.15)$$

$$\mathcal{R}_{s1} = \frac{2l_1}{\mu_r \mu_o \pi (r_6^2 - r_5^2)} \quad (3.16)$$

with μ_r being the relative permeability and μ_0 being the permeability of free space.

The radial reluctance components \mathcal{R}_{p2} , \mathcal{R}_{p3} , \mathcal{R}_{s2} , and \mathcal{R}_{s3} have cross-sectional areas that are not constant through the element. For flux in the radial direction r the area will change as a function of r . Equation (A.6) does not account for a change in area, which needs to be accounted for. If the standard method of triple integration for a volume of a cylinder is used, the area can be divided into differential elements as shown in Figure 3.6. The volume of a cylinder is

$$Volume = \iiint r dr d\theta dz. \quad (3.17)$$

In order to use Equation (A.6) the area must be derived from this volume and Equation (3.17) becomes

$$Area = \frac{\iiint r dr d\theta dz}{length}. \quad (3.18)$$

Using the differential element as shown in Figure 3.6b, the change in radial distance r brings changes to the angle of rotation and axial lengths. Evaluating Equation (3.18) for the change in radius from r_{y1} to r_{y2} , the change in axial length from l_{x1} to l_{x2} and the change in angle of rotation from θ_1 to θ_1 . This yields

$$Area = \frac{\int_{l_{x1}}^{l_{x2}} dz \int_{\theta_1}^{\theta_2} d\theta \int_{r_{y1}}^{r_{y2}} r dr}{r_{y2} - r_{y1}}. \quad (3.19)$$

The integrals in Equation (3.18) can be solved for the radial sections of the RT with the primary reluctances \mathcal{R}_{p2} and \mathcal{R}_{p3} . The geometry of these sections is shown in Figure 3.5a. Using Equation (3.19) to solve the areas of the radial sections A_{p2} and A_{p3} , yields a similar area for both

$$A_{p2} = A_{p3} = \frac{(l_{x2} - l_{x1})(2\pi)(\frac{1}{2}(r_{y2}^2 - r_{y1}^2))}{(r_{y2} - r_{y1})}. \quad (3.20)$$

Using the geometry shown in Figure 3.5a, Equation (3.20) resolves to

$$A_{p2} = A_{p3} = \frac{\pi(l_2 - l_1)(r_3^2 - r_2^2)}{(r_3 - r_2)}. \quad (3.21)$$

Similarly, Equations (3.18) and (3.19) can be solved for the radial regions in the secondary core to yield

$$A_{s2} = A_{s3} = \frac{\pi(l_2 - l_1)(r_5^2 - r_4^2)}{(r_5 - r_4)}. \quad (3.22)$$

Using the resulting areas and substituting them into Equation (A.6) gives the reluctance for the primary core

$$\mathcal{R}_{p2} = \mathcal{R}_{s3} = \frac{(r_3 - r_2)}{\mu_r \mu_o \pi (l_2 - l_1)(r_3 + r_2)}, \quad (3.23)$$

and for the secondary core

$$\mathcal{R}_{s2} = \mathcal{R}_{p3} = \frac{(r_5 - r_4)}{\mu_r \mu_o \pi (l_2 - l_1)(r_5 + r_4)}. \quad (3.24)$$

To determine the reluctance of the air gap, the fringing effect has to be considered. Various methods proposed [56, 57] attempt to model the air gap reluctance more accurately. The most common technique used is to increase the area of the air gap. The amount of fringing compensation ranges from 5% to adding the length of the air gap to either side of the air gap region. Neither of these methods are completely accurate for an unequal fill factor during rotation at either side of the air gap. Taking the classic approach of adding the length of the air gap l_{ag} to the side yields

$$l'_2 = l_2 + l_{ag} = l_2 + (r_4 - r_3). \quad (3.25)$$

The air gap reluctance with the compensated area can now be given by

$$\mathcal{R}_{ag1} = \mathcal{R}_{ag2} = \frac{(r_4 - r_3)}{\mu_o \pi (l'_2 - l_1)(r_4 + r_3)}. \quad (3.26)$$

3.2.2.3. Fill factor correction for radially laminated cores

The laminations are stacked in such a manner that the conventional core areas cannot be used to obtain an optimal design. The air gap will be unique in the sense that the rotor and stator will not have the same fill factor at the air gap. This result in a lower usable air gap as the flux from the rotor will only cross a portion of the air gap efficiently. The effective air gap has to be assumed to be smaller than the actual air gap due to the inefficient use of the magnetic material of the stator at the air gap. The inclusion of filler laminations will greatly increase the effective air gap and is a solution that should be considered for the rotor.

To correctly model the core, the air gap between the laminations need to be taken into effect. This can significantly affect the magnetizing inductance of the core. The traditional method is by using a stacking factor for the laminations. The stacking factor represents the amount of active material in the space.

Depending on the construction of the laminated core the laminations will not have the same stacking factor for the primary and secondary regions. The

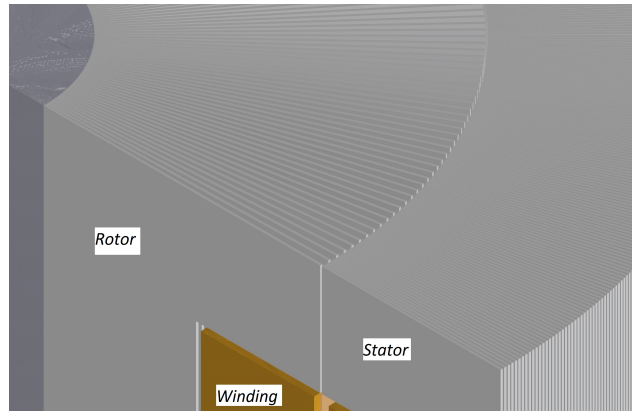


Figure 3.7: The decreasing fill factor of the laminations on the rotor for the radially stacked RT

primary side has a much smaller radius than the secondary side. The stacking can be seen for a radially laminated core in Figure 3.7. The stacking factor for each region can be calculated by

$$Fill\ factor = \frac{Actual\ area\ filled\ by\ lamination}{Theoretical\ area\ of\ the\ region}. \quad (3.27)$$

If the inner lamination fill factor of 0.95 can be achieved, the outer fill factor will be much lower. This is especially important in the rotor since the lamination density in the air gap will not be the same for the rotor and stator. This poses a difficult design and evaluation problem as the flux would have to go from one lamination in the rotor to several laminations on the stator. This sees an effective increase in the air gap distance that the total flux would have to travel. One of the proposed solutions to this is the addition of filler laminations. This decreases the distance of the effective air gap and increases the total magnetic material. The effect of the filler lamination is more pronounced if the ratio between the rotor and stator fill factors is significant. Figure 3.8 shows the flux path for the radially stacked RT with and without filler laminations.

For the radially stacked RT the fill factor of the laminations K_{fill} changes with radius to the extent of

$$K_{fill_o} = \frac{n_{lam} d_{lam}}{2\pi r_o}, \quad K_{fill_i} = \frac{n_{lam} d_{lam}}{2\pi r_i} \quad (3.28)$$

with n_{lam} and d_{lam} being the amount and thickness of the laminations respectively. For the case without filler laminations this becomes

$$K_{fill_o} = K_{fill_i} \left(\frac{r_1}{r_3} \right). \quad (3.29)$$

The flux passes through only the primary lamination and then splits once it reaches the secondary laminations. This causes a low flux density in the stator side with a lot of the material left unused. A design like this requires adjustments to the design equations as most of the air gap is not actually usable. The effective usable air gap as seen from the primary side then becomes

$$A_{e_{ag}} = \pi r_1 \cdot (l_2 - l_1) \cdot (1 + AG_f) \quad (3.30)$$

with r_1 , l_1 and l_2 shown in Figure 3.5. The air gap correction factor AG_f is a function of how large the air gap is in relation to the lamination thickness. Larger air gaps will have a larger correction factor as the flux will distribute more on the stator.

In the case of equal number of filler laminations as rotor laminations, the effective usable air gap essentially doubles. This would increase the total power capability of the RT if the stator laminations were sized according to the rotor having filler laminations in it. The better flux distribution in the air gap makes better use of the stator laminations at the air gap, which will result in a lower magnetizing current. The effect of the filler laminations can be seen in Figure 3.8.

The stacking factor can be utilized to reduce the area used in the reluctance calculations once the geometry and lamination thickness and layout are chosen in this study's design section. This will reduce the active area of the core and give a more accurate model. The air gap reluctance can be modified to include the effect of this lower fill factor. This can be achieved by adding half of the length of the air gap to the flux path through the air gap. The resulting reluctance for the air gap becomes:

$$\mathcal{R}_{ag1} = \mathcal{R}_{ag2} = \frac{1.5(r_4 - r_3)}{\mu_o \pi (l'_2 - l_1)(r_4 + r_3)}. \quad (3.31)$$

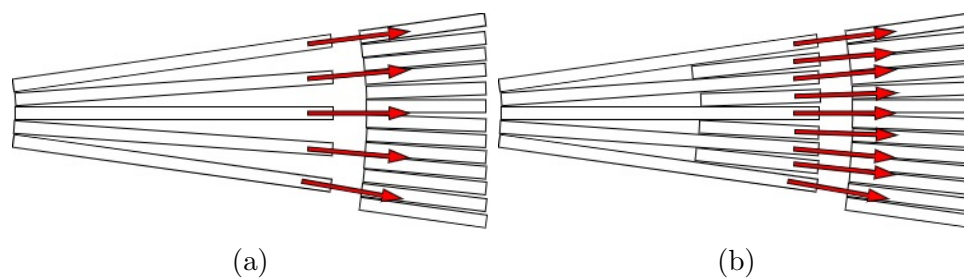


Figure 3.8: Flux vector plot of the radially stacked core (a) Without filler laminations and (b) With filler laminations

3.2.2.4. Leakage inductance

The leakage inductance in the RT is mostly determined by the distance between the two coils. Since one coil rotates in relation to the other, an air gap is required. This increases the distance between the coils. Additional factors such as the winding insulation will also increase the leakage inductance. This can be partially compensated for by increasing the width of the coil.

If all the field intensities (Equations (A.18) to (A.20)) are combined and substituted into Equation (A.21), the total stored energy can be found. This expression can in turn be substituted into Equation (A.16) to yield the total leakage inductance

$$L_{lk} = \frac{\pi(r_5 + r_2)N_p^2}{2l_2} \left[(r_4 - r_3) + \frac{(r_5 - r_4) + (r_3 - r_2)}{3} \right] (10^{-9}) \quad (3.32)$$

for the radially laminated, axial air gap RT with the adjacent winding configuration. The leakage inductance can be split up for the primary

$$L_{lkp} = 0.5 \times L_{lk}, \quad (3.33)$$

and secondary side

$$L_{lks} = \frac{0.5}{a^2} \times L_{lk}, \quad (3.34)$$

with a being the turns ratio.

3.3. Single phase RT core configurations

To evaluate the core layout for the three-phase RT, a single-phase model has to be analyzed first. The RT can consist of either three single phase RT's or a single core with three phases. As previously discussed, the two main constraints in the RT are the separation of windings and an air gap to facilitate rotation.

3.3.1. Radially laminated single phase core dimensions

From previous research [17, 18, 49], it was shown that the air gap has to be as small as practically viable, as it increases the magnetizing inductance. A smaller air gap is also beneficial to the separation of the windings, since it reduces leakage inductance. With a narrow window area, the core winding area has to be deeper, which result in the overall windings being further apart from each other. Reducing the number of winding layers by increasing the window width is paramount to reducing the overall leakage inductance. The

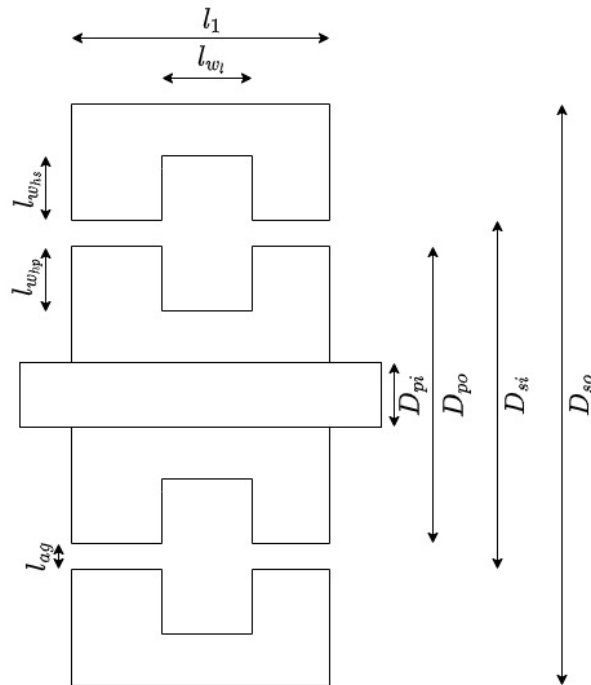


Figure 3.9: Geometry of the axial air gap single-phase RT with adjacent windings

window area can therefore be adjusted by the ratio δ between the window length l_{wl} and the window height l_{wh}

$$A_w = l_{wl} \cdot l_{wh} = \frac{l_{wl}^2}{\delta}. \quad (3.35)$$

The stacking of laminations and lamination direction significantly affects the active material in the core. If the laminations are placed radially outwards along the shaft, it reduces the amount of active material at the outer diameter of the core significantly. If sectioned laminations are used, i.e., axially and radially, there will be a discontinuity between the sections that act as additional air gaps. This reduces the magnetizing inductance of the core and needs to be accounted for in the model presented in the previous section. The analytical model needs to be adjusted for these air gaps between the laminations.

The dimensions that govern the outer diameter and length of the RT are proposed by [19]. The equations are valid for radially placed laminations and consider the material discontinuity by working with the inner core dimensions where the laminations are entirely flat with no gaps. The dimensions are shown in Figure 3.9. The inner diameters are indicated as D_{pi} and D_{si} for the primary and secondary sides respectively.

The dimensions of the RTs outer diameter and length are a function of the inner shaft diameter. The relationship was evaluated by [53], and it was observed that the outer diameter of the RT remains largely unchanged with the increase in inner shaft diameter. With the increase in shaft diameter, the overall length of the RT is reduced. The relationship shows the advantages of using a larger inner diameter to minimize the size of the RT. This has the added benefit of utilizing less core material and reducing the cost. The relationship presented by [53] is shown in Figure 3.10.

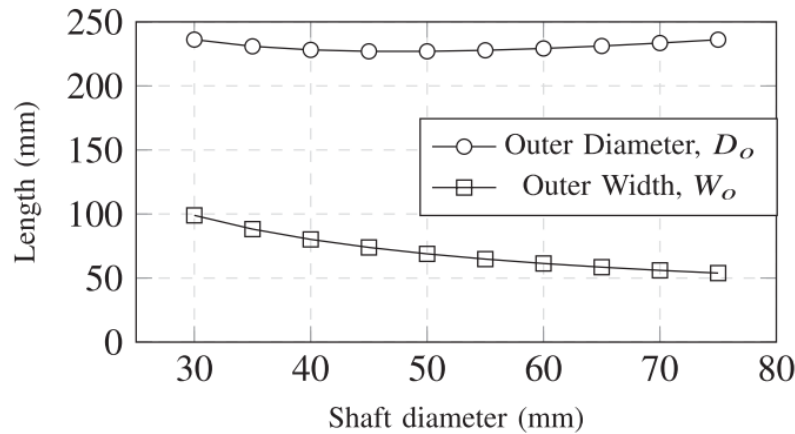


Figure 3.10: The outer dimensions of a 1.2kVA single phase RT with the change in shaft diameter [53]

The dimensions of the RT can be determined with the above-mentioned considerations in mind. The window area needed for the windings can be calculated based on the current density, the required number of turns, and a chosen fill factor. The primary core's outer diameter D_{po} is a function of the inner diameter D_{pi} and the minimum core cross-sectional area A_c . The required outer diameter is

$$D_{po} = \frac{2 A_c}{\pi D_{pi}} + (D_{pi} + 2l_{w_{hp}}). \quad (3.36)$$

Similarly, the outer dimension for the secondary core is

$$D_{so} = \frac{2 A_c}{\pi (D_{po} + 2l_{ag})} + (D_{po} + 2l_{w_{hs}} + 2l_{ag}). \quad (3.37)$$

The outer width of the core for a single phase l_o are the same for the primary and secondary side, and can be calculated as

$$l_o = \frac{2 A_c}{\pi D_{pi}}. \quad (3.38)$$

The air gap l_{ag} between the primary and secondary cores is yet unknown. To increase the magnetization inductance and reduce leakage inductance, a small air gap should be chosen. The initial estimate is based on manufactured prototypes by [19] and [42]. The air gap is initially chosen as 0.4mm for mechanical reliability. This air gap distance should be evaluated in the FEM analysis as well as the analytical circuit analysis. Increasing the air gap could potentially result in a more suitable design due to the decrease in manufacturing costs from allowing for larger tolerances at the expense of magnetizing inductance.

3.3.2. Combined lamination core dimensions

As stated in the previous section, the layout of the laminations will affect the overall size and efficiency of the transformer. If a combination of radial and rolled laminations can be used, a fill factor close to one can be achieved on the core area. This method will significantly change the fundamentals of the rotary transformer core, as the flux will be guided rather than flowing in its natural path. This can have significant advantages to the size, but a decrease in efficiency could result in the laminations needing to meet each other perfectly at each of the points. This topology of RT was first presented by [18] and features a 97% stacking factor as seen in Figure 3.11.

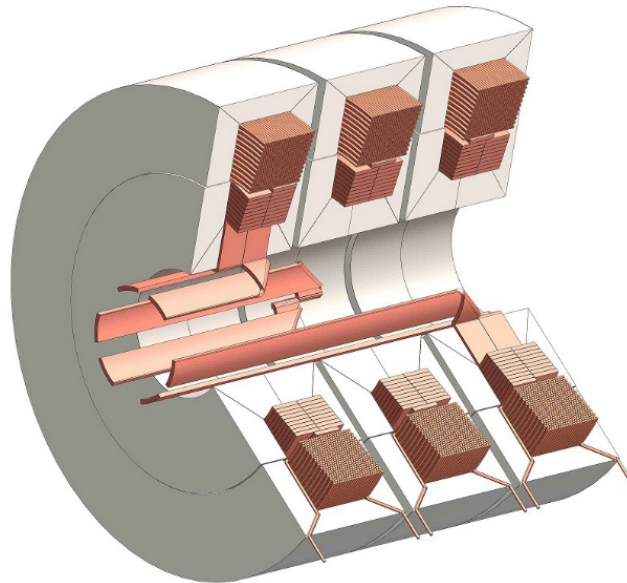


Figure 3.11: Proposed three-phase RT with combined laminations [18]

The advantages of this type of construction lies within the inherent nature of aligning laminations with the direction of the flux. This allows for a higher fill factor but does mean that at least different directions of laminations need

to be used. The inner and outermost parts can be made from rolled sheets of laminations that have a machined edge to form a trapezoidal shape. The radial portion of the core is created by machining a corresponding edge to a series of disk-shaped laminations. These are constructed by joining a series of laminations stacked together, similar to conventional electric machine laminations.

With this alternative method of placing the laminations, the equations in the previous section are no longer valid. New geometric equations need to be derived for each of the laminated parts. Using the same area product A_p from Equation (3.1), and number of primary turns from Equation (3.6), a starting point can be chosen. With the current density set, a standard wire size can be chosen. With this information the required winding area A_w can be calculated as well as the new core area A_c from the area product A_p (equation 3.2).

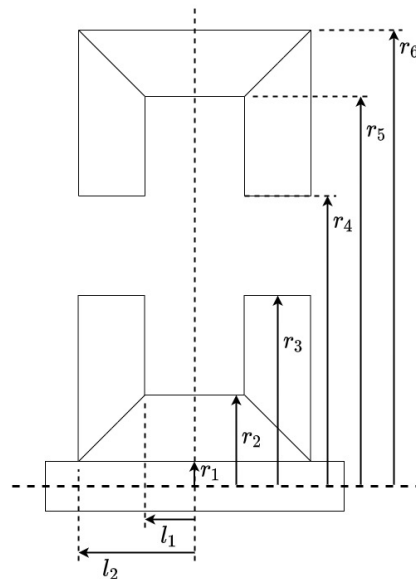


Figure 3.12: Geometry of the axial air gap RT with combined rolled and stacked laminations, in the adjacent winding topology

The new dimensions for the rolled laminations on the primary side becomes

$$r_2 = \sqrt{\frac{A_c}{\pi} + r_1^2}. \quad (3.39)$$

The outer diameter of the primary side of the lamination is

$$D_{po} = 2(r_2 + l_{w_{hp}}), \quad (3.40)$$

with $l_{w_{hp}}$ being the depth of the primary winding window. The depth is a function of the winding ratio δ and the required winding area A_w . A reasonable ratio for δ is around 3:1 to reduce the leakage inductance by making the

winding area wider than it is deep. Equation (3.35) shows the ratio between the winding depth and width.

The outer length $2\ell_2$ of the transformer needs to be evaluated in a fundamentally different way. The core area of the transformer is continuously changing in the stacked laminations as a function of the radius. This is a phenomenon unique to this type of RT construction and therefore there are no clear guidelines as to methods of mitigating this effect.

There are two primary methods of choosing the way that the stacked laminations are produced. The first method is to keep the area constant but will result in an expensive and over-complicated design. The second is to choose one dimension and the core area will increase as the flux moves to the secondary side. This has significant advantages in terms of manufacturing but can result in lower flux densities on the secondary core. This means that the transformer has magnetic material that will not be fully utilized. This increases the cost of materials and the overall weight of the transformer.

In this design the secondary option was selected. When the core area is being evaluated, the more conservative approach is to select the area at the innermost point of the transformer, i.e., r_1 . This will result in the least likelihood of the corners saturating at full load. To save on magnetic material and by selecting a more conservative starting flux density the outer length of the transformer is evaluated at the bottom of the winding at r_2 ,

$$\ell_o = 2 \left(\frac{A_c}{2\pi r_2} + \ell_1 \right). \quad (3.41)$$

The dimensions for the secondary side is evaluated in a similar manner as on the primary side. Since the outer diameter has already been set, the inner diameter of the secondary side D_{si} is

$$D_{si} = D_{po} + 2\ell_{ag}. \quad (3.42)$$

The winding dimensions for both the primary and secondary are the same since they have an equal number of turns. The outer diameter D_{so} can be calculated as

$$D_{so} = 2\sqrt{\frac{A_c}{\pi} + r_5^2}. \quad (3.43)$$

The air gap is still set at 0.4mm for mechanical reliability.

3.4. Three-phase RT core configurations

The three phase RT can consist of a number of different configurations. In this section the layout of the RT will be compared by using three separate single phases and using a single core with three phases.

3.4.1. Three single phase RT's in a three-phase system

The first type of core configuration is by using single phase RT's on the same shaft. They can either be stacked along the length of the shaft or radially on top of each other. The configuration along the length of the shaft is the more optimal choice as it is easier to construct, and all three phases will be identical. The radially outward stack can cause an imbalance due to different winding lengths and core dimensions. Previous work done by [17,19] proposed the use of three single phase RT's along the length of the shaft.

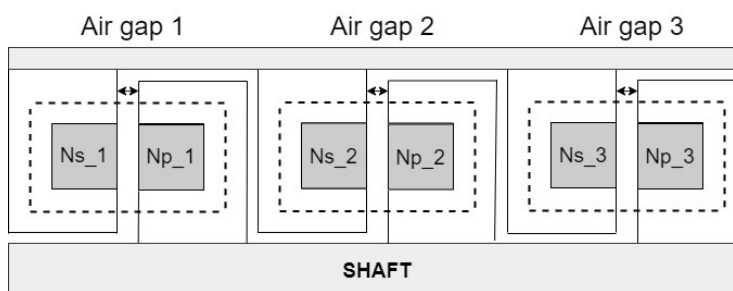


Figure 3.13: Three-phase configuration of single-phase RTs with radial air gap stacked along on the shaft

The cores can either be the radial or axial air gap configuration. The radial air gap configuration is shown in Figure 3.13. It has a more complex mechanical design and will result in a more expensive prototype. This is offset by the fact that the design will have reduced leakage flux as the windings can be placed closer to each other. This can improve the electrical characteristics of the RT. The axial air gap configuration is similar to how conventional electric machines are built and is a lot simpler in terms of assembly and manufacturability and is shown in Figure 3.14.

3.4.2. Single core RT with three-phase windings

To obtain a higher power density and decrease the manufacturing cost the three-phase RT can also be constructed using a single core. Due to the nature

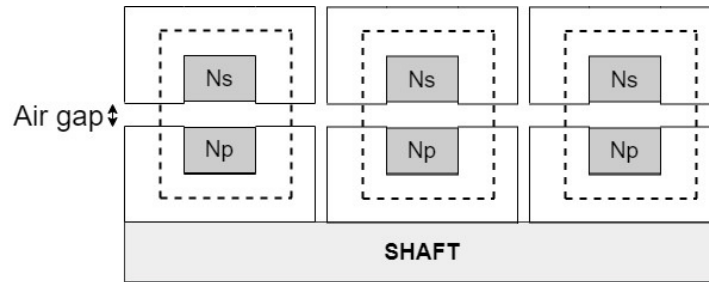


Figure 3.14: Three-phase configuration of single-phase RTs with axial air gap stacked along on the shaft

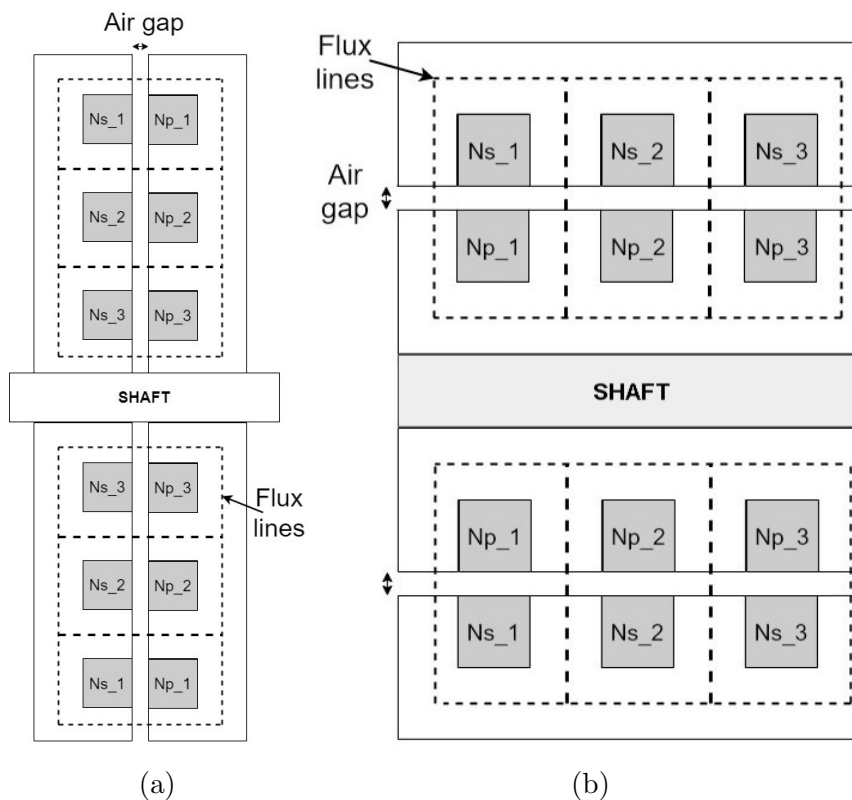


Figure 3.15: Three-phase RT with a single shared core in the (a) Radial air gap, and (b) Axial air gap configuration

of the air gap the RT is of a shell type transformer construction and has four limbs. The two limbs on the inside are larger than those on the outside due to flux from two phases. In this configuration the middle winding has to be wound in the opposite direction of the outer windings due to the mutual flux and the phase shift.

The topology with the radial air gap is difficult to achieve during the de-

sign phase. With the increase in the radial direction the effective air gap area increase and it can be difficult to match the electrical characteristics of each phase. The construction is relatively simple, and a low leakage flux can be obtained since the windings can be very close to each other. This does result in a larger outer diameter compared to the axial air gap topology. The constraint on space depends on the application specific requirements. The topology can be seen in Figure 3.15a.

The axial air gap topology with a single core is the most desirable layout for the three-phase RT. It has a single core and an air gap that is similar to conventional electric machines. Similar to the axial air gap topology, the middle coils winding direction needs to be reversed. This configuration does present a more difficult secondary winding construction as it would need to be very stiff as it is not supported at the air gap side. If the coil is not perfectly round, the leakage inductance will increase, reducing the power factor of the RT. Special care has to be taken to ensure the same air gap distance is maintained throughout the length of the shaft as it would unbalance the phases in this configuration. The topology is shown in Figure 3.15b.

3.5. Material selection

The selection of the core material will greatly influence the magnetic characteristics of the RT. As discussed in Chapter 2 the use of laminations is required to mitigate the effects of eddy currents. It is vital to select a material with the proper characteristics to reduce loss and cross conduction.

The appropriate selection of winding material is also crucial as the windings on the rotor will be difficult to cool and will experience high operating temperatures. The resistance of the material will increase with temperature so the appropriate current density and material should be selected to minimize conduction losses.

3.5.1. Lamination selection

In any transformer there needs to be a core material to help facilitate the flow of induced flux for better magnetic coupling between the sets of windings. This is usually done with ferromagnetic materials. These materials can either be in the form of electrical steel or ferrite materials. Ferrite materials have advantages such as higher resistivity and that they can accommodate higher frequencies. They are smaller in size because of the frequency increase and have a much better power density. At lower frequencies such as 50/60 Hz, the

use of ferrites is limited due to their low saturation points. At these frequencies the more appropriate material is electrical steel.

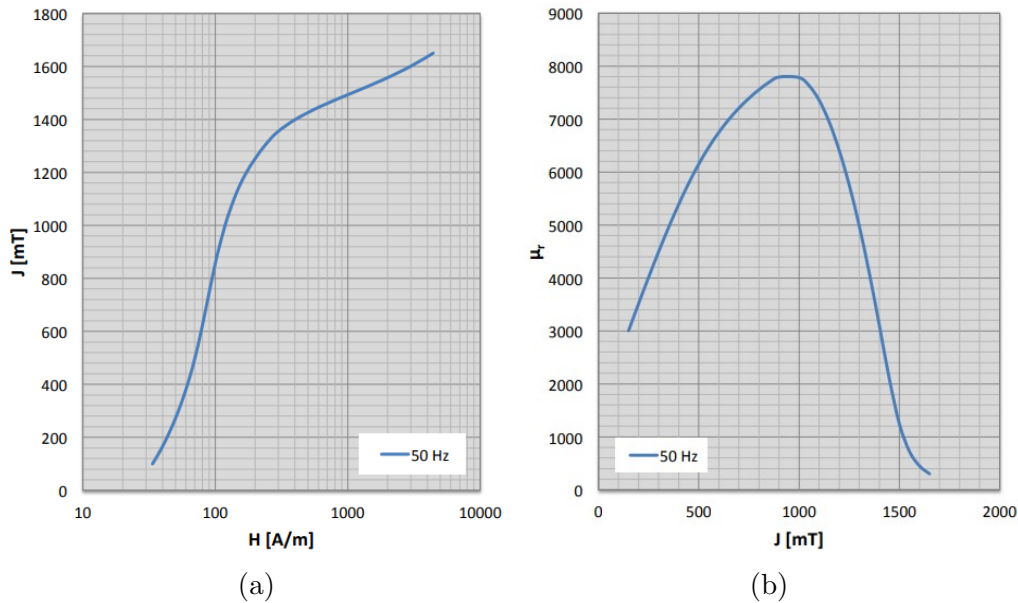


Figure 3.16: M400-50A electrical steel (a) Flux density vs field intensity, (b) Relative permeability vs flux density

Electrical steel come in many different configurations for both their physical shape and electrical properties. There are several alloy steels to choose from, each with their own magnetization curve. To limit eddy effects at this frequency, laminations are used in parallel to the flux direction. This results in several thin sheets of an alloy steel. Laminations are available in both grain-oriented and non grain-oriented configurations. For the radially stacked designs, the flux path will not always be in the direction of the steel, so non grain oriented laminated steel has to be used. In the rolled and stacked lamination layout grain-oriented steel can be used.

As discussed in Section 2.8, the air gap significantly affects the BH curve of the magnetic material. There is similar energy loss for both, but the field intensity required to achieve the rated flux density is much higher. Since the air gap will be the main constraint when it comes to field intensity, a material should therefore be selected that reaches an appropriate flux density at the specific field intensity.

The maximum size for the lamination thickness is dependent on the skin effect of the eddy currents. Using thicker sheets of laminations will reduce the

manufacturing time and complexity at the cost of higher core losses. Thinner sheets are more beneficial and will reduce the total losses experienced by the RT [58]. For a 50Hz transformer the ideal lamination thickness is 0.3mm.

The selected material is the M400-50A electrical steel with a thickness of 0.5mm. It is a non grain-oriented steel with reasonably low core losses at 50 Hz. It also has a good relationship between field intensity and induced flux which can be seen in Figure 3.16. Finally, the relative permeability lowers rapidly when the material starts to saturate, which will help increase the total reluctance in the core. It is also selected for its cost as it is a widely available lamination standard. Thinner sheets of laminations such as 0.35mm are not cost-effective in South Africa.

3.5.2. Winding material

An important part of selecting a winding, is to achieve the correct current density required in the transformer. From Equation (3.1) it can be seen that decreasing the current density results in a larger area product for the transformer. This leads to higher costs due to the increased material usage. A high current density will lead to higher loss and could result in the transformer operating at a below desirable efficiency.

To reduce costs and enhance the feasibility of the transformers coil, a winding material that is commonly available should be used. The most common type of conductor materials are copper, silver and aluminum. Each of these materials have their own advantages such as a lower weight for aluminum and a lower resistance for silver. The most inexpensive of the materials is aluminum wire with silver wire being the most expensive. Since silver wire is not commonly available and is costly, it is excluded from the available materials that can be used in the design. The comparison between copper and aluminum wire can be seen in Table 3.1.

Table 3.1: Winding material comparison

	Copper	Aluminum
Resistivity (Ωm)	1.72×10^{-8}	2.83×10^{-8}
Density (g/cm ³)	8.91	2.7
Relative price (\$/kg)	2.9	1
Conductivity: Equal Volume (%)	100	44

The most common type of conductor is the circular copper wire, and it is available in standard sizes with varying levels of insulation. The windings should be chosen to be below the set current density, but still fit into the winding area. A multi-strand wire with a thin insulation layer can be used in this design, as it reduces potential eddy current effects as well as allowing for large amounts of turns. For space critical applications such as electrical machines, enameled copper wire is the most suitable option for power density. The number of turns can be calculated from Equation (3.6).

3.6. Core loss model for the three-phase RT

The primary losses in a transformer core are conduction, hysteresis, and core losses. The resistive (conduction) losses in the windings can be calculated from OHM's law as a function of the winding resistance R and current through the coils I in the form of

$$P_r = 3k_t k_w (I_p^2 R_p + I_s^2 R_s). \quad (3.44)$$

The subscripts p and s denote the primary and secondary side. k_w is a compensation factor for other minor effects such as the skin- and proximity effects. k_t is the thermal modifier for the specific material chosen to compensate for the increased resistance at high operating temperatures.

The second type of losses is eddy current loss in the core. The loss can be described by

$$P_e = K_e B_m^2 t^2 f^2 V, \quad (3.45)$$

with the volume V of the core with dimensions shown in Figure 3.5 being

$$V = \pi \times 2l_2(r_2^2 - r_1^2 + r_6^2 - r_5^2) + 4\pi(l_2 - l_1)(r_3^2 - r_2^2 + r_5^2 - r_4^2), \quad (3.46)$$

The loss coefficient K_e is an analytically derived value for the type of electrical steel and the construction of the core [59]. B_m is the peak flux density in the core. The lamination thickness t and the frequency f play a large role in the magnitude of the losses, and in both situations it should be reduced. Since the core needs to operate at the grid frequency of 50Hz, the only variables that can be controlled are the construction and the type and thickness of the laminations. The manufacturers data sheets often list the total core loss at a specific flux density for a specific weight of laminations. This losses include the hysteresis losses. The loss can then be estimated with their factor P_s as

$$P_c = P_s V \rho, \quad (3.47)$$

using the volume of the core and the specific weight of electrical steel ρ .

If the manufacturers data sheets are not used to include hysteresis effects it can be estimated by

$$P_h = \eta B_{peak}^n fV, \quad (3.48)$$

where η and n are the Steinmetz hysteresis coefficient and exponent respectively [59]. The total core loss is the combination of the losses in the form of

$$P_{loss} = P_r + P_e + P_h, \quad (3.49)$$

or with the manufacturer's tested core loss coefficients as

$$P_{loss} = P_r + P_c. \quad (3.50)$$

This total loss of the RT in W can be used in the analytical calculations for efficiency as well as a starting point for the thermal design.

3.7. Thermal design

In the case of any design that generates heat as a function of other losses, the thermal effects of the design needs to be considered to ensure that the design does not exceed its expected operating range. In the design of the RT, the electrical steel laminations have temperature effects that could play a role in the efficiency of the transformer. Secondly the winding temperature is important as very high temperatures could lead to permanent damage of the winding insulation, or the increased degradation over time.

In this chapter we first investigate the steady state heat transfer of the RT, to determine what equilibrium temperature would be for the core and the windings. Second, we determine if natural convection is enough or whether additional cooling would be required to ensure long term stable operation of the RT.

3.7.1. Natural convection

With the previous section discussing the losses of the system, we have an estimated amount of heat that would need to be dissipated at full load. Using these parameters, we can determine the temperature at the surface of the RT when it is in a steady state. The primary methods of heat transfer from the surface of the RT are convection and radiation. Due to the large rate of thermal conduction within steel, the inner portions of the RT would be within a few °C of the external temperature. As long as the surface temperature of

the RT is within reasonable range, the inner parts can be assumed to be sufficiently cooled since conduction is usually magnitudes higher than convection.

The steady state heat transfer rate of convection of the RT, \dot{Q}_c , can be described by

$$\dot{Q}_c = hA_s(T_s - T_\infty), \quad (3.51)$$

with A_s being the surface area, and T_s, T_∞ being the surface and air temperature respectively. The heat transfer coefficient of the RT h can be calculated by using Equations (C.1) to (C.4), and is dependent on the air properties, orientation of the RT, and smoothness of the surface.

3.7.2. Radiation heat transfer

Radiation heat transfer is a form of electromagnetic radiation that does not require a medium for energy transfer. Radiation heat transfer between two objects will always occur if there is a difference in temperature between them. As the radiation meets the surface of an object, some of it may be transmitted through and some may be reflected back. The rate of which energy is absorbed is denoted by the absorptivity of the material β , the reflectivity by η and the transmissivity by κ . The sum of these is always equal to one.

The overall heat transfer coefficient is defined as

$$\dot{Q}_r = \epsilon_{thr}\sigma_{SB}(T_1^4 - T_2^4)A_s, \quad (3.52)$$

with the rate being dependent on the relative emissivity ϵ_{thr} , temperature difference and surface area. The derivation of the formula is shown in Equations (C.5) to (C.9).

Radiation heat transfer has a significant impact on the total heat transfer of a system if only natural convection is used. If a fan is present in the system, the rate of heat transfer from forced convection often vastly exceeds that of radiation. The emissivity of the transformer can be increased significantly by painting it. The relative emissivity of electrical steel is $\epsilon_{thr} = 0.3 - 0.6$.

3.7.3. Conduction heat transfer

In the previous sections we considered the heat transfer from the surface of the RT. To accurately determine the temperature of the inside components such as the windings, the conduction heat transfer between the surface and inner windings need to be determined. Conduction is the heat transfer through solid materials.

Since the RT consists mainly of copper wires and electrical steel for the core, the majority of heat will need to be conducted to the surface. The air gap

between the primary and secondary side of the core does pose a problem for cooling the inner part of the core. The air gap is very small and externally forced convection is difficult to achieve.

The primary concern of the conduction analysis is the steady state temperatures of the windings and the core material. The windings will therefore be the hottest part in the RT, and cooling optimization should be focused on reducing the temperature to extend the lifetime of the windings. The heat that is generated in the windings can be determined from the section on conduction loss. The heat is estimated to be equally distributed between the windings and it will be analyzed as a lumped model with the entire winding being at the same temperature. The same holds true for the primary and secondary core.

Since copper and electrical steel have stable thermal conductivity and expansion at the temperature range we consider, these properties can be assumed to be constant. There are multiple heat sources and as long as the heat transfer of conduction vastly exceeds that of the convection and radiation, the temperature difference is all that is required. The rate of heat transfer in cylindrical coordinates is

$$\dot{Q}_{cond_{cyl}} = -kA \frac{dT}{dr}. \quad (3.53)$$

Since this area changes with the radius, separating the variables and integrating from r_1 to r_2 where $T(r_1) = T_1$ and $T(r_2) = T_2$ gives

$$\dot{Q}_{cond_{cyl}} = 2\pi Lk \frac{T_1 - T_2}{\ln(r_2/r_1)}. \quad (3.54)$$

Combining these equations to have a complete heat transfer model is useful in determining the hottest part of the RT.

3.7.4. Internal forced convection

To facilitate additional cooling on the rotating (inner) core, forced convection through the shaft can be used. This allows for heat removal on the surface of the RT as well as from the inside. A traditional solid shaft is often unable to remove enough heat from the inside of the core. Since the inside is the rotating side, cooling methods such as liquid cooling is not easily achievable. By machining a hollow shaft, air can be forced through and remove the heat. For small machines this is not needed and is difficult to achieve. For very large RTs a hollow shaft is a viable option.

Additionally, the casing can be made bigger than the lamination outer diameter to facilitate direct cooling on the laminations. With the radial lamination

orientation, the outermost part can be used as a finned heat sink with the laminations acting as the fins. This increases the surface area and will therefore result in a more efficient energy transfer to the surrounding areas. This will indirectly help the rotor as it allows for heat transfer through the air gap onto the stator.

The internal forced convection model is shown in Appendix C.

3.7.5. Combined heat transfer

To determine the temperatures inside the RT a combined heat transfer model is required. Since the core losses vary with the flux distribution inside the core, it is nearly impossible to get the temperature distribution accurately outside of FEA. In this instance we are considering the core and windings as lumped objects with a uniform temperature distribution. The thermal model is that of radial heat transfer. The model can be seen in Figure 3.17.

The primary objective of this thermal analysis is to determine the surface, core, and winding temperatures. The surface temperature can be obtained by assuming all of the heat flows outward to the surface. The temperature at the surface is stable when the rate of heat transfer away from the surface equals that of the losses inside the RT. The solution is to work backwards from the surface temperature to determine the core and winding temperatures. The method of calculating the final temperatures is shown in Figure 3.18.

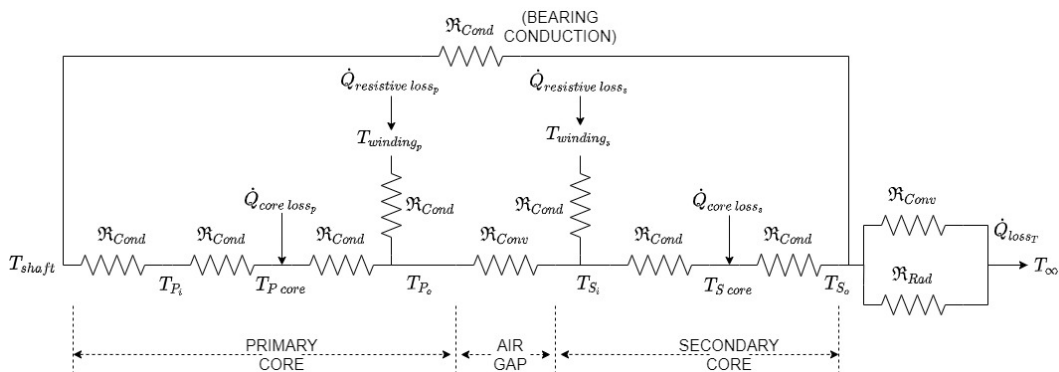


Figure 3.17: Thermal resistance model

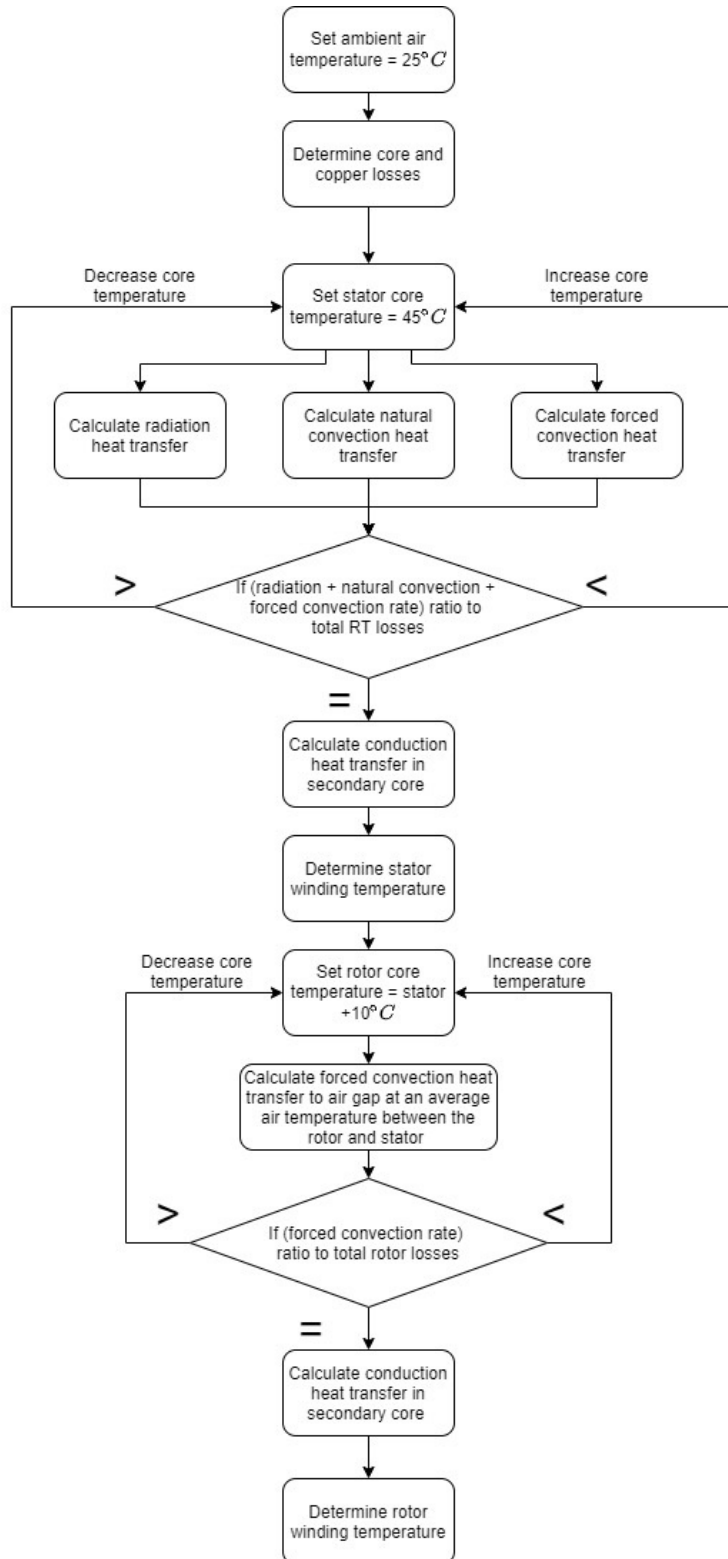


Figure 3.18: Thermal analysis method

3.8. Vibration

To evaluate the use of the RT in a direct shaft coupling an analysis has to be done on the vibration characteristics of the machine. Special care has to be taken that the air gap stays uniform throughout its operation. Rotating unbalance can also lead to issues with extra torque ripple on the DFIG.

3.8.1. Rotating unbalance

The rotor of the RT needs to be balanced in such a way that the weight is equally distributed in the radial direction. In practice this is usually not achieved due to gaps in the laminations that exist to facilitate the wiring of the rotor. This gap leads to not only the unbalancing of weight on the rotor but it has less force on it due to the flux path. This will cause the rotor to have a rotating force which the bearings will need to transfer to the stator. A proper mount is required to ensure the rigidity of the system.

The total force F_t that the bearings will need to withstand is the weight of the rotor F_n and the force caused by rotation

$$F_t = F_n + F_r \quad (3.55)$$

$$F_r = U\omega^2 \quad (3.56)$$

with ω being the rotational speed and U being the unbalance of the rotor. Since the unbalance is a static unbalance where there is mass removed from only one axis, the counter-weights only need to be added there. The unbalance can be determined from the sum of the mass balance

$$U = \sum M_1r_1 + M_2r_2 + M_n r_n \dots \quad (3.57)$$

where each mass is evaluated at its center of gravity to get the radius. The total added weight must make the unbalance U equal to zero. The mass should be added in such a way as not to unbalance the rotor in a different axis.

The effect of the unbalanced radially stacked rotor with a winding slot can be seen in Figure 3.19. The cyclical force experienced by the RT is much larger at higher rotational speed. The added vibrations will form induced resonance that can affect the operation of the RT and potentially unbalance the phases as well as cause additional wear and friction on the bearings.

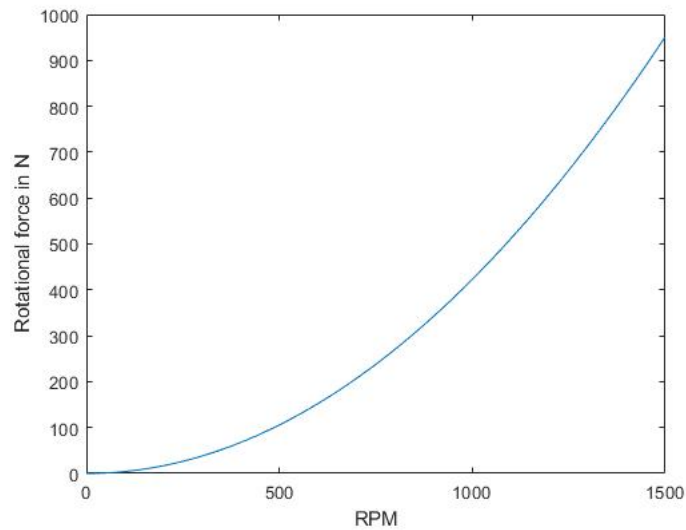


Figure 3.19: Rotating unbalance of a 0.5kg material loss on one side of the rotor of the RT vs speed

3.8.2. Natural and induced resonance

The rotor will experience resonance based on its geometry and excitation. The designer can use modal analysis to determine the natural frequencies that the rotor will vibrate at. The mode shape of the vibrations will be dependent on the stiffness and rigidity of the shaft. If the frequency of the natural harmonics coincide with that of the induced forces excessive vibrations will occur. This could lead to issues such as increased noise and wear on the bearings and in extreme cases it could affect the air gap distance and stability of the RT.

The induced vibrations will come from the flux excitation of the RT. The forces experienced is sinusoidal at the electrical frequency that the RT is operated at. Since the phases are 120° offset from each and not balanced such as on conventional electric machines, the total vibrations and the number of harmonics introduced into the system will be large.

3.8.3. Noise

Since perceivable noise is simply vibration in the audible frequency spectrum of the human ear, which is around 20-20000Hz, the vibrations of the RT could cause a very high ambient noise level. Since the operating frequency of the grid is at 50Hz, the vibrations caused by the time varying flux through the laminations, cause conventional transformers to be noisy. This is especially noticeable when the transformer is close to or at full load. Since most dis-

tribution transformers are oil cooled, the oil absorbs some of the sound and converts it into heat.

In the case of the RT, it suffers from additional imposed noise due to the mechanical vibration caused by rotation. If the vibration from the rotation superimposes on the vibration of the forces caused by the flux, the RT will be very noisy. For the radially stacked case, the laminations should be completely baked in resin to ensure that they cannot vibrate with respect to each other as this will increase the amount of energy dissipated as vibrations.

The vibrational noise that the RT emits is a form of loss and should be added to the expected losses that occur in during the operation of the RT. In most cases this amount is small enough to neglect in efficiency calculations.

3.8.4. Air gap harmonics

Any deflection and vibration in the rotor will affect the air gap distance. The magnitude of the distance change should be such that the operation of the RT is mostly unaffected. A stiffer shaft selection and a larger air gap will reduce the effects that vibrations have on the RT. Improper alignment between the rotor and stator can lead to an unbalanced three phases. Proper bearing selection and tight tolerances reduce the likelihood of an alignment issue.

If the electrical design is robust and not sensitive to coupling changes the effect of the vibration will be minimal. Larger number of turns will increase the total inductance of the RT and increase its resilience to small coupling changes. The leakage inductance is dependent on the air gap distance and minor air gap changes should be considered during the design process. The effect of increased air gap distance is shown in Figure 2.12b.

3.9. Mechanical stability

The prototype that is considered needs to be mechanically stable enough to work without affecting the electrical results and be safe enough to operate in a testing environment. Since the proposed RT is of a frameless construction it needs to be sturdy enough to handle the vibration. Since the RT is not inducing any torque, there is no need for analysis.

The critical speed of the machine can be calculated in several ways depending on the expected type of failure. The shaft will experience centrifugal forces due to rotation as well as from the flux in the air gap. When determining the maximum rotational speed, the entire rotor can be considered a lumped model shaft, the limiting speed becomes

$$\omega_c = \left(\frac{\pi}{l}\right)^2 \sqrt{\frac{EI}{A\gamma}} \quad (3.58)$$

with l being the length, g the constant for gravity, EI being the shafts flexural rigidity, A the cross section and γ being the specific weight of the material. This type of analysis is useful in determining the largest air gap diameter that can be achieved for a specific shaft size and rotational speed. Due to the primary windings being wound on the rotor directly, the limiting speed is more likely to come from the forces on the wire. Since any metal will expand when heated, the maximum stress concentration will be when the rotor is running at full speed while the DFIG is cold and not yet synchronized to the grid. The limiting factor is the break strength of the wire with additional safety factors defined by the design requirements of the RT. The limiting speed of the bearings is typically magnitudes higher than speeds that can be achieved by a DFIG and does not need to be considered.

The final mechanical stability to calculate is the force that the lamination holding tabs will experience. A single lamination that shears off a single tab could be potentially dangerous if it came loose. Since the proposed RT is of a frameless design the required safety factor should be in excess of 10 due to the possibility of injury. The lamination tabs for the constructed RT are shown in Figure 5.3.

3.10. Summary

In this chapter an analytical model is developed for a single-phase RT. The principle of duality is used to express the transformer model as an electric circuit. A traditional (gapped) transformer model is used as the starting point. The transformer winding resistances are calculated the same way as a conventional transformer and is a function of winding dimensions and resistivity of the material used.

A reluctance model is used to create the magnetic model of the transformer. The primary and secondary sections are split into geometric regions that can be evaluated individually. From the reluctance model the magnetizing inductance can be calculated. To keep the model as reliable as possible the leakage inductance is calculated using the energy stored in the windings and air gap. Non-ideal elements such as lamination stacking factor and its effects on the air gap is included.

The possible topologies for utilizing the single-phase designs in a three-phase system is discussed. The three-phase RT can either be made from three single

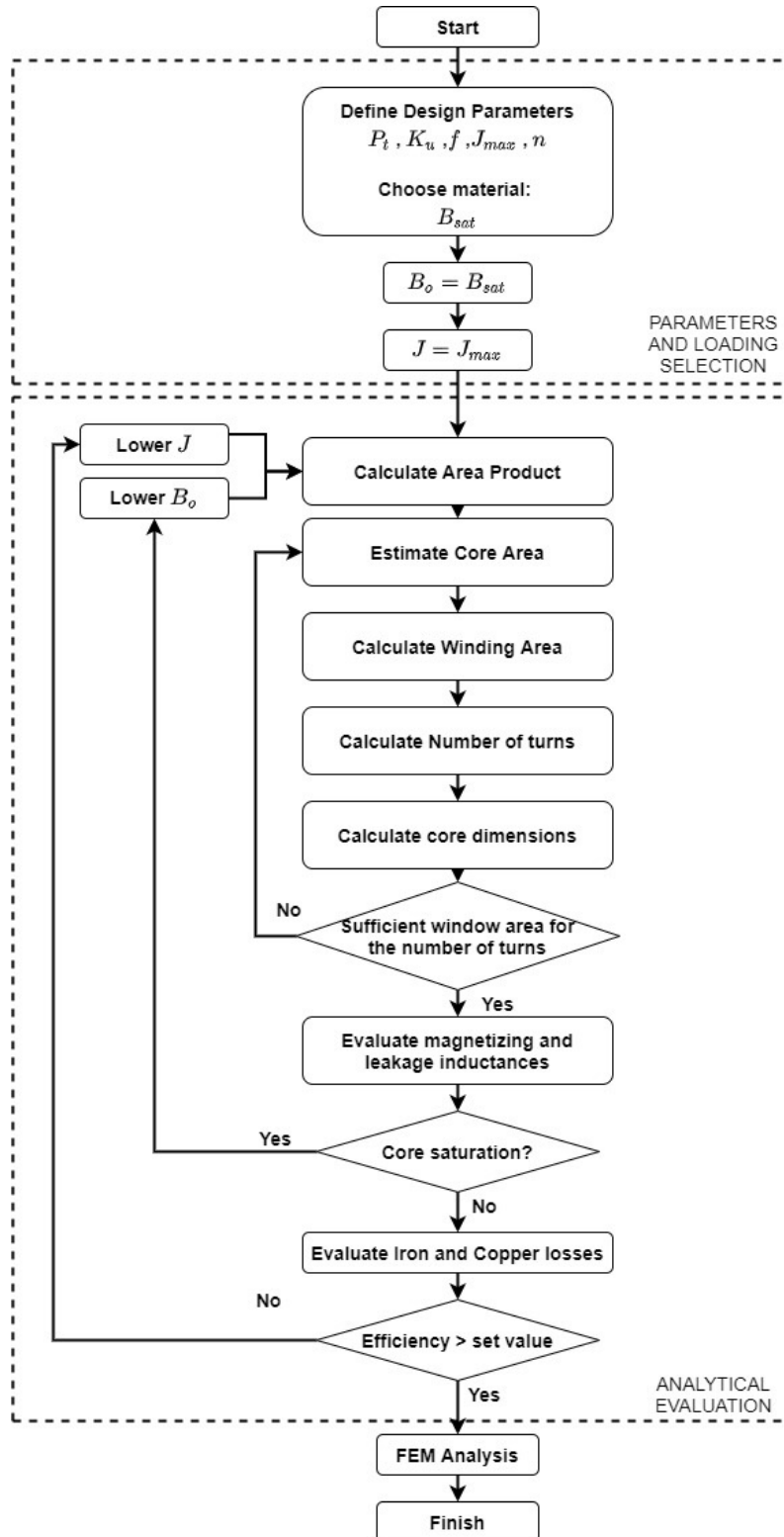


Figure 3.20: Flow chart illustrating the final RT design outline

phase RTs in either the axial or radial air gap configuration, or it can be made from a single core. The single core offers advantages such as higher power density and easier construction.

The next step in the design is to select the material. At low frequencies the core has to be laminated to reduce eddy currents. The winding material also plays a large role in the cost and efficiency of the RT. The RT is then evaluated physically in terms of thermal, vibration, and mechanical design. The analysis is required to achieve a functional RT that will meet its performance requirements.

The final iterative design outline is shown in Figure 3.20. The main focus of this design is to increase efficiency and magnetic coupling while reducing the overall size. The design outline procedure is the same regardless of the topology or lamination layout.

Chapter 4

Design and FEA analysis of a 6kVA three-phase RT

To design the three-phase RT, the RT model developed in Chapter 3 can be used as a starting point. The RT can first be designed as a single phase RT and then adapted to a three-phase RT with a single core to meet the requirements. In this chapter the design of a single phase RT is first investigated then integrated as a three-phase design. The final mechanical design of the RT is then done.

4.1. RT design outline and requirements

The first step in the RT design is creating a list of requirements and performance metrics that it has to adhere to. The purpose of the RT is to couple to the RDFIG and must be able to handle the full rated current and voltage of the RDFIGs rotor. The design requirements stem from the design of the RDFIG and the intended role.

Table 4.1: 6kVA three-phase RT design requirements

Parameter	Value	Unit
I_{rotor}	8.7	A
V_{rotor}	230	V
P_{rotor}	5760	W
Frequency	50	Hz
n	90	%
PF	0.96	
Impedance	9	%

CHAPTER 4. DESIGN AND FEA ANALYSIS OF A 6KVA THREE-PHASE RT

The design requirements are given in Table 4.1. The requirements are the minimum that the RT has to achieve. The requirements on size and length are not considered in this approach but should be minimized. The leakage and magnetizing inductance is of particular importance.

To ensure the validity of the analytical model, another form of verification is required. This is most easily done with a finite element analysis software such as Ansys Maxwell. In this section we discuss the different modeling techniques that can be used in designing and validating different lamination layouts. Analysis will be done on all of the proposed designs.

4.2. Single phase 2kVA RT design and analysis

In order to design the three-phase RT, a single phase design should first be done. This reduces the simulation time and complexity and allows for a more rapid design process. The analytical analysis of a single phase is also simpler, allowing for more than one design to be considered. The design can be optimized in ANSYS Maxwell or analytically in MATLAB.

4.2.1. Single phase design dimensions and parameters

The first step in the design is deciding the topology of the RT. From previous research [17, 18, 23, 43], the axial air gap topology with adjacent windings has proven to be the most suited design. The layout of the design is shown in Figure 4.1. The stator limb is chosen as the same size as the rotor limb and it is sized at the smallest point. This reduces the flux density radially outward as the material will increase.

Using the equations presented in Chapter 3 and appendix A, the dimensions of the RT can be calculated based on the chosen topology. The shaft is set at a diameter of 50mm for structural rigidity as well as to improve the inner to outer radius ratio. The air gap is set at 0.4mm. In this design the RT will have the dimensions as shown in Table 4.2 for the layout as shown in Figure 4.1.

4.2.2. Single phase 2D analysis

The simplest way of determining the validity of the analytical solution is a 2D analysis. The analysis is the most basic form of validation and is quick to achieve. It also offers a starting point for the design where it can be incrementally improved in each of the design iterations. The model aims to calculate

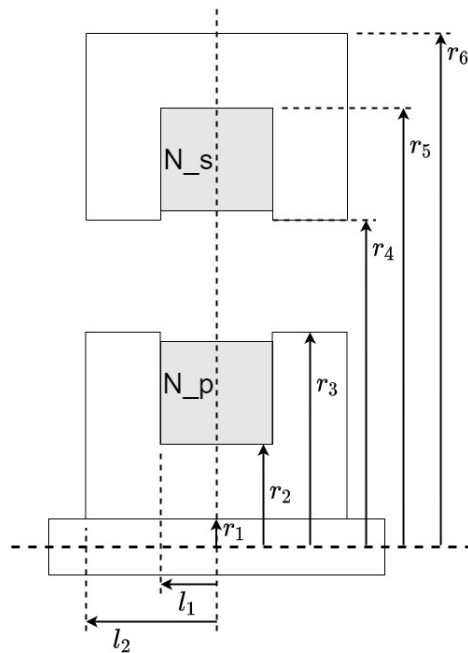


Figure 4.1: The layout of the single phase axial air gap RT with adjacent windings

Table 4.2: 2kVA single phase RT design dimensions as shown in Figure 4.1

Parameter	Value	Unit
r_1	25	mm
r_2	56	mm
r_3	71.2	mm
r_4	71.6	mm
r_5	96.85	mm
r_6	107.9	mm
l_1	31.5	mm
l_2	53.9	mm
N_p	178	turns
N_s	178	turns

the maximum flux density in the core, as well as the magnetizing and leakage inductance.

Since the model is in 2D, the solver can be set to an axis-symmetric model which is the easiest to compute. The axis-symmetrical model is a simple model that only consists of one half of the core in the 2D plane. Rotation in this mode is not useful due to the solver assuming solid parts. This type of core and winding configuration induces no additional torque on the shaft and rota-

CHAPTER 4. DESIGN AND FEA ANALYSIS OF A 6KVA THREE-PHASE **16**

tion analysis can be omitted. The 2D model can be optimized in Maxwell to achieve higher efficiencies or smaller size.

This type of simulation has some significant drawbacks when a final design is chosen. Due to its approximation of a solid cylinder for the rotor and stator, it does not have the same amount of material as a physically built model. This results in a lower flux density and can lead to the assumption that the RT will not saturate. This is particularly important if the RT is built with no form of compensation for the decreasing lamination fill factor as the radius increases. Adding filler laminations will decrease the difference in expected versus achieved performance. A much more conservative answer should be expected with flux densities proportionally lower. The relationship is based on the fill factor that can be achieved during manufacturing.

The solver can be partially improved by the adjustments of the material setting to laminated and lowering the fill factor. Using this will result in a core that has less material and will correlate better to the analytical model without a noticeable decrease in computational time. This does not solve the problem completely as the lamination stacking factor cannot be set as a function of radius.

The second drawback of 2D modeling of the RT is the lack of calculating other parameters that would be needed for a physical implementation such as eddy current analysis and accurate core losses. Some software packages can

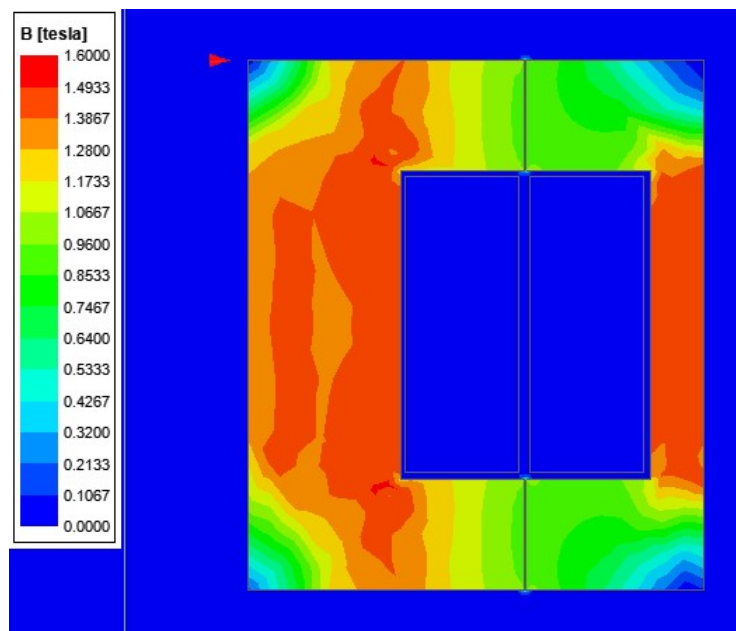


Figure 4.2: Flux distribution in the RT during an axis-symmetric 2D analysis

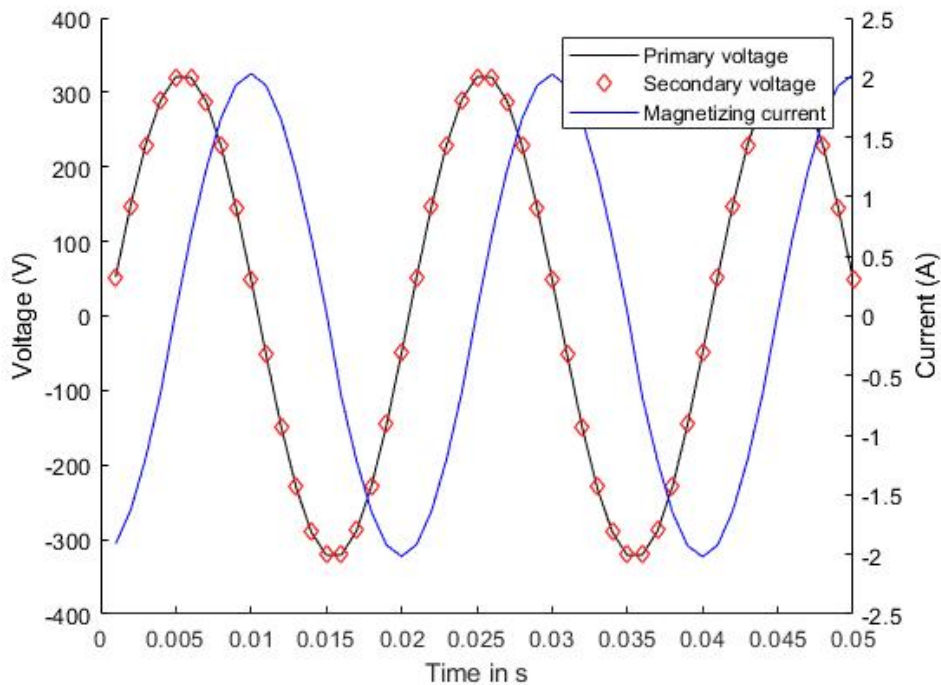


Figure 4.3: Voltage and current waveforms for the open circuit 2D model

still accurately model the winding resistances and therefore losses in the windings, but due to the lack of correct core losses, efficiency cannot be calculated. This makes the 2D models not useful for optimization as it would lose an important optimization parameter. The model would also pose limitations when a design is realized into a prototype as a thermal model would be difficult to achieve and design for.

The magnetizing and leakage inductance for the RT in a 2D simulation is often not correct due to the air gap being a constant length and rotation not affecting the operation in this mode. Analytical values could be used for electrical circuit analysis, but a 2D simulation would not be able to accurately verify the analytical answers. In the proposed RT FEA model shown in Figure 4.2 can clearly be seen that the RT is operating at around 1.5T which is the chosen point below the saturation point of M400-50A electrical steel which is at around 1.65T. This shows that the RT in a 2D simulation has a operating point in terms of flux density below the expected values. This could lead to the incorrect assumption that the core will not saturate once it is constructed. The open circuit waveforms are shown in Figure 4.3 and it shows a favorable magnetizing current. If a scaling factor is used the model can be used to calculate the knee point of the core.

4.2.3. 3D Analysis of the single phase radially laminated RT

There are two primary ways of constructing the radially stacked RT, namely with and without filler laminations. The filler laminations can be on either the rotor or stator or both. In this section only the effect of filler laminations on the rotor is considered due to its effect on the air gap.

4.2.3.1. 3D Model without filler laminations

The most basic design and assembly of a radial RT is one without any filler laminations on either the stator or the rotor. This is easier to manufacture and analyze as there is only one type of lamination on the rotor and stator side. The rotor has a very low fill factor at the air gap, leading to increased leakage inductance and a localized flux distribution in the stator side of the air gap. This results in inefficient use of the magnetic material on the stator. This type of construction will lead to a sub-optimal design in terms of overall size to power handling ability.

By the use of a quarter model, the simulation size can be decreased without a noticeable decrease in accuracy. The RT can now be evaluated for almost

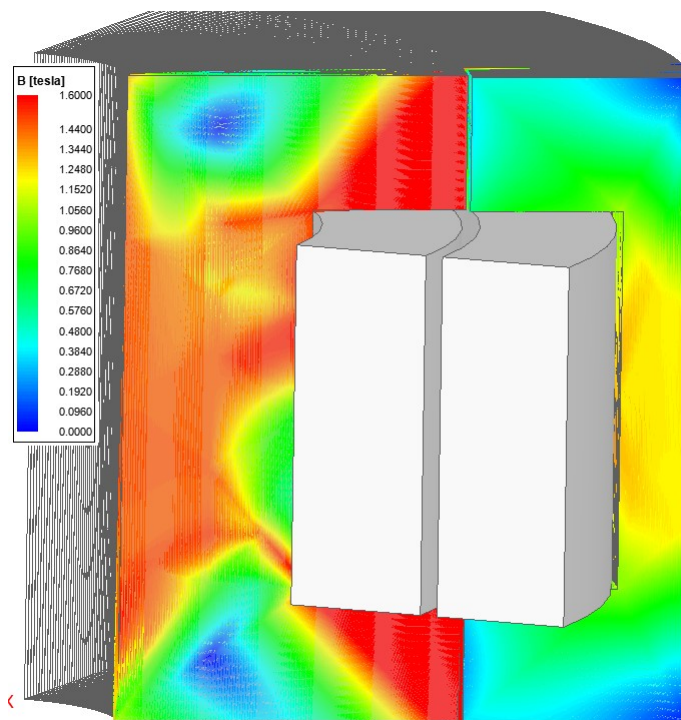


Figure 4.4: Flux distribution in the radially stacked RT without filler laminations during a 3D analysis

CHAPTER 4. DESIGN AND FEA ANALYSIS OF A 6KVA THREE-PHASE **19**

all of the shortcomings that the 2D simulation could not. Accurate core losses and inductance parameters can aid in the optimization process and validate the analytical results. The effect of rotation can also be investigated to ensure that the design would function correctly at rated conditions. Figure 4.4 shows the flux distribution in the radially stacked RT without filler laminations. The flux density is higher than with the 2D model due to there being less magnetic material present on the rotor side. The low fill factor on the rotor at the air gap can be partially reduced by choosing a larger shaft size, therefore having a smaller inner to outer radius ratio.

In this case the flux density is around 1.7T in the RT which is at the start of the saturation region and due to the nonlinear behavior of electrical steel in this area, the RT requires a larger magnetization current. The magnetizing inductance is smaller than that of the 2D and the leakage inductance higher. The core and hysteresis losses, as well as eddy currents show that this design is feasible to implement, but due to the low fill factor on the rotor at the air gap, the design is not ideal. The high leakage inductance and low magnetic coupling results in a poor performing transformer. To compensate for the weak magnetic coupling, the ratio between the core and winding area (Equation (3.3)) can be adjusted so that a more suitable design can be optimized for.

4.2.3.2. 3D Model with filler laminations

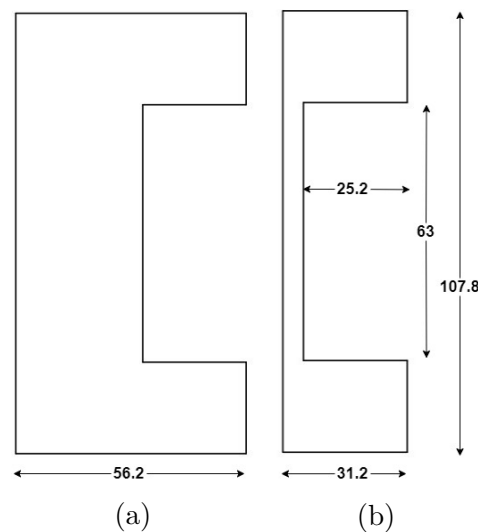


Figure 4.5: Lamination size difference for the rotor (a) and rotor filler (b) lamination

CHAPTER 4. DESIGN AND FEA ANALYSIS OF A 6KVA THREE-PHASE RT

To increase the amount of active material without increasing the overall dimensions of the RT, filler laminations can be placed on both the rotor and the stator. In this section we only look at placing laminations on the rotor side due to the effect that it has on the air gap. The stator can achieve a 0.95 fill factor at the air gap, therefore the addition of filler laminations on the stator will not have such a profound effect on the operation of the RT.

For ease of manufacturing, laminations are placed 1:1 on the rotor side, which means that there is an equal amount of full size and half height (filler) laminations. The sizing difference can be seen in Figure 4.5. Due to the very small axial flux area of the filler lamination, they need to be evaluated separately when doing analytical calculations.

The addition of more magnetic material will lead to a higher magnetic coupling and a lower flux concentration on the stator. This will increase the effectiveness of the stator laminations since there is a larger effective usable air gap that the flux can cross. The effect of this can be seen in the flux density plot of the RT as shown in Figure 4.6. The core has a lower flux density in the yoke of the rotor due to the increase in magnetic material there. The core is now close to the 1.5T design point that was set in the analytical calculations. The effect that the increased magnetic material at the air gap has is shown in Figure 4.7.

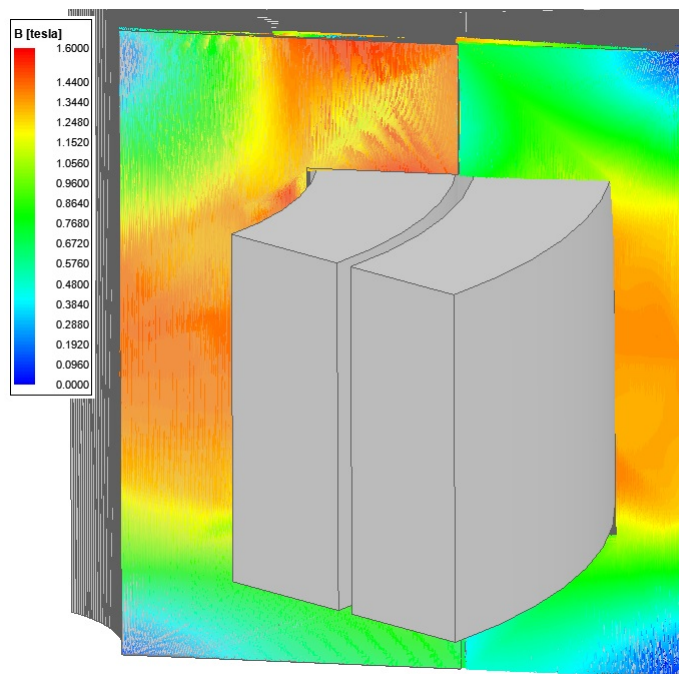


Figure 4.6: Flux distribution in the RT with filler laminations during a 3D analysis

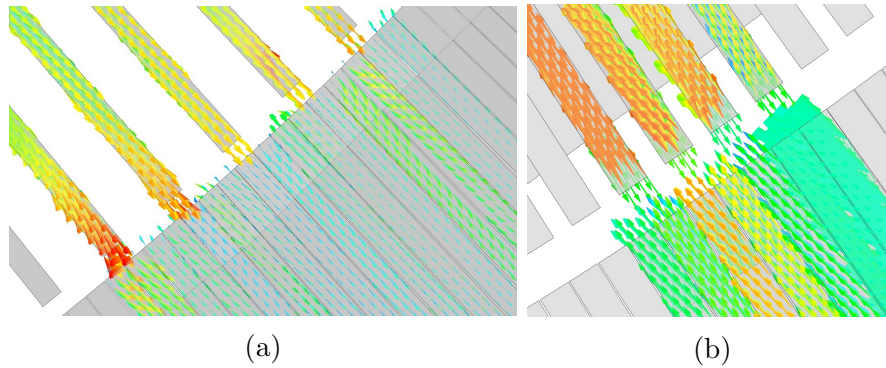


Figure 4.7: Flux in the air gap for RT (a) Without filler laminations and (b) With filler laminations

Similarly, the inductance parameters, eddy currents and core losses can be calculated accurately as with the simulation without filler laminations. The effect of the increased magnetizing inductance can be seen in the open circuit magnetizing current plot in Figure 4.10.

4.2.4. Rolled and stacked lamination layout

Stacking the laminations radially around the shaft is not the only method of constructing the RT. Using only flat sheets of laminations [22] constructed an RT using a combination of axial and radial sections. The design was not considered in this research due to the efficiency being lower than the proposed design target (85% achieved). An alternative to that is the combination of rolled and stacked laminations. This increases the fill factor of the machine to over 0.9. The design has increased power density when compared to the radially stacked design. The rolled and stacked design is shown in Figure 4.8.

The main drawback of the design is the manufacturing of the core. The rolled and stacked sections need to be joined using an adhesive that can transfer heat before they are machined. The edges cannot be of a stepped design as the equivalent air gap distance between the two sections would be too large. The surfaces also need to be machined at a low speed due to thermal constraints of the laminations, as they will alter their magnetic properties if they get too hot. This results in a much more expensive RT core to construct due to the special machining work. The windings of the RT core remain largely the same with the number of turns being the primary difference.

The flux density of the proposed core is shown in Figure 4.9. The dimensions and number of turns is kept the same as the radially stacked design to show how much the increased fill factor of the core combined with a smaller effective air gap distance affect the operation of the RT. The flux density is very low

CHAPTER 4. DESIGN AND FEA ANALYSIS OF A 6KVA THREE-PHASE **RT**

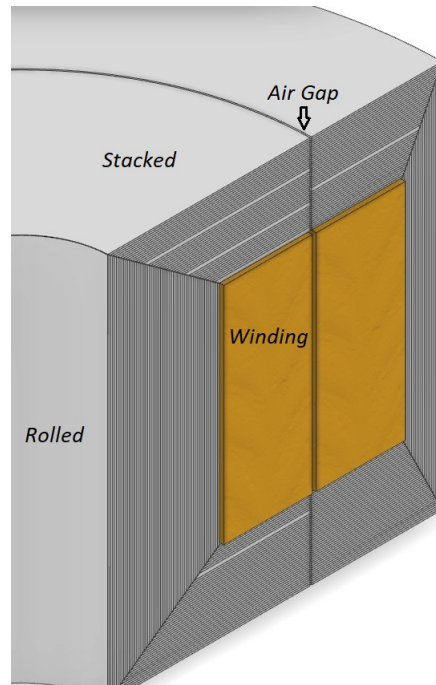


Figure 4.8: 3D representation of the rolled and stacked RT

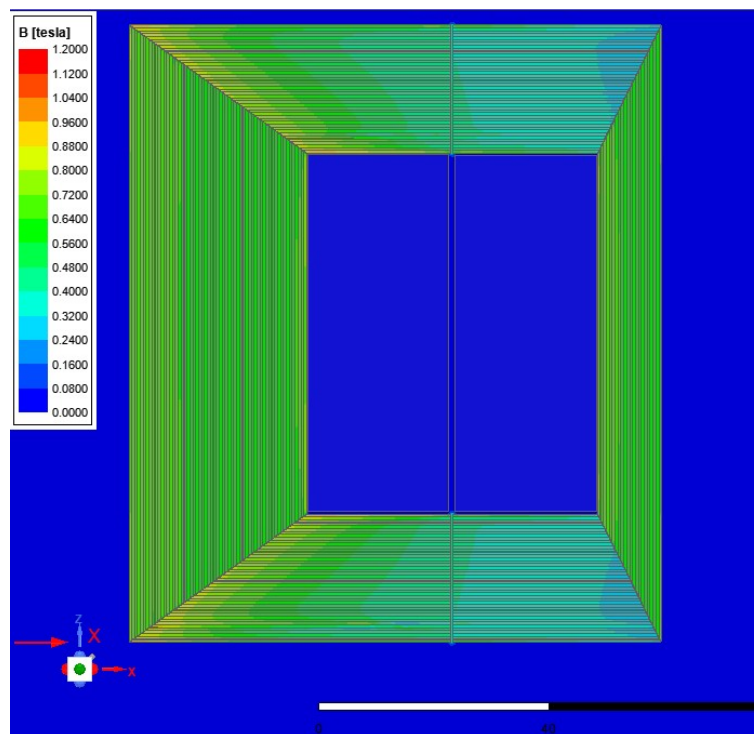


Figure 4.9: Flux density of the rolled and stacked design during an axis-symmetric analysis

at 1.0T and the core is not being used to its full capability. To mitigate the effects of eddy currents, each of the rolled and stacked layers has to have a slit in them. This stops the eddy currents from flowing in the same direction as the winding. This type of core construction has a limit on the scalability of the design as each layer of laminations increase the effective air gap that the field has to cross. It is therefore only suited to small cores.

4.2.5. Comparison of the different single phase FEA models

To make an accurate comparison between the 3 proposed models there are a few factors to consider. One of the primary differences of their operation is the amount of current required to magnetize the RT. This will affect the low power operation of the RT which is typically at low wind speeds. At a low power output the DFIG is also not very efficient especially when the load is a purely inductive load such as the magnetization of the RT. A higher magnetizing inductance which reduces the magnetizing current can be achieved at a lower air gap distance. The radially stacked RT with filler laminations does

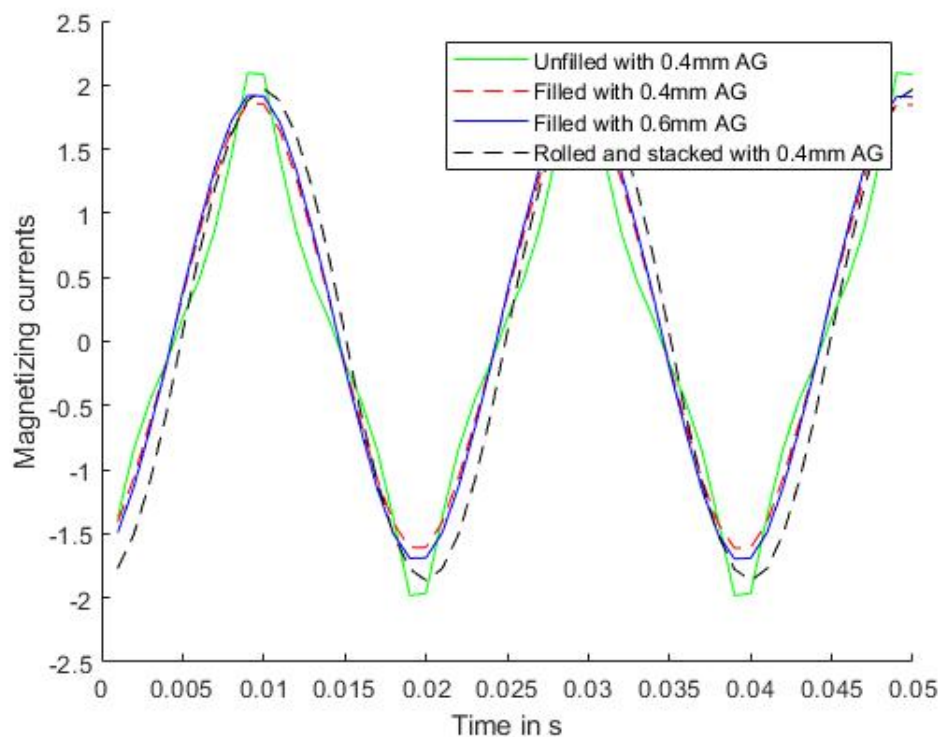


Figure 4.10: Magnetizing currents of the radial RT with and without filler laminations and the alternative configuration

Table 4.3: Inductances of the different proposed single phase RT

	L_{mp}	L_{lk}	Unit
Unfilled 0.4mm AG	430	3.8	mH
Filled 0.6mm AG	451	3.6	mH
Filled 0.4mm AG	560	3.5	mH
Rolled and stacked 0.4mm AG	627	4.9	mH

better in this regard but is still worse than the rolled and stacked design. The magnetizing currents are shown in Figure 4.10.

The second important aspect is the leakage inductance of the proposed designs. All of the proposed designs have worse leakage than an equivalent gap-less power transformer with only the rolled and stacked RT being worse than the other two proposed designs. With a higher current the voltage on the secondary side will drop as the RT has a high impedance percentage. This is the inherent limitation of a RT as it increases the induced voltage requirement of the DFIG. This can be mitigated if it is coupled with a DFIG that can provide the necessary voltage it requires. The increased voltage is directly proportional to the % impedance of the RT.

The third consideration when choosing between RT concepts is the manufacturing of the proposed design. The radially stacked RT is the easiest and most cost effective to construct, but it has the draw back of having an air gap distance that will likely not be uniform along the length of the RT. This requires the RT to be designed to accommodate a large range of air gap distances without altering the operational performance. At different air gap distances the RT will have a change in its magnetizing inductance, affecting its no-load characteristics. The rolled and stacked design does not suffer from the same air gap distance problems but introduces an air gap problem of its own. The rolled and stacked section needs to be joined together at 4 places along the flux path. This can lead to secondary air gaps if the interface boundary is not very precise. This can be a problem for large power rating RT's as the secondary air gap can have as big of an impact as the primary air gap. Expensive machining will be required to manufacture such a core due to the tight tolerances required.

The final characteristics that are important is the core and copper losses. Since the 3 designs use the same winding and have a comparable amount of core loss, the efficiency of the designs are comparable. Overall the radially stacked design with filler laminations are the most practical way of implementing the proposed RT. It has good magnetic coupling parameters and is suitable for designs at different power ratings.

4.3. Three-phase 6kVA RT design and analysis

The final validation of the FEA is to determine that the 3 single phase model can be used in a three-phase WYE configuration. This final validation aims to combine the 3 single phase RT's in a manner that only a single set of laminations include all three phases. Thermal analysis has to be done to ensure that the inner core does not overheat and operate at a reduced efficiency. The three phases should ideally have the same magnetizing and electrical characteristics to ensure a balanced load on the DFIG.

There are two main ways of arranging the three phases onto one sheet of laminated steel, namely shared limb and separated cores. In the shared limb configuration the two inner flux paths are shared between two phases. This results in a higher power density and reduced magnetic material.

Both models are evaluated in the same manner under the same loading conditions. The circuit used in ANSYS Maxwell is shown in Figure 4.11. Both layouts have the same number of turns, resistance and air gap parameters.

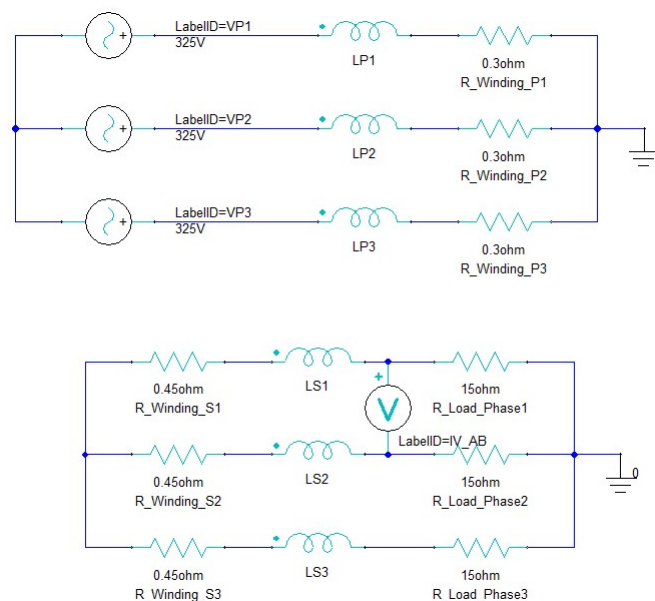


Figure 4.11: External circuit parameters for ANSYS Maxwell

4.3.1. Shared inner limb three-phase RT

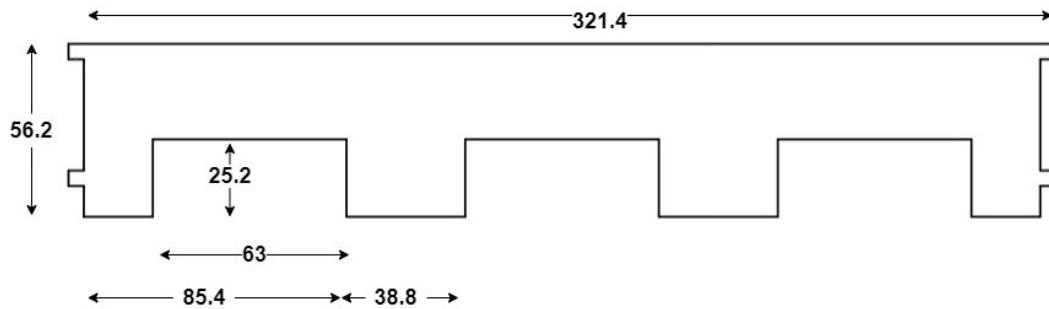


Figure 4.12: Primary lamination size for the shared limb configuration

The combination of all three phases on a single sheet allows for decreased costs and increased ease of manufacturing. There will be small cross flux between the adjacent phases due to this sort of configuration and can be seen in the FEA model in Figure 4.13. To get an increased power density, shared limbs can be used similar to conventional three-phase power transformers. In this design the cooling proved to be inadequate to facilitate such a design. The larger surface area and reduced flux concentration helps to keep the temperature down and prevent the middle phase on the rotor from overheating. The stator does not experience the same limitations as the rotor due to it being easier to cool. During the simulation an external circuit was used to test the individual performances of the phases, as well as evaluating potential fault conditions. The core dimensions for the shared limb core is shown in Figure 4.12.

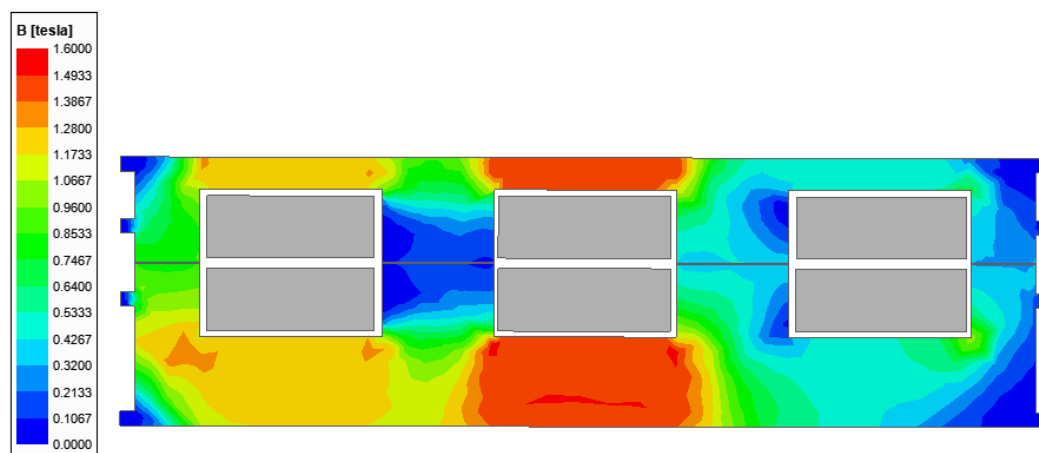


Figure 4.13: Flux density plot of the shared limb radially stacked three-phase RT with filler laminations

4.3.2. Separated limb three-phase RT

For the separated core each of the phases are separate from each other and can operate independently. The increased spacing allows for better cooling potential and reduces the unbalance if the air gap distance is not kept constant. The core dimensions for the separated core configuration is shown in Figure 4.14.

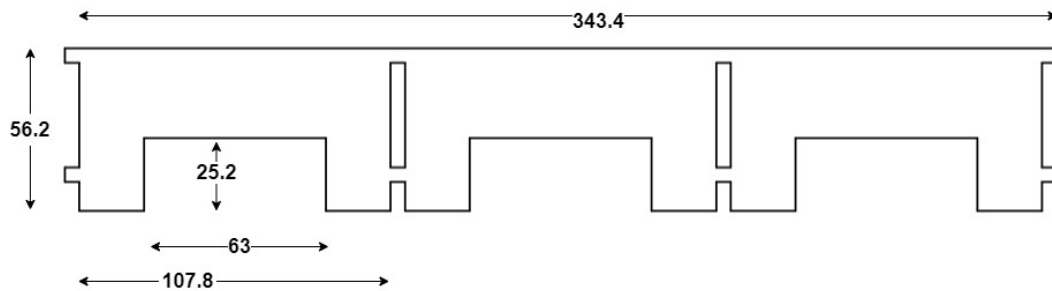


Figure 4.14: Primary lamination size for the separated limb configuration

The flux density of the three-phase Wye connected RT is shown in Figure 4.15 when phase A is at its peak flux density. The small coupling sections between the phases has the highest flux concentration. Their size was chosen to limit the flux cross over between the individual phases while maintaining structural rigidity. Testing was also done with only a single phase active to test the amount of flux that can cross and use the other limbs. The core is wound so that the middle phase has its winding direction reversed. This ensures that any flux that crosses will flow in the same direction.

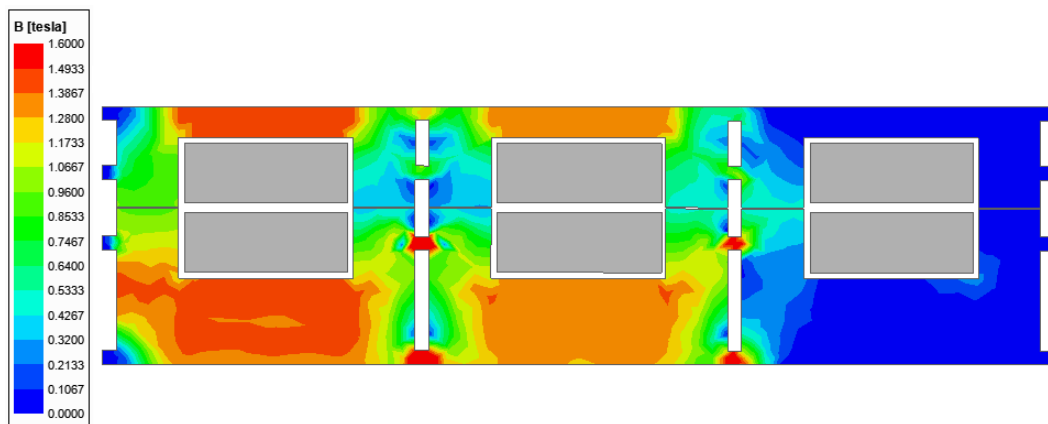


Figure 4.15: Flux density plot of the separated limb radially stacked three-phase RT with filler laminations

The middle phase therefore has around a 50% lower magnetization current compared to the other phases. At full load this reduces to less than 2%. The resulting magnetizing currents can be seen in Figure 4.16.

4.3.3. Comparison and model selection of the three-phase RT

The comparison between the two proposed layouts have to be done in terms of electrical performance, power density and manufacturability. The shared limb design has reduced magnetic material which leads to lower core losses and increased power density. These are both favorable and is the reason that power transformers are usually manufactured in this way. The two main problems that the shared limb design has is that it is difficult to cool on the rotor and is sensitive to coupling changes. With a prototype design the air gap consistency cannot be guaranteed, and therefore this topology is only suitable when access to accurate manufacturing and assembly is possible.

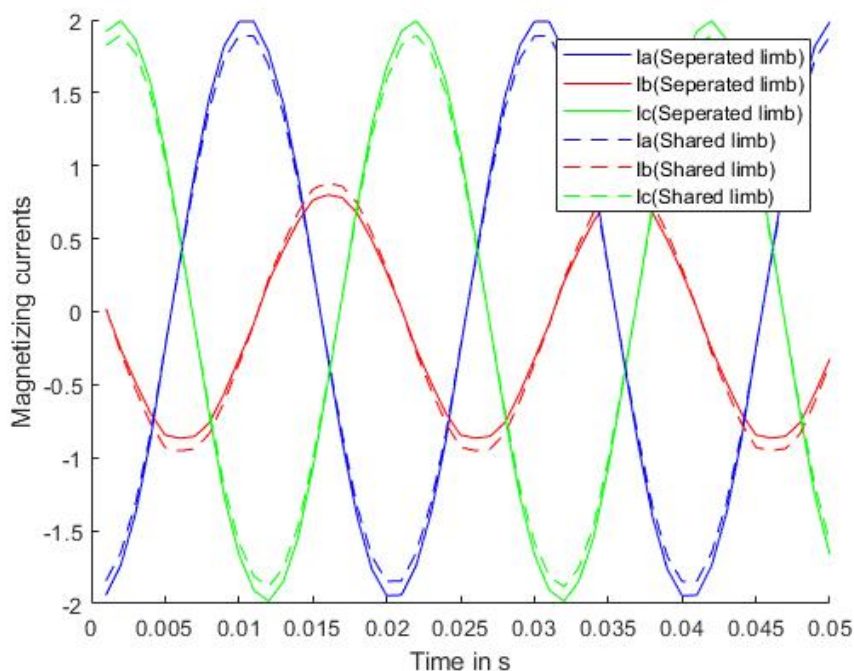


Figure 4.16: Magnetizing currents for the three-phase RT with and without the shared inner limb

The separated limb design shares many of the same characteristics with the shared limb although to a lesser extent. It is the compromise between using

CHAPTER 4. DESIGN AND FEA ANALYSIS OF A 6KVA THREE-PHASE RT

three individual phases in a three-phase configuration and sharing the inner limbs. The advantages that it has is simpler manufacturing due to a decrease in the lamination count and much lower sensitivity to coupling changes.

The design chosen is the separated limb, radially stacked, axial air gap RT. The overall length of the RT's laminations increases by 7% while the outer diameter stays constant. The primary side has filler laminations while the rotor does not. The lamination sizes for the primary filler lamination and secondary lamination is shown in Figure 4.17.

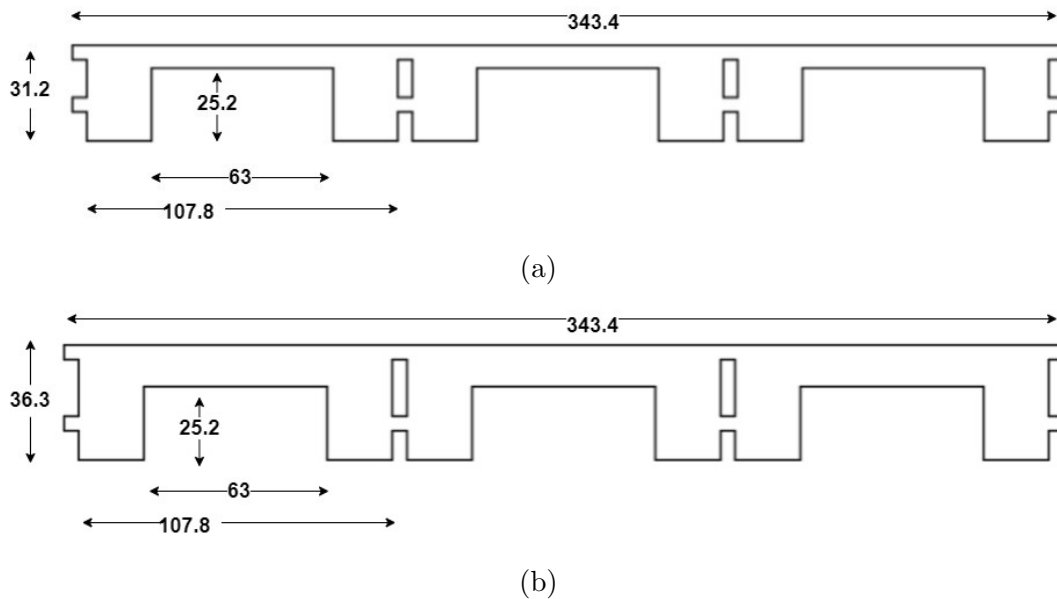


Figure 4.17: The (a) Primary filler and (b) Secondary laminations for the separated limb, radially stacked, axial air gap three-phase RT

The maximum load voltage and current waveforms for the radially stacked three-phase RT without shared limbs is shown in Figure 4.18. This current magnitude can only be reached when the RT is actively cooled. The rated current for the ambient cooled case is 9A. As expected the input current on the primary side is lower for the middle phase. Similarly the full load voltage and current waveforms for the radially stacked three-phase RT with shared limbs is shown in Figure 4.19.

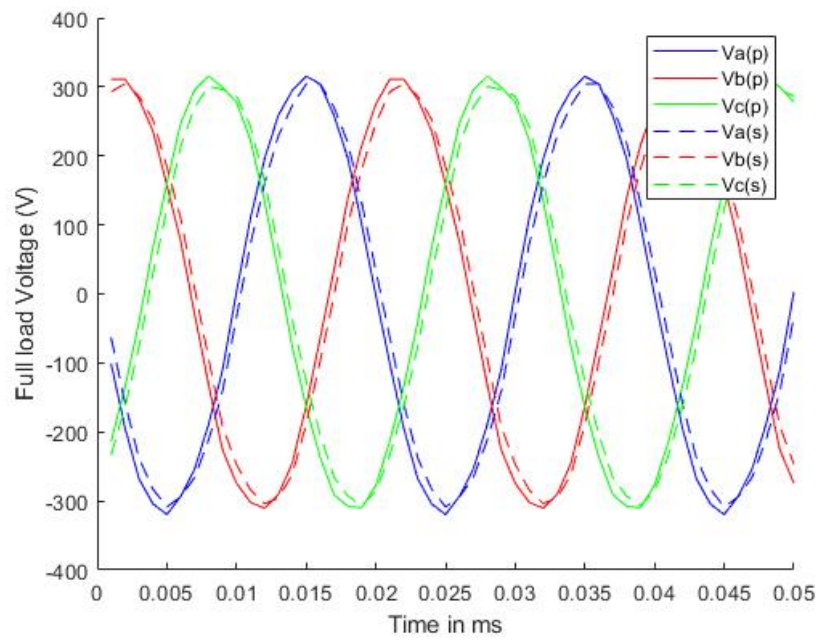


Figure 4.18: Primary and secondary voltage of the three-phase separate limb RT at maximum load with additional cooling

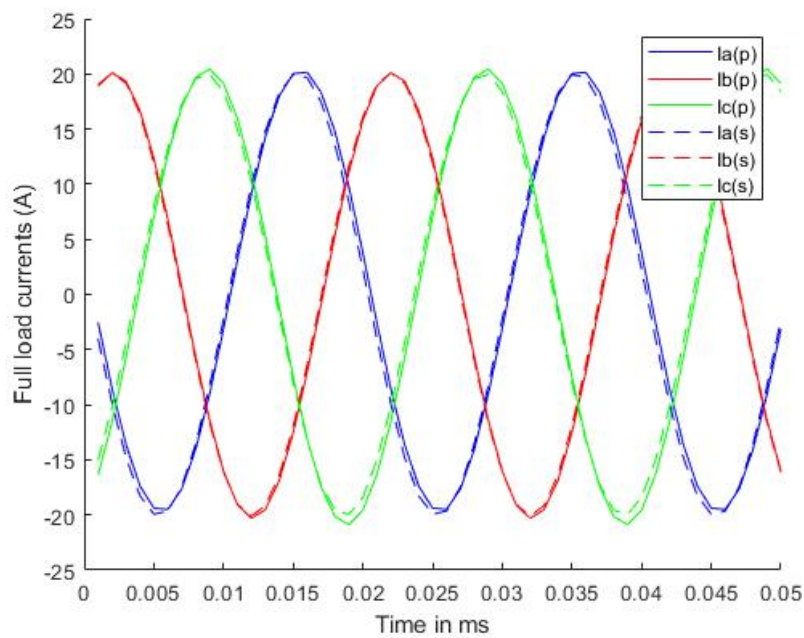


Figure 4.19: Primary and secondary current of the three-phase separate limb RT at maximum load with additional cooling

4.4. Three-phase RT mechanical design

The proposed RT design needs to be prototyped if a comparison between the analytical, FEA and a physical model want to be made. In this section the design is discussed in terms of mechanical layout and material selection. The sectioned view of the proposed three-phase RT is shown in Figure 4.20.

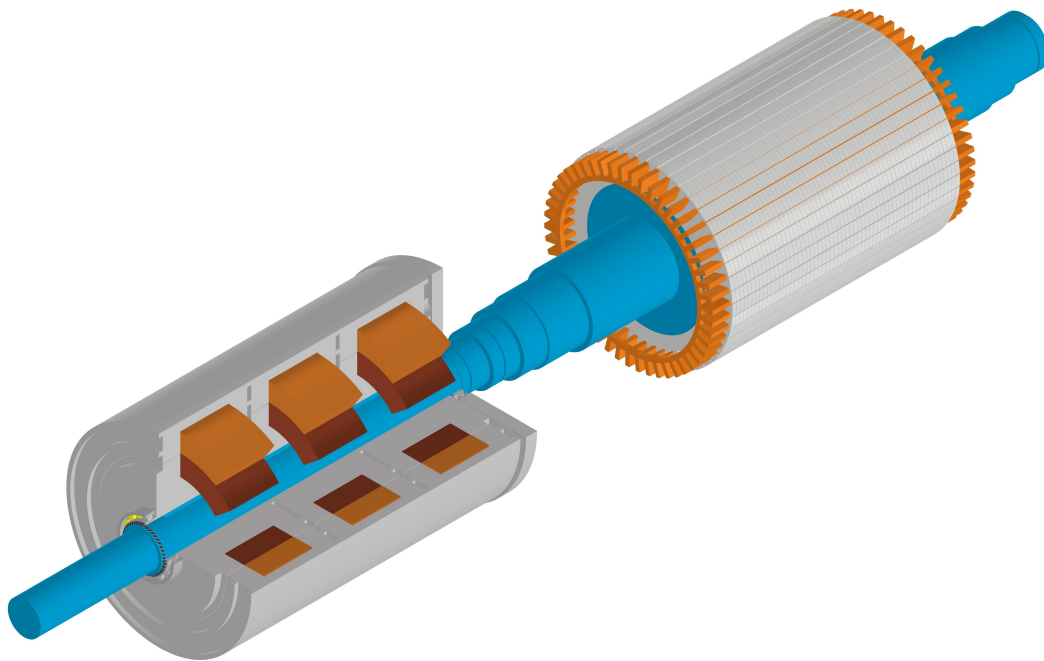


Figure 4.20: Three-phase RT connected to the DFIG shaft

4.4.1. Material selection

The material selection of the constructed RT is of significant importance as it can play a role in the electrical performance. Winding material and lamination selection play the largest role, but other ferromagnetic materials that interact with the laminations can have an effect too. Insulation material is of significant importance as the position and thickness of it can affect characteristics such as leakage in the secondary winding.

The lamination selection is done in the analytical design stage before the sizing is done. The characteristics and thickness of the material will change the magnetic coupling parameters of the RT and is a vital step. The chosen lamination is the M400-50A at 0.5mm. It is a non grain oriented electrical steel that is easily available. A thinner size such as 0.3mm will reduce the

CHAPTER 4. DESIGN AND FEA ANALYSIS OF A 6KVA THREE-PHASE 82

core losses but increase the complexity and cost of manufacturing. The lamination is insulated to prevent eddy currents to flow from one sheet to the next.

The winding selection is also done before the analytical calculations based on the design requirements such as size, power density and cost. The winding size is important as this is used to set the current density requirements of the calculations for the area product in Equations (3.1) to (3.6). The chosen material is the Armoured Polyesterimide (API) 200°C Enamelled Copper Conductor. It can operate at high temperatures and due to the thin insulation the winding fill factor can be high. The winding can be made out of multi-stranded API wire.

The shaft and the other plates that directly touch the laminations should have a low permeability to ensure that they do not become a part of the flux path. Carbon steel has a relative permeability of around 100 times that of air, so in certain topologies cannot be used directly against the laminations. The more appropriate material to use is stainless steel as it has the same relative permeability as air. Making the shaft out of stainless steel has the added benefit of being very stiff and having a high tensile strength. The chosen materials for each component is shown on the drawing for each part as seen in Appendix C.

The insulation material used on the rotor is more simple than on the stator. The rotor has its windings bare on the air gap side so it only needs to be insulated against the laminations. A 0.3mm sheet of NOMEX type 410 paper was used due to its excellent electrical resistance and mechanical strength. It is cut into the required shapes to protect the windings. The stator coils are wrapped in cloth and then ELMOTHERM varnish is applied to them in order to harden the insulation. The windings is double wrapped to ensure that the coils are protected during the assembly process of the stator.

4.4.2. Layout and assembly of the RT

Due to the windings of the RDFIG being on the rotor, the winding of the RT has to be on the rotor as well. The conductors pass underneath the bearing in a machined slot to allow for a connection to be made between the two machines. The rotor will be internally WYE connected with no neutral due to the RDFIG also not having a neutral.

Due to the dimensions of the RT a standard induction machine casing cannot be used due to the RT's length to diameter ratio. The RT will be of a frameless design with the bare laminations showing on the outside. This does require a stiff construction of the frame but allows for direct cooling on the

laminations. Since the RT is frameless it will be flange mounted for simplicity. A cut through concept of the layout as mounted is shown in Figure 4.21.

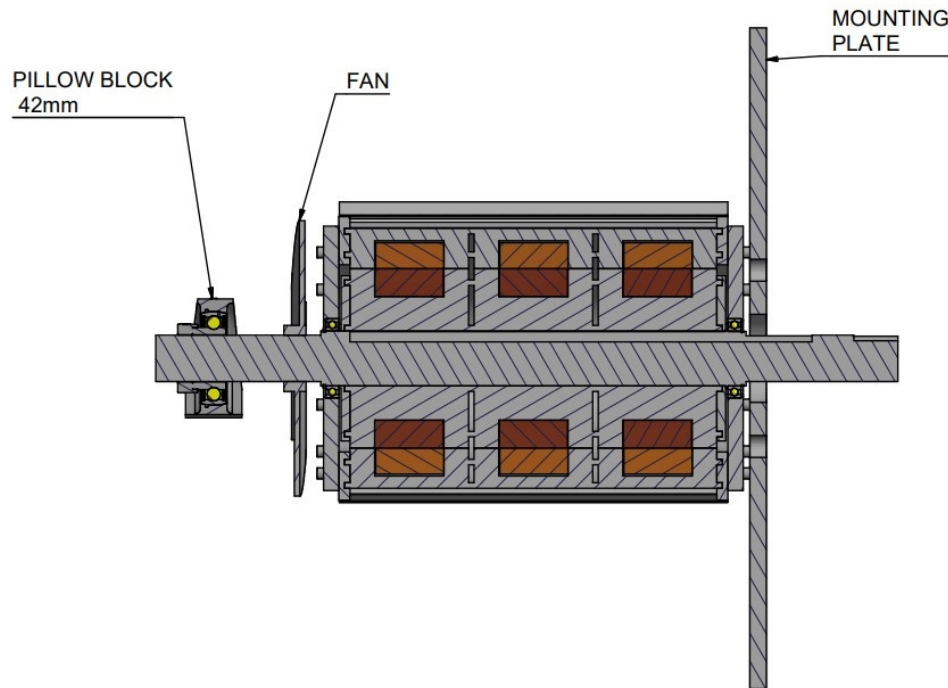


Figure 4.21: Three-phase RT physical layout as mounted

The RT has a space on the shaft for an external fan to be mounted to increase its thermal performance. It is supported in the back by a self-aligning bearing. The RDFIG is connected to the mounting plate side of the RT.

4.5. Summary

In this section the proposed RT was first designed and simulated in a single phase configuration to determine the accuracy of the FEA simulations. The 2D model proved to be too inaccurate due to the unique geometry of the radially stacked RT core. This required the use of a 3D model to accurately determine the core losses, magnetizing and operating parameters. The radially stacked design is also compared against an alternative rolled and stacked lamination design. This type of design is superior in terms of operating parameters but it is very complicated to manufacture. The proposed solution was to go with a three-phase radially stacked core.

CHAPTER 4. DESIGN AND FEA ANALYSIS OF A 6KVA THREE-PHASE **84**

The radially stacked core was analyzed in two configurations namely: Shared limb and separated limb. The shared limb is the conventional layout of transformers as it has the highest power density. The flux from two phases is shared in the same path. This type of configuration is very sensitive to coupling changes and any manufacturing defect would result in an unbalanced RT. The proposed solution is therefore to go with the separated limb design as it offers superior coupling parameters and thermal performance.

The proposed RT is then evaluated in terms of material selection and mechanical layout. The RT uses M400-50A laminations and API copper wire. Due to the unique layout and dimensions of the RT a standard induction motor frame cannot be used. The design is therefore a frame-less design that is flange mounted to a mounting plate. The RT is connected on its shaft to the RDFIG.

Chapter 5

Prototype manufacturing

The RT concept presented poses a more complicated mechanical design than that of a typical transformer. Due to the topology and size of the RT, a standard motor frame cannot be used, and a new casing or frame has to be designed. The following section details the subsequent manufacturing of the mechanical design process of the three-phase RT.

The configuration that was chosen has an inner rotor assembled on a shaft similar to a conventional DFIG. This is to connect the power on the rotor to the rotor output of the DFIG. The outer part of the RT remains stationary and is used for mounting the RT. The stator is shown in Figure 5.1a and the rotor in Figure 5.1b. The rotor is supported on its shaft by two bearings, one on either side of the core. The full assembly is shown in Figure 5.2.

The size and length of the shaft is determined by the electrical design and

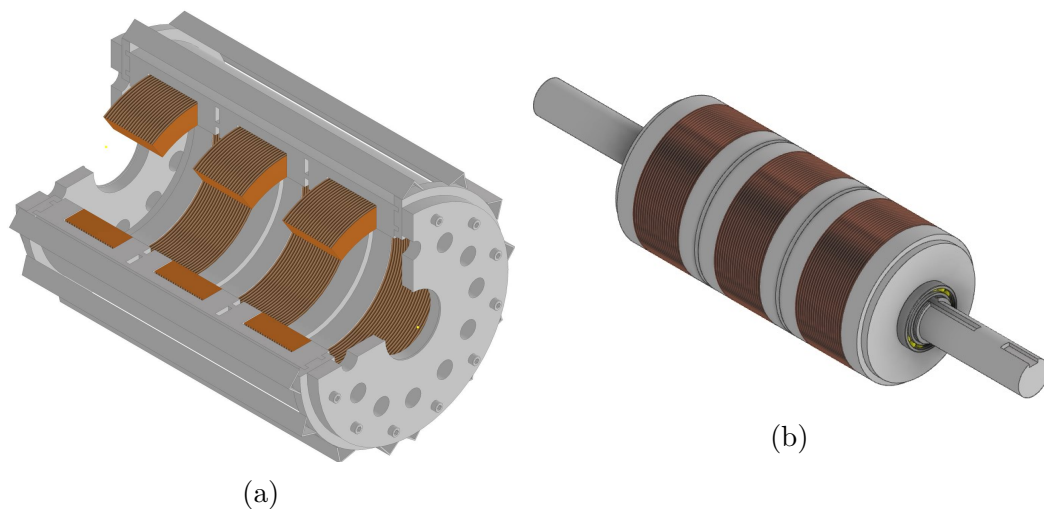


Figure 5.1: (a) The stator assembly and (b) the rotor assembly

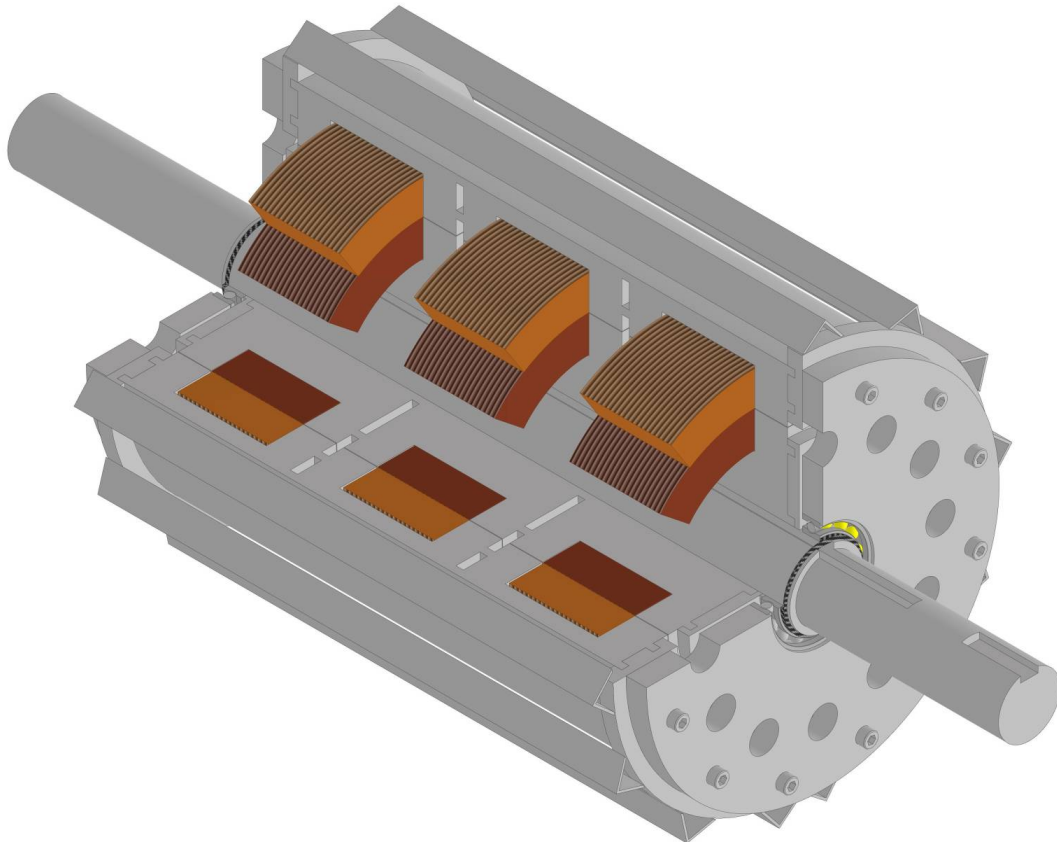


Figure 5.2: Cross-sectional view of the complete three-phase RT assembly

elongated to allow for the use of a fan. The RT is constructed as a frameless design with a welded design holding the lamination end plates. The bare laminations are showing and are only supported on the side. The mechanical drawing for each component is detailed in Appendix E.

5.1. Primary (rotor) portion of the RT

The rotor of the three-phase RT is constructed with the use of flat pieces of non grain-oriented electrical steel that is placed radially around the shaft. The laminations have notches that are securely held in place by the end rings. The primary lamination sheets consist of all three phases on a single sheet connected by small areas. The rationale was to decrease the cost of using three sets of laminations, extra machined parts to secure them and to increase the ease of assembly. The laminations can be seen in Figure 5.3, and the filler to primary lamination ratio in Figure 5.4.

Due to the stacking factor decreasing radially from the shaft, special care

is required to achieve a high fill factor at the air gap. This facilitates better magnetic coupling and a more suitable design. A low fill factor at one side of the air gap leads to inefficient use of the magnetic material on the opposite side. The higher fill factor is achieved by the use of filler laminations. The filler laminations have the same overall dimensions as the primary laminations, but with half the height. This allows for a stacking of 1:1 filler to primary laminations. The sizing and placement of the laminations are shown in Figure 5.5a. Additional filler laminations are possible but increases the complexity of the assembly.

The shaft is constructed of stainless steel. This allows for a high structural rigidity even with the longer shaft length. Stainless steel is a non-magnetic material, thus there is no impact on the operation of the core. The long groove in the shaft facilitates the wires coming from the winding and passing underneath the bearing. This is to facilitate electrical coupling between the RT and induction machine.

The holding plate of the lamination is made from stainless steel as well, due to its magnetic and structural properties. The end plate is secured onto the shaft and rests on a machined shoulder to ensure immobility. The shaft and lamination holding plate are mounted upright and laminations are placed in an upright position. Due to the square tabs securing the lamination, its supports an upright stacking procedure. To leave space for the windings to pass through to the groove in the shaft, special care is required. Another end-plate is used to secure the other end that includes a shoulder for the bearing. The assembly before and after the end plate is seen in Figures 5.5a and 5.5b. Bearings are then press-fitted onto both sides of the core and secured with circlips.

Once the laminations are all secured, the end plates on the rotor can be wound. The primary windings are relatively simple with only a single-strand enameled wire. Before the windings can be wound the core is insulated with NOMEX paper preventing the wires from damage and providing an additional

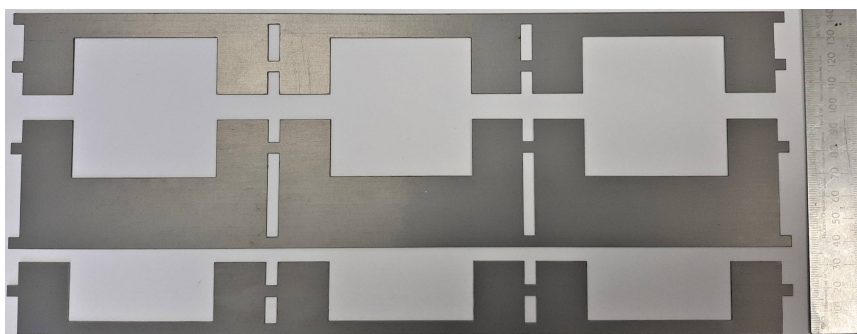


Figure 5.3: Laminations (a) Stator, (b) Rotor primary, (c) Rotor filler



Figure 5.4: Rotor filler lamination on primary lamination

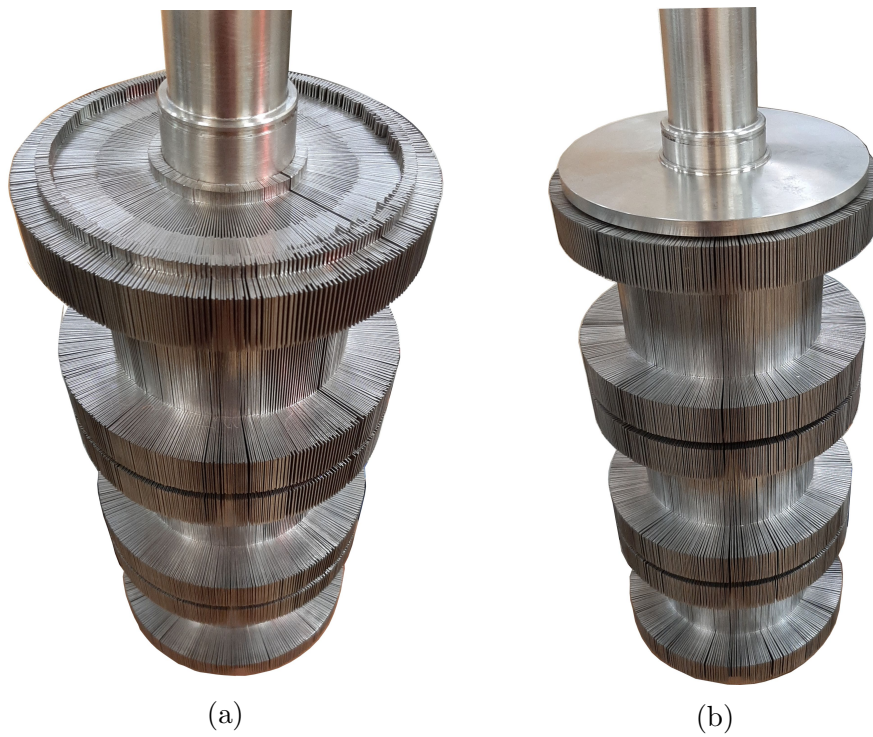


Figure 5.5: (a) Rotor laminations without end plate, (b) Rotor laminations with end plate

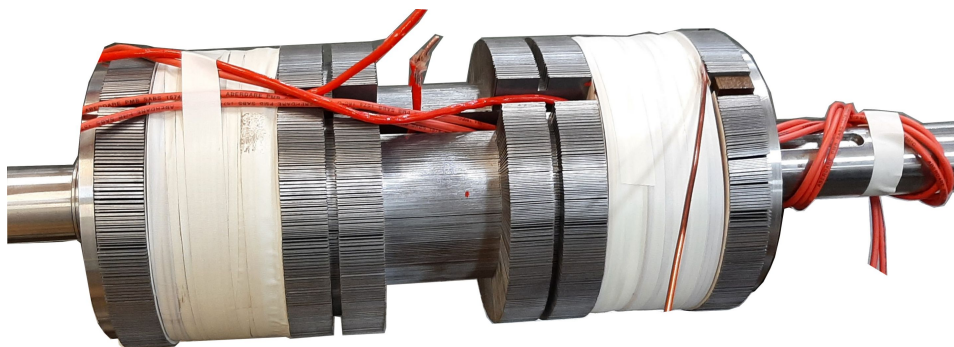


Figure 5.6: Rotor during winding

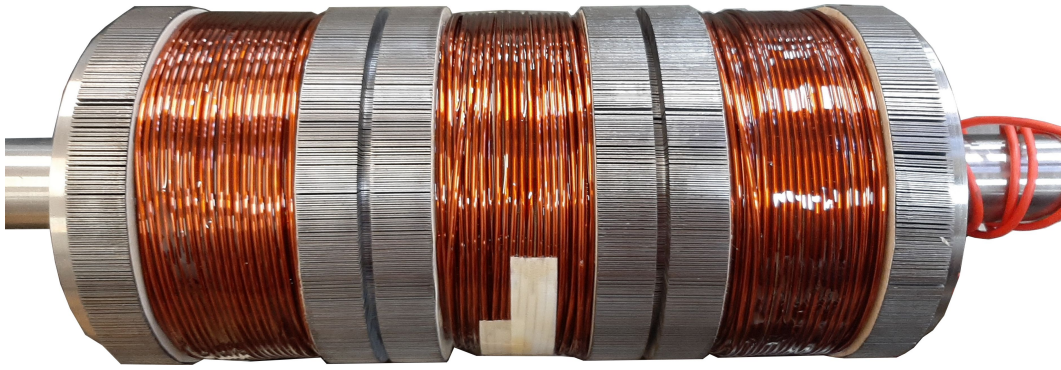


Figure 5.7: Completed rotor

layer of electrical insulation. Whilst the shaft is mounted on a lathe for easier access and to facilitate rotation, the wire is wound directly onto the shaft. The lathe was not used to turn the core due to safety concerns. The rotor can be seen during the winding process in Figure 5.6 and completed in Figure 5.6. As the wire is internally WYE connected, only three wires are available on the outside of the shaft. The wires run out on the shaft in the machined groove and pass underneath the bearings. The induction machine rotor is also connected in WYE. To secure the windings, they are varnished with Elmotherm. The height of the winding is very close to the air gap to reduce leakage and is therefore not covered in tape. The resultant fill factor is 0.62 which exceeded the designed specifications. Therefore, the rotor should be able to handle more than the rated current.

5.2. Secondary (stator) portion of the RT

The secondary (stator) side of the RT is more complex to construct as it is internally wound. This requires splitting the stator in two halves, to enable fitting the three windings on the inside. The coils are wound on a former of the correct size. For added protection from scratching and to act as an insulation layer, the coils are wrapped in two layers of cloth. Thereafter, the coils are varnished and baked to retain their shape. Due to only external support of the coils, a certain degree of stiffness is required to prevent deformation during assembly or operation. To achieve a higher fill factor, the coils were wound with two parallel wires. The bare coils before the cloth wrapping are shown in Figure 5.9c. The achieved fill factor of 0.56 was higher than the designed specification.

The core is constructed by using the same method that is used to stack the rotor. The two sets of end-plates that secure the laminations are welded

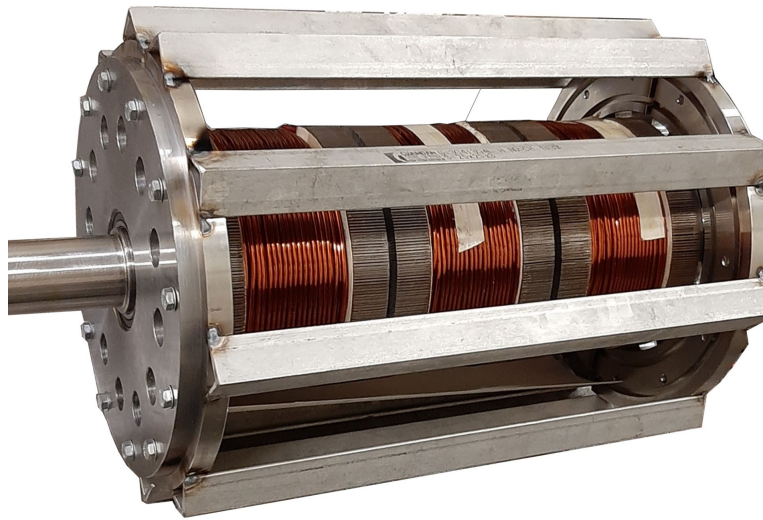


Figure 5.8: Stator without laminations test fitted onto rotor

together using stainless steel angle iron. The end plates can be seen in Figure 5.10a and the completed welding is shown in Figure 5.8. For a more rigid construction, a half section of seamless pipe could be used. The laminations can then slide in from the side. Thereafter, they are secured by welding the tabs of each end of the lamination in place. The half section is shown in Figure 5.9b. Although the laminations are the same length and have the same winding window as the primary laminations, they are not the same height, to ensure that the effective magnetic area of the rotor and stator is similar.

Additional filler laminations are not added due to the low impact on the operation of the RT. The fill factor of the stator is at its highest at the air gap interface. The stator is then assembled by placing the three coils in one half of the assembly and joining the two halves together. To secure the end plate, it is consequently bolted onto one side of the assembly. The half assembly with the windings can be seen in Figure 5.9d.

Due to the addition of cloth and using a former to wind the coils, the fill factor that can be achieved is lower than that of the rotor. The outcome is the same number of turns but with two wires in parallel as appose to a single heavier gauge wire as on the rotor. This should only affect copper losses and will not pose a thermal issue because cooling the stator is easier than the rotor.

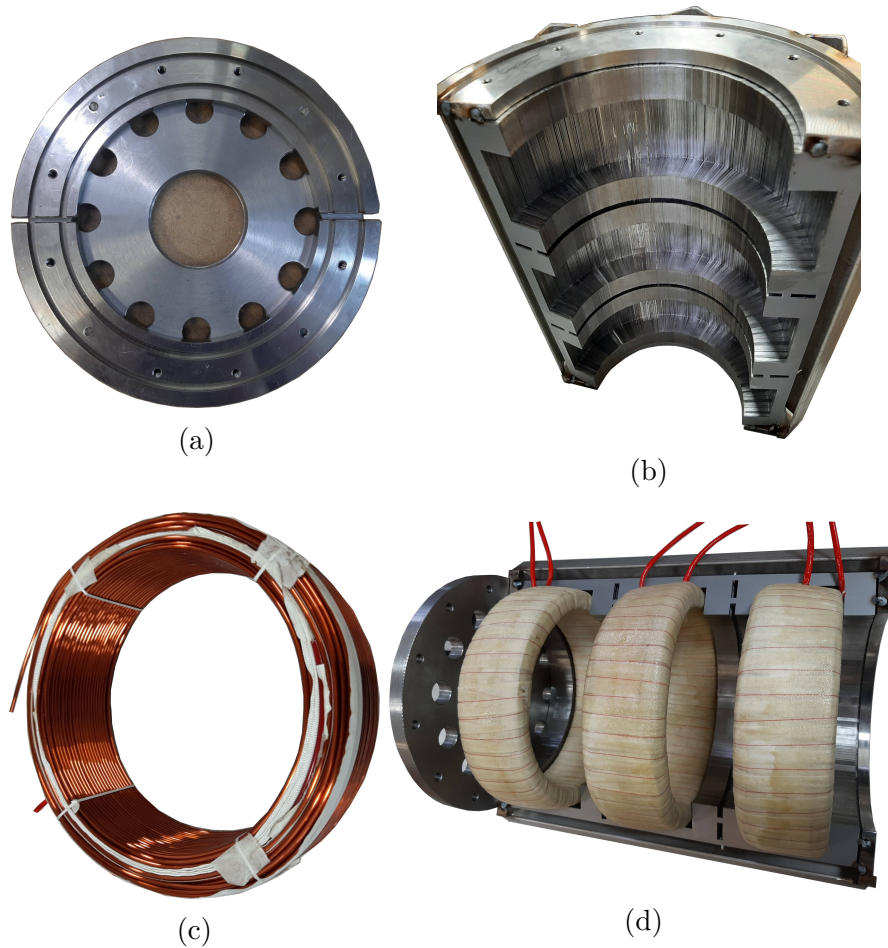


Figure 5.9: Assembly of the stator (a) End plate and lamination end plate, (b) Stacked stator half, (c) Coil before cloth and resin, (d) The coils in one half of the stator

5.3. Full assembly of the RT

The full assembly is done similar as on a regular electrical machine. The stator is placed vertically, and the rotor is lowered with the use of a crane. The bearing will ensure that the shaft is aligned once inserted. Special care is needed to ensure that the rotor connect with the stator, as it can damage the exposed coils. It is recommended to assemble the RT while only one half of the stator present, to improve visibility into the assembly. The end plate is then secured on the opposite end. The recommended half assembly without the coils is shown in Figure 5.10a.

A limitation of the manufacturing is that the designed air gap of 0.4mm was not achieved. This is possibly due to the warping of the stator plates during

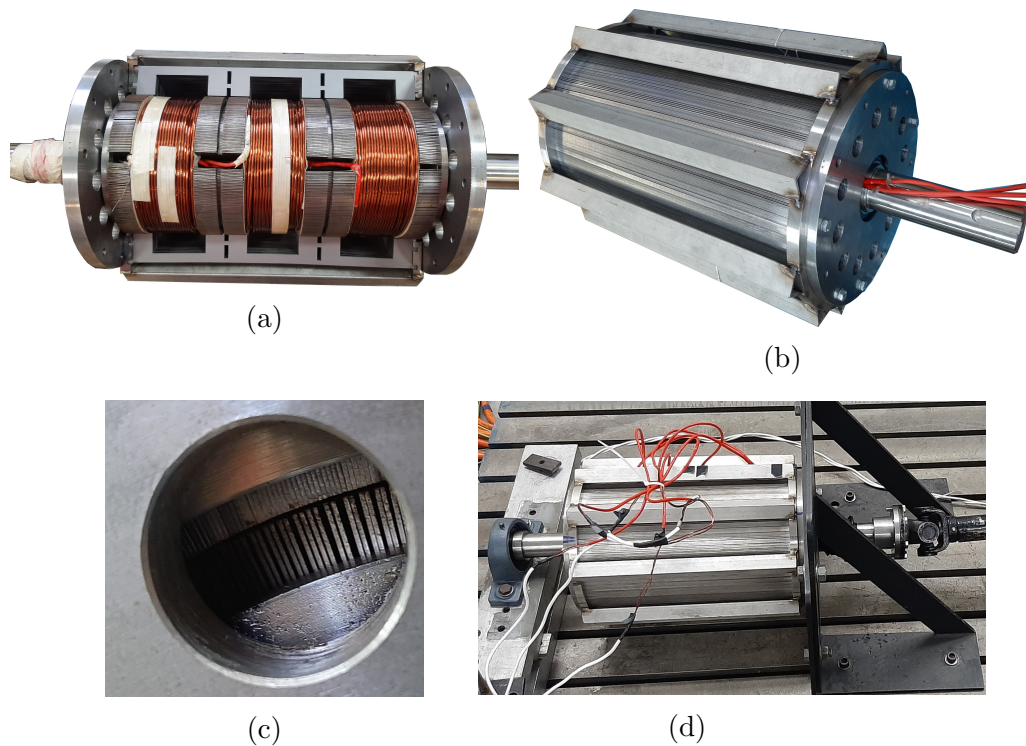


Figure 5.10: Complete assembly of the RT (a) Rotor in stator half, (b) Full assembly, (c) Inspection of the air gap, (d) RT mounted in testing

manufacturing. The achieved air gap ranges from 0.5-0.7 mm. This can be reduced to the designed 0.4mm by doing extra post-machining to the stator. However, this was not executed due to time constraints and the unavailability of equipment in the workshop. The achieved air gap is shown in Figure 5.10c. The completed RT is shown in Figure 5.10b before it is mounted, while Figure 5.10d shows the end plate and driving shaft is attached. The mounting plate drawing can be seen in Appendix E.

5.4. Summary

This chapter discusses the mechanical design and assembly of the three-phase RT. The core is constructed from laminated steel that is placed radially around a stainless-steel shaft. The laminations are held in place with small square notches on both the rotor and stator side. The rotor includes filler laminations that are placed 1:1 to increase the fill factor at the air gap to ensure a good magnetic coupling. The rotor was wound directly, and the windings are left bare at the air gap side. This was done to reduce the distance between the windings and decrease the amount of leakage flux. The rotor is internally

WYE connected and the three wires runs out on the shaft passing underneath the bearings.

Due to the stator being internally wound, it was split into two halves to accommodate the assembly of internal coils. The stator was constructed by welding the lamination holding plates together with stainless steel angle iron. This leaves the stator laminations exposed and means that the RT is of a frame-less design. The laminations were then inserted from the side and secured by welding one lamination from each side to the end plate.

The RT was assembled similar to a conventional DFIG with the advantage that one half of the core can be removed to assist with guiding the rotor in. The designed air gap of 0.4mm was not achieved due to the warping of the lamination end plates. The achieved air gap ranges between 0.5-0.7mm which reduces the magnetizing inductance. The RT is WYE connected on the rotor and can be configured in WYE or delta for the stator. It features a 1:1 winding ratio between the rotor and stator with 178 turns each.

Chapter 6

Three-phase RT measurements

To evaluate the RT designs presented in Chapter 4, an experimental three-phase RT was constructed in Chapter 5. The experimental prototype needs to be tested to determine its parameters, analyze its operation and efficiency, and evaluate its use while coupled to the RDFIG. The analytical and FEA models can be used to compare against the prototype RT. Since the air gap of 0.4mm was not obtained, the analytical and FEA models have to be updated to the correct value of 0.6mm to be a direct comparison to the prototype.

The RT is tested in both a stationary and rotating configuration. Due to a lack of slip ring and brush assemblies on the RT, measurements on the rotor are problematic whilst rotating. The first set of parameter testing was done stationary, to enable the recording of the voltage and current measurements. The RT is then mounted to the four pole DFIG in a rotor tied configuration and tested at its synchronous speed of 1500rpm. The following tests were conducted:

Resistance and inductance measurements

The resistance and inductance parameters need to be measured for the prototype RT, to experimentally verify the model developed in Chapter 4. These tests are done stationary so that both sets of windings can be accessed without a slip ring and brush assembly. The equivalent circuit that reflects these parameters is shown in Figure 6.1.

No-load testing

The RT is tested stationary under no-load test conditions by maintaining the secondary windings as an open circuit. The core losses and magnetizing current can be determined in this test. The no-load characteristic curve will provide the magnetizing current required for a given voltage level as well as to give an indication of where the RT will start to saturate. The magnetizing curve can then be compared to the analytical and FEA models.

Short circuit testing

The short circuit testing is done with the secondary windings shorted and the primary windings magnetized. The voltage is increased until the rated output current of the RT is reached. This test can determine the conduction losses in the windings as well as the impedance of the RT. This is useful to calculate voltage drop of the RTs output at a given current.

Full load measurements

To determine the efficiency of the RT at rated load it has to be tested stationary. This first limitation is due to the RDFIG rotor having a lower power output than the prototype RT at full load. The second limitation is that a slip ring and brush assembly would be required to measure current and voltage between the rotors of the RDFIG and RT. The RT is tested using a resistive load at its rated voltage. The efficiency, power factor, and total harmonic distortion can be calculated from these tests.

RDFIG coupled to RT measurements

To validate the concept of using the RDFIG with the RT, they have to be connected to each other and assumed to be one system. Standardized induction machine testing is done e.g., no-load, blocked rotor, and efficiency tests. This give the new parameters of the RDFIG with the RT being a part of the system and can be compared to the individual models of the two separate systems combined. Finally, the RT coupled RDFIG can be synchronized to the grid and tested as a generator.

6.1. Rotary transformer no-load tests

The no-load testing consists of resistance and inductance tests, an open circuit test from both the primary and the secondary side, as well as a short circuit test. These tests give the equivalent circuit parameters e.g., core loss and a verification of the inductance parameters of the RT. Voltage and current waveforms can also be obtained for the respective no-load conditions.

6.1.1. Resistance and Inductance tests

The primary (R_p) and secondary (R_s) winding resistances can be obtained by a simple DC resistance test at its rated current. To determine the magnetizing L_{mp} and leakage inductances, L_{lkp} and L_{lks} , the windings can be tested using a LCR meter. The LCR meter has set frequencies and the inductance can be calculated from tests at multiple frequencies. The alternative way is to use the

no-load testing results to determine the inductances. The following tests can be done:

- Primary winding inductance with secondary winding open $L_{p(oc)}$
- Primary winding inductance with secondary winding short circuited $L_{p(sc)}$
- Secondary winding inductance with the primary winding open $L_{s(oc)}$

From these tests the mutual inductance M can be calculated by

$$M = \sqrt{(L_{p(oc)} - L_{p(sc)})L_{s(oc)}}. \quad (6.1)$$

The magnetizing inductance L_{mp} is a function of the turns ration a between the primary and secondary number of turns and the mutual inductance. For a 1:1 winding configuration the magnetizing inductance and the mutual inductance is similar ($a = 1$). The magnetizing inductance as seen from the primary winding is

$$L_{mp} = \frac{N_s}{N_p} M = aM, \quad (6.2)$$

and from the secondary winding

$$L_{ms} = \frac{N_p}{N_s} M = \frac{M}{a}. \quad (6.3)$$

The primary and secondary leakage inductance can be determined by

$$L_{lkp} = L_{p(oc)} - L_{mp} \quad (6.4)$$

and

$$L_{lks} = L_{s(oc)} - L_{ms}. \quad (6.5)$$

The DC resistances are shown in Table 6.1 and are compared to the analytical values, as well as the measured values from the short circuit tests. The resistances obtained in the prototype compares well to the designed values.

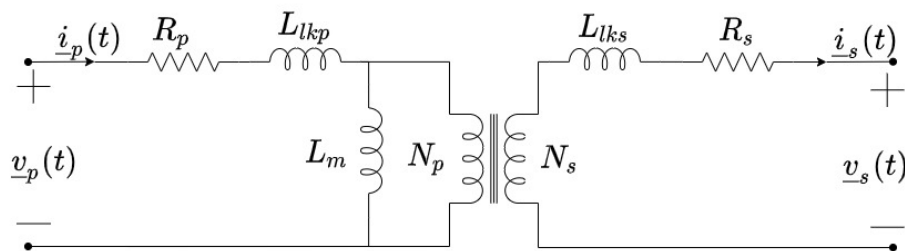


Figure 6.1: Single phase RT equivalent circuit

The inductance values of the per phase model is shown in Table 6.1. Since the air gap of 0.4mm was not obtained the inductance values are for the achieved air gap of 0.6mm. The magnetizing inductance compares well with that of the analytical and FEA model. The designed magnetizing inductance at a 0.4mm air gap is larger than what was achieved by the 0.6mm air gap and subsequently the magnetizing current is higher. This mainly effects the RT at a low load due to the proportionally higher magnetizing requirements. This is similar to conventional transformers.

Table 6.1: Inductance and resistance measurements per phase for the 0.6mm air gap RT at 25°C

	Analytical	FEA	Measured		Unit
			OC & SC Tests	LCR meter	
R_p	0.255		0.286	0.28	Ω
R_s	0.445		0.482	0.45	Ω
L_{mp}	451	455	448	450	mH
L_{llkp}	3.5	3.1	3.43	3.2	mH
L_{llks}	3.5	3.1	3.43	3.2	mH

The leakage inductance that was measured is higher than that of the FEA but compares well to the analytical values when the measured inner diameter of the coil is used. This mainly due to the secondary winding placement and positioning. The coil is double wrapped in cloth and the distance between the rotor and stator coil is not consistent throughout. None of the coils are perfectly round or perfectly straight, and their position with regards to the rotor results in a higher leakage inductance. This can be circumvented partially by the use of coils that are bare on the air gap side, similar to how the rotor was constructed as shown in Figure 5.7.

The leakage and magnetizing inductance were not tested during rotation due to a slip ring and brush assembly not being available. When testing the transformer at different orientations, the leakage inductance increases by 4% when aligning the winding slit of the rotor and the split line of the stator. The stationary values can be compared to the RDFIG coupled results in Chapter 6.3.

6.1.2. Open circuit tests

Open circuit testing consists of applying 0 - 110% of the rated voltage to either the primary or secondary set of windings by use of a variable transformer. Due

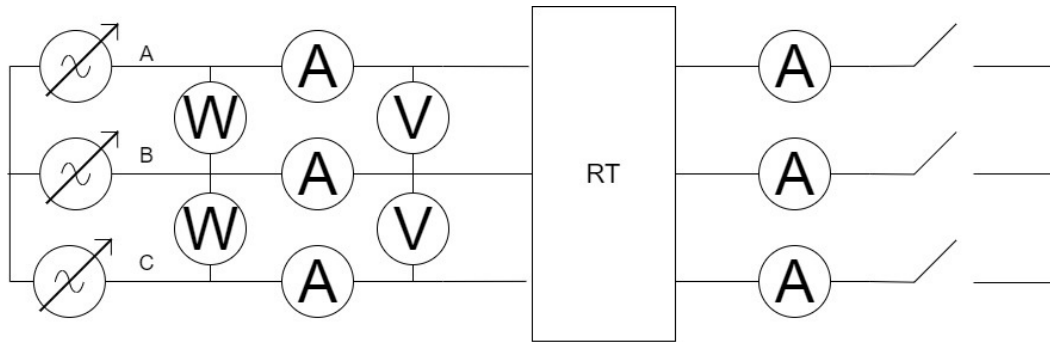


Figure 6.2: Equivalent test setup for the stationary open and short circuit RT tests

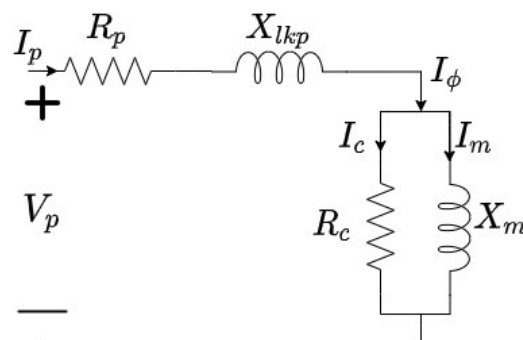


Figure 6.3: Equivalent per phase open circuit electrical model of the three-phase RT

to the operation ranges of the DFIG, the RT has to be tested from both the primary and secondary side for the DFIG to operate in motor and generator mode. Since the RT has its rotor wound in a three-phase WYE configuration without a neutral available, the applied voltage is connected in WYE for both the primary and secondary side to ensure consistency between the results. A schematic of the test setup is shown in Figure 6.2. A Delta configuration on the stator is also possible.

During the test the primary and secondary voltage is measured as a line-to-line voltage, while the magnetizing current is measured per phase. The result of this test can provide information pertaining to the magnetizing inductance of the RT as well as the core losses. The equivalent per-phase no-load circuit is shown in Figure 6.3 as seen from the primary side.

In a standard power transformer, the impedance of the magnetizing branch is high compared to the primary impedance which is the leakage inductance. In an RT, this assumption is no longer valid due to the inclusion of an air gap. The air gap increases the leakage inductance significantly and decreases the

Table 6.2: No-load measurements with calculated core parameters

Parameter	Measured value	Unit
$I_{p_{phase}}$	1.65	A
$V_{p_{phase}}$	230	V
$V_{s_{phase}}$	229	V
$P_{ocTotal}$	165	W
$X_{m_{A\&C}}$	140.9	Ω
X_{m_b}	349	Ω
R_c	962	Ω

magnetizing inductance. This can be partially compensated for by increasing the number of turns, thus leading to an increase in the magnetizing inductance. When analyzing the current of the no-load test this needs to be accounted for.

For the RT, the power draw during the no-load test does not only represents core loss. It includes the copper losses of the magnetizing branch such that the power draw of the RT becomes:

$$P = P_c + I_{p(oc)}^2 R_p \quad (6.6)$$

The measured open circuit voltage $V_{p(oc)}$ and current $I_{p(oc)}$ is used in conjunction with the primary coil's DC resistance R_p to calculate the current absorbed by the core. This current I_c represents a component of the primary current that represents the component of core loss. The current I_c can be solved by Equation (6.6). The corresponding magnetizing current I_m can then be solved by

$$I_m = \sqrt{I_{p(oc)}^2 - I_c^2}. \quad (6.7)$$

The magnetizing reactance can be calculated at the rated operating point as

$$X_m = \frac{V_{p(oc)}}{I_m}. \quad (6.8)$$

and the resulting core loss resistance R_c is found in a similar way by

$$R_c = \frac{V_{p(oc)}^2}{P_c}. \quad (6.9)$$

The results of the no-load test are shown in Table 6.2 and can be compared to the analytical and FEA results.

An important characteristic of any transformer is its no-load magnetization curve shown in Figure 6.4. This shows the amount of current required to magnetize the transformer to a specific operating voltage. The graph is obtained

by plotting the open circuit voltage of transformer versus the required current. Ideally the transformer should be in the linear region for optimal performance. If the gradient of the curve starts to level out, it gives an indication of saturation in the transformer. The knee point of the transformer is when a 50% increase in current only results in a 10 % increase in voltage. Operating a transformer in the saturation region is not ideal and will result in less than desirable operating parameters.

The RT shows a favorable magnetization curve where it does not saturate. This compares well to the FEA and analytical models, with the FEA requiring less current to magnetize. Due to manufacturing issues, a single turn from phase A was removed due to the air gap clearance. This resulted in a negligible difference (less than 1%) when comparing the voltages of the phases. The power factor at no-load is low and the lagging current of Phase A can be seen in Figure 6.5. The measured and simulated current waveforms for all three phases can be seen in Figure 6.6.

The increased no-load core losses can be attributed to the increased losses on the edges of the filler laminations as they experience a higher flux concentration than elsewhere in the core. This cause increased localized thermal losses on the rotor which is difficult to cool. Phase B has a much lower magnetization point than the other phases. This is due to the layout of the lamination,

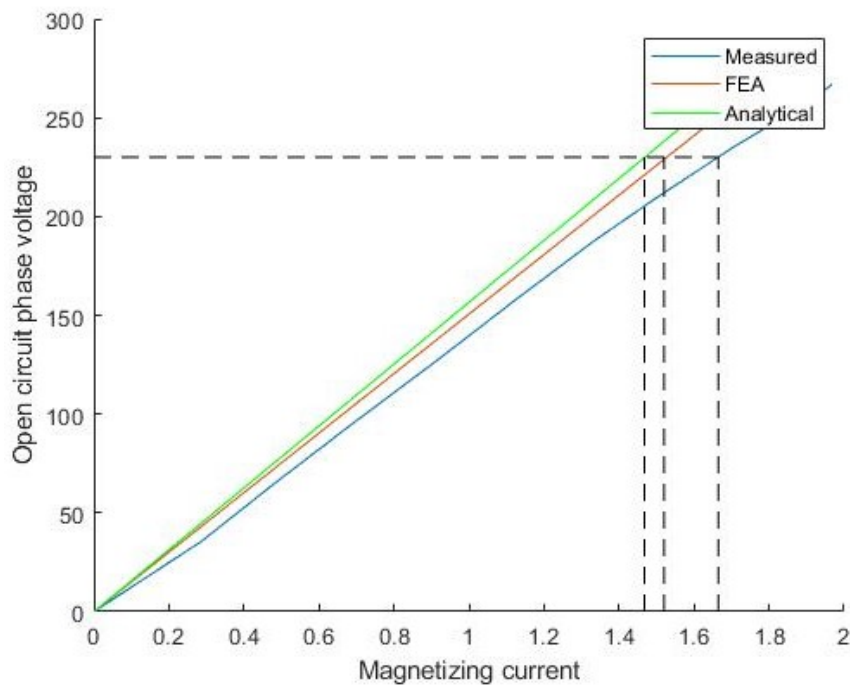


Figure 6.4: Per phase open circuit magnetization curve

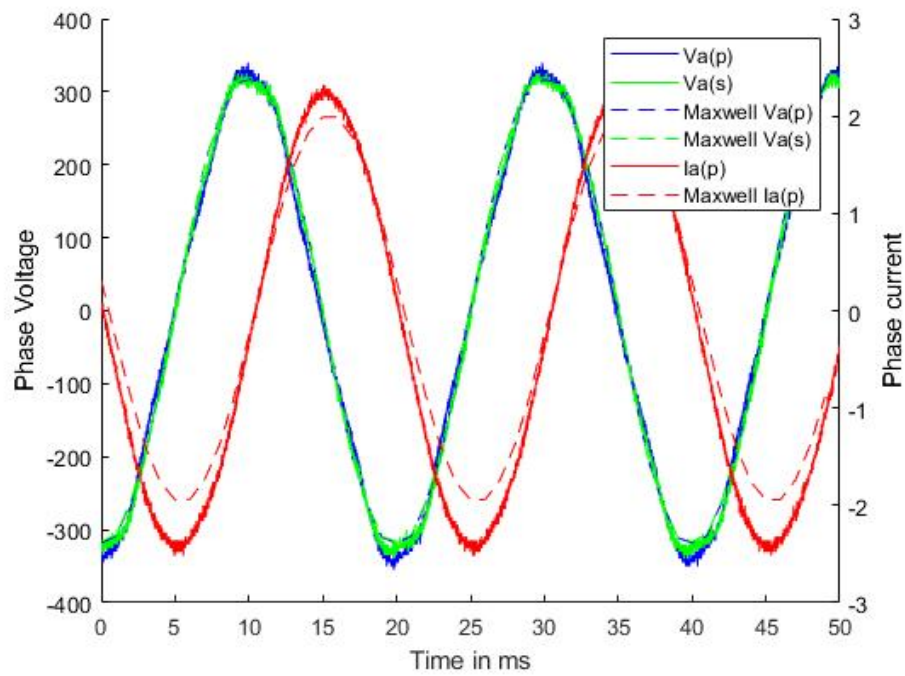


Figure 6.5: Measured and simulated phase voltage and current waveforms for phase A at no-load

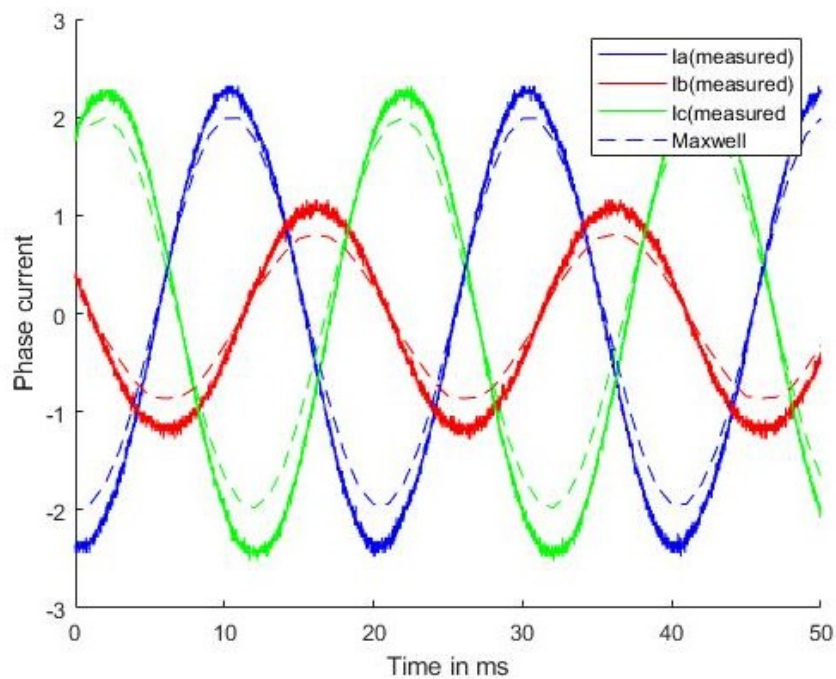


Figure 6.6: The measured and simulated current waveforms at no-load

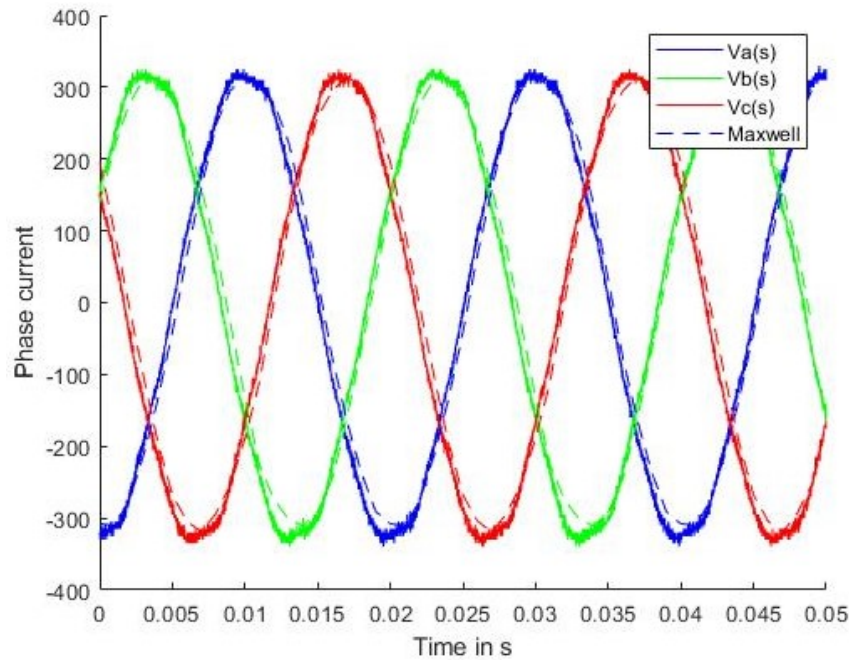


Figure 6.7: Open circuit output voltages

with the small tabs connecting the three phases acting as an easier path for the flux to flow. This became less prevalent once the RT is loaded, as they saturate fully and effectively become flux barriers. The middle core of conventional transformers often shares the same characteristics with the RT, with Phase B requiring less magnetization current. The difference between the RT and a conventional transformer mainly refers to the magnitude of the current imbalance. To solve this issue three separate phases can be used with spacing in between. In this prototype the increased cost of such a solution outweighed the benefits of separating the phases.

The voltage waveforms of the no-load tests are given in Figure 6.7. The primary and secondary voltage is consistent and smooth, indicating that saturation does not occur. Due to the ratio of magnetizing reactance X_m to core loss resistance R_c , the RT is seen more as an inductive load at open circuit conditions and will have a low power factor as seen in Figure 6.7. Comparing to the FEA, this behavior is possibly due to the construction of the core.

6.1.3. Short circuit tests

The second type of no-load test is the short circuit test. The short circuit test is used to determine the remaining RT parameters, which the open-circuit test is unable to do. One set of windings are shorted and the other is magnetized.

Table 6.3: Three-phase RT short circuit parameters

Parameter	Measured value	Unit
$I_{s_{phase}}$	8.5	A
$V_{p_{phase}}$	19.4	V
P_{sc}	175	W
$X_{lkp} + aX_{lks}$	2.16	Ω
Z_{sc}	2.28	Ω
Impedance	8.4	%

The test setup is shown in Figure 6.2. The primary voltage is increased until the secondary current reaches its rated value. The primary voltage is typically only a fraction of the rated voltage (5-10%) with the percentage commonly referred to as the impedance percentage. This is the amount of voltage required to produce the rated short circuit current. A lower impedance percentage is beneficial as there will be less of a voltage drop on the output as current increases.

During this test the induced flux is low enough to be neglected and the power loss is purely the conduction losses of the windings. The losses in the windings are given by

$$P_{sc} = I_{p(sc)}^2 (R_p + a^2 R_s) \quad (6.10)$$

with a being the turns ratio of the transformer. The equivalent circuit of the short circuit test is shown in Figure 6.8. The equivalent resistance as seen from the primary side is

$$R_{eq} = R_p + a^2 R_s, \quad (6.11)$$

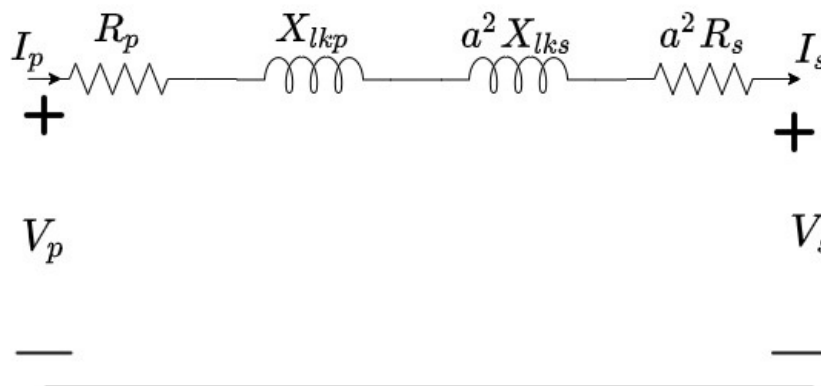


Figure 6.8: Short circuit equivalent circuit

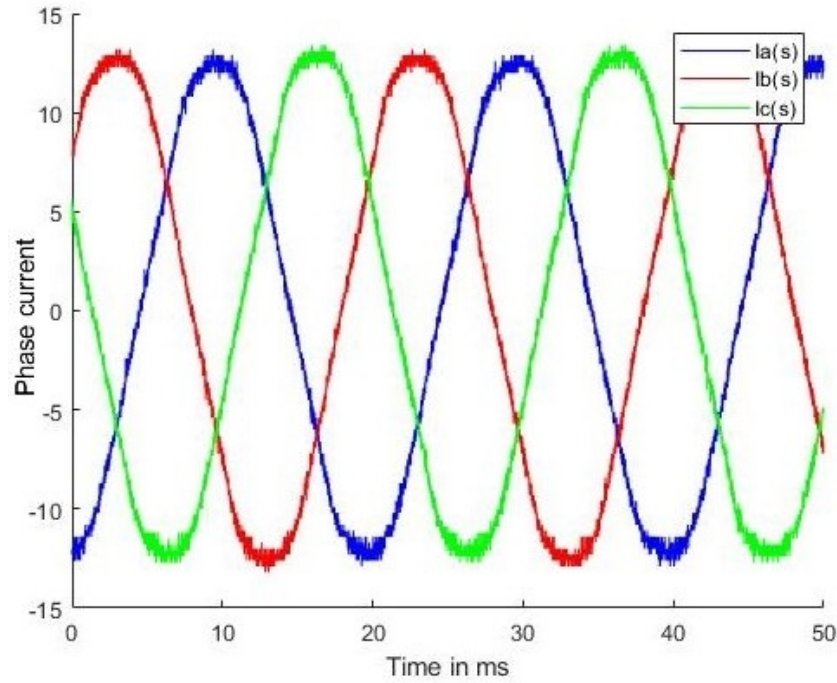


Figure 6.9: Three-phase RT Rated output short circuit currents

and similarly, the equivalent reactance is given by,

$$X_{eq} = X_{lkp} + a^2 X_{lks}. \quad (6.12)$$

The equivalent impedance Z_{sc} is required to calculate the reactance, and is given by

$$Z_{sc} = \frac{V_{p(sc)}}{I_{p(sc)}}. \quad (6.13)$$

Since the DC winding resistances of the RT are already known, it can be removed from the equation to leave only the reactance which then become

$$X_{lkp} + a^2 X_{lks} = \sqrt{Z_{sc}^2 - (R_p + aR_s)^2}. \quad (6.14)$$

Due to the nature of the air gap and the separation of the windings in the RT, the leakage reactance is higher than in conventional transformers. This leads to higher impedance that reduces the voltage regulation of the RT.

The full load current analysis is shown in Table 6.3. The measured conduction losses of the RT are 175W which is 2.9% of the total rated power of the RT. The short circuit currents are shown for the rated full load of the RT in Figure 6.9.

6.2. Full load RT testing

To evaluate the full-load performance of the RT, it has to be tested stationary. This is due to the current limitations on the rotor of the DFIG. A resistive load is used to evaluate the performance of the RT. The RT rotor (primary) is connected to a variable voltage supply in a WYE configuration. The input and output voltages are measured using an oscilloscope as well as analog meters for verification. The test setup is shown in Figure 6.10. All load tests are conducted at an input voltage of 400V L-L, with the resistance being the only factor that changes.

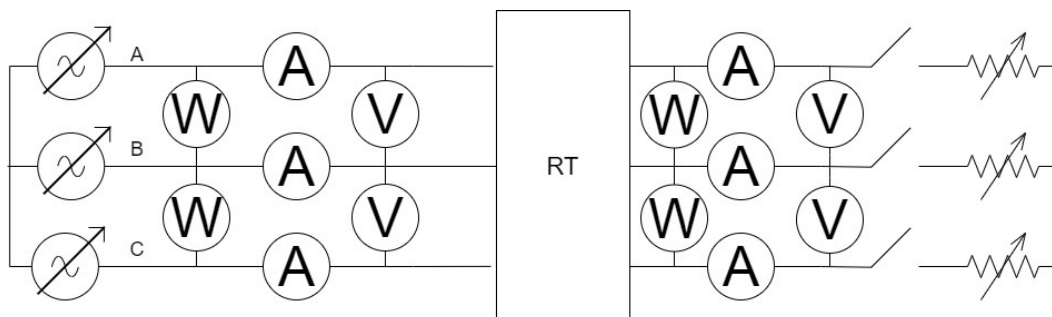


Figure 6.10: Equivalent test setup for the stationary RT load tests

To evaluate the power and efficiency, each phase of the RT has to have both input and output current, voltage, and power measurements. For the balanced resistive load, the current on the output is shown as balanced, in Figure 6.11d. The input currents are not completely balanced with a difference between Phase A and Phase C of 6%. This is likely due to an inconsistent number of turns between the phases and other manufacturing challenges that occurred during production and assembly. Phase B is consuming less current than the other phases, which is expected due to lower magnetizing requirements and mutual flux from the other two phases. Similarly, the output voltage waveform is shown in Figure 6.11b. The voltages have a 120-degree shift between them with the magnitude difference of 3% higher for phase C. This increase in voltage also attributes to the higher input current for phase C.

The results of the full-load test at rated input voltage, rated output voltage, and at 1.3 PU output current is shown in Table 6.4. The RT is able to deliver its rated output current at the rated input voltage. If the output voltage is required to be at grid voltage (400V L-L) the RT is still able to deliver a stable output. From the loading tests the efficiency can be determined from the watt-meter results and calculated by using the oscilloscope data and MATLAB. The power factor can be determined by taking the real power divided by

Table 6.4: Full-load test at (a) Rated input voltage, (b) Rated output voltage, (c) Maximum loading of 1.3PU. Voltage and currents are averaged between phases

Parameter	(a)	(b)	(c)	Unit
$I_{P_{phase}}$	8.95	9.43	12.06	A
$I_{S_{phase}}$	8.8	9.2	11.63	A
$V_{P_{phase}}$	229	241	230	V
$V_{S_{phase}}$	219	230	213	V
$P_{In_{Total}}$	6025	6620	7795	W
$P_{Out_{Total}}$	5780	6340	7430	W
PF	0.98	0.97	0.94	
Eff	96	95.8	95.6	%

the apparent power to the RT. The output is at unity power factor. At rated, the RT has a high power factor of 0.98 and is able to achieve 96% efficiency at full-load. The measured voltage and current waveforms for Phase A can be seen in Figure 6.12.

Such high efficiencies are uncommon for RTs [17,22,23], but is below the efficiency of traditional power transformers. The high leakage of the RT combined with the non-ideal topology reduces the efficiency of the RT. The topology has a low magnetic material fill factor that results in a larger RT, which in turn increases the mean length of turn for the winding, resulting in higher copper losses. To achieve a similar performance, the current density of the RT has to be reduced significantly.

To evaluate the efficiency of the RT losses as a function of current is important. The core losses of the RT remain relatively constant throughout the operation of the RT with the highest core losses observed being at no-load. The core losses will increase significantly if the RT enters saturation. The saturation of the RT is above 440V L-L so it can be assumed that it never reaches saturation during normal operation. As the current increased the copper losses in the windings also increased. The total losses of the three-phase RT as a function of current are shown in Figure 6.13. The RT will experience losses exceeding 400W at 10A and will require active cooling if operating in that region for a prolonged time.

The efficiency of the RT is of particular interest as it will affect the RT coupled to RDFIG proposal the most. A high efficiency is beneficial for the system operation. The efficiency curve for the three-phase RT operating at rated input voltage is shown in Figure 6.14, and is 96% for the RT operating at rated output power. The efficiency remains mostly constant at around 96%

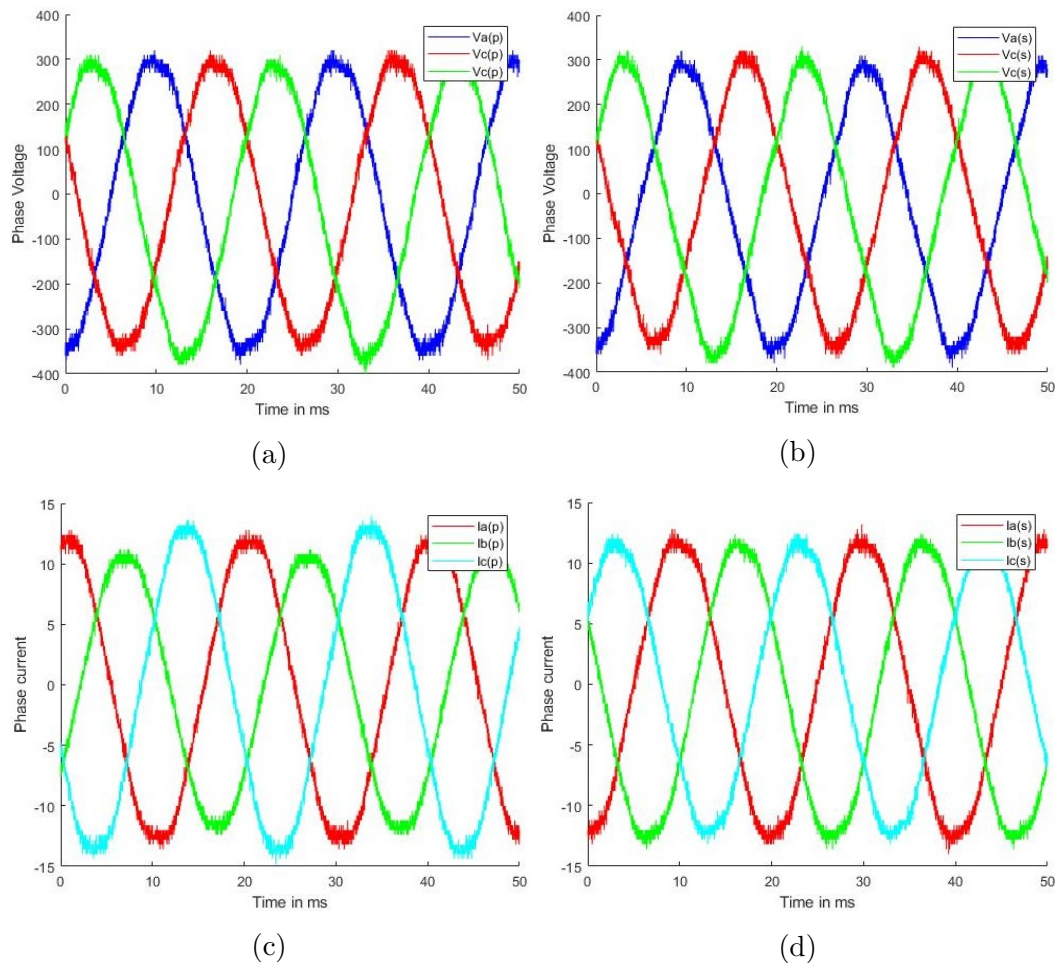


Figure 6.11: The input and output Voltage (a,b) and Current (c,d) waveforms for the three-phase RT as measured

between 4 and 6.5kW. As the load increases past this point the efficiency will reduce. The efficiency results for the specific test conditions such as at higher output voltage is shown in Table 6.4.

To analyze the voltage regulation, it has to be calculated by

$$VR\% = \frac{V_{o(NL)} - V_{o(FL)}}{V_{o(FL)}} * 100. \quad (6.15)$$

Using the results of the stationary full-load test the voltage regulation is 6%. A lower voltage regulation percentage is beneficial for the application of the RT, but due to the large leakage flux, the voltage regulation is not ideal. This can partially be compensated for by the RDFIG when the RT is grid-tied, as the RDFIG can manage a higher induced voltage if it is run via a control

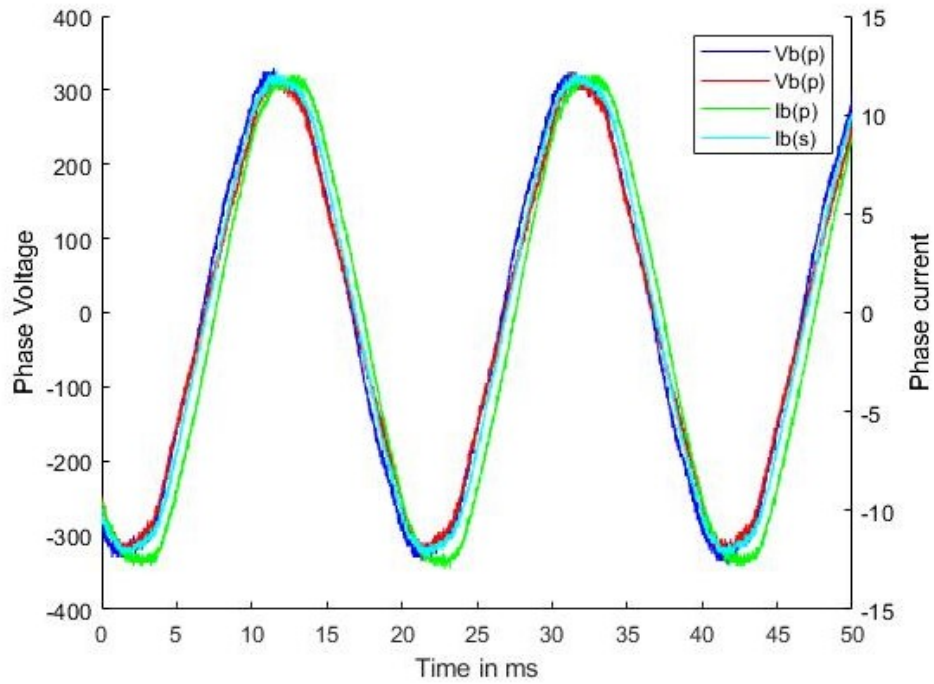


Figure 6.12: Full-load measured voltage (phase) and current waveforms for Phase A

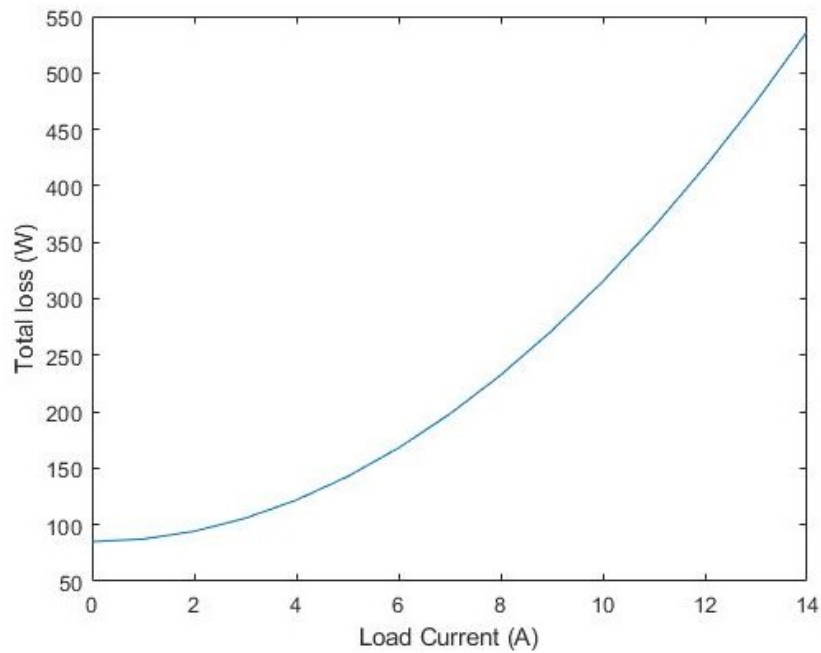


Figure 6.13: Total RT losses as a function of function of load current at rated input voltage

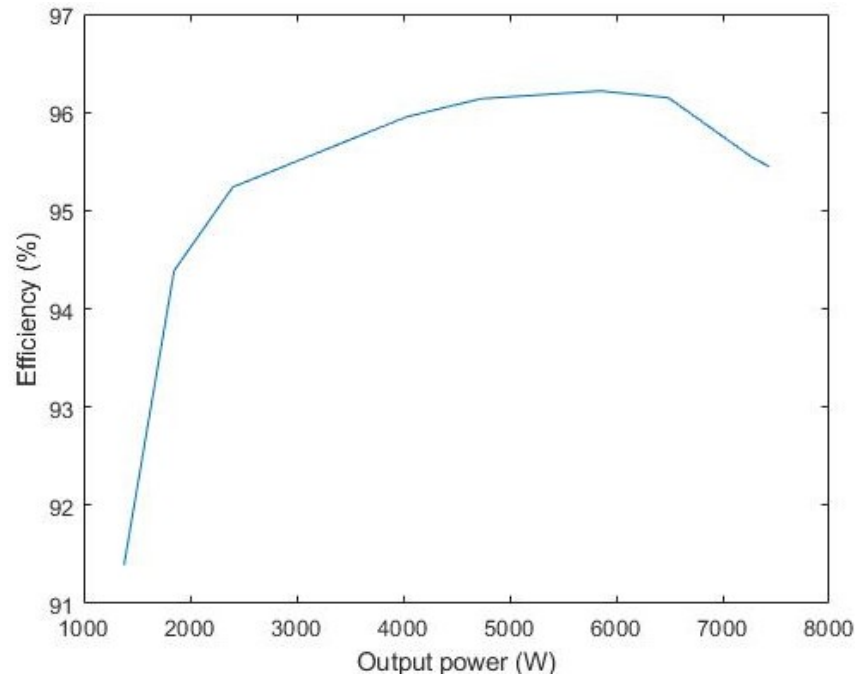


Figure 6.14: Efficiency of the three-phase RT as a function of output power at 400V L-L input voltage

system.

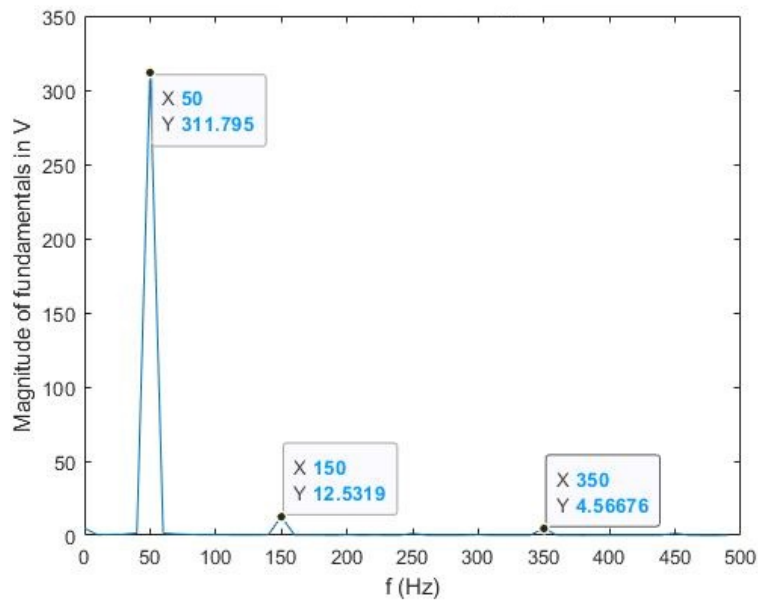


Figure 6.15: FFT of the per phase output voltage of the RT during stationary testing

To analyze the harmonics of the system, a Fast Fourier Transform (FFT) can be done on the voltages to determine the fundamental resonance frequencies. The FFT for the full-load stationary test is shown in Figure 6.15. The voltages are phase voltage. Due to the relatively large series inductance the waveforms are smooth, and the 3rd harmonic has a low magnitude. The total harmonic distortion is 1.6% meaning the RT has a very smooth sinusoidal waveform.

6.3. RDFIG coupling tests

To test the RDFIG coupling, the RT is mounted to the other side of the RD-FIG with an induction motor connected to the driving side of the RDFIG. The RDFIG can be tested in two ways, with or without the other induction motor. For all the tests the rotor of the RDFIG is connected to the RT and its windings are not directly accessible due to the lack of a slip ring and brush assembly. The rotor of the RDFIG is connected in WYE to the RT without a neutral. The field of the RDFIG is accessible on the stator. The physical test setup is shown in Figure 6.16.

6.3.1. RDFIG no-load and blocked rotor tests

To obtain the equivalent circuit parameters, the RDFIG needs to be tested at a no-load condition. During this test, the induction machine is connected and operate the system at 1500rpm to overcome rotational losses. The stator

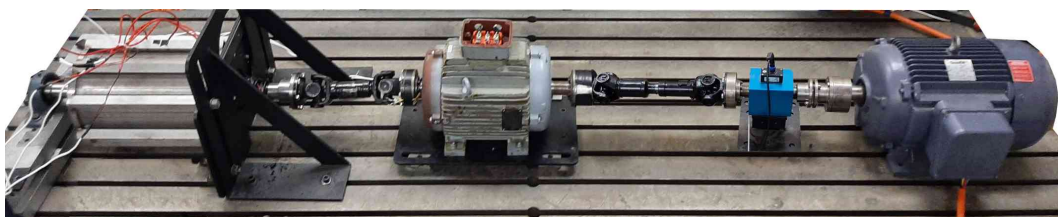


Figure 6.16: Rotor tied DFIG setup with RT on the left

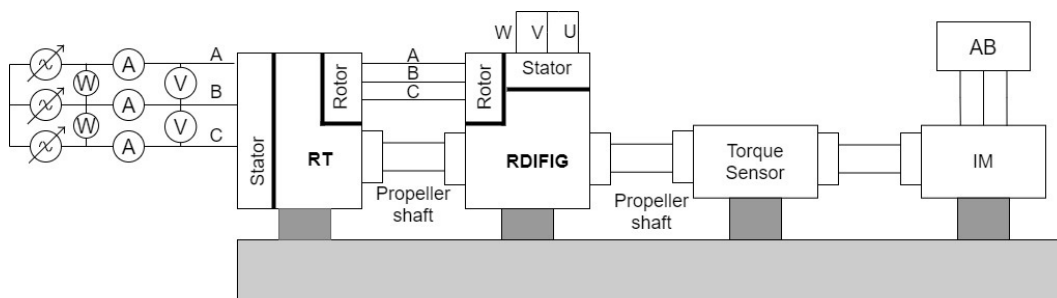


Figure 6.17: Equivalent parameter estimation test setup of RDFIG with RT

Table 6.5: RDFIG-RT No-load tests

Parameter	RDFIG alone	RDFIG with RT	Unit
I_{nl}	2.87	3.7	A
V_{nl}	230	228	V
P_{nl}	250	320	W
$P_{core_{nl}}$	204.3	212	W
X_{nl}	102.8	61.4	Ω
R_c	776.8	735.6	Ω
PF	0.125	0.126	

Table 6.6: RDFIG-RT Blocked rotor tests

Parameter	RDFIG alone	RDFIG with RT	Unit
I_{br}	6	5.97	A
V_{br}	40.3	52.1	V
P_{br}	306	380	W
X_{br}	6.04	8	Ω
R_{br}	2.83	3.52	Ω
PF	0.42	0.405	

(control windings) on the RDFIG is shorted and a grid voltage is applied to the stator of the RT. The voltage, current, and power measurements are taken before the RT. The equivalent test setup is shown in Figure 6.17. The test results are shown in Table 6.5.

The RT-RDFIG performs poorer in the no-load test due to the added inductance and resistance of the RTs windings. The power factor remains mostly unchanged as the magnetizing inductances of the RT and the RDFIG is in parallel. The RT adds an additional 70W of losses at no-load.

The blocked rotor test was conducted in a similar manner to the no-load test but with a clamp on the RDFIG shaft. The stator of the RDFIG is still shorted and the input power to the RT is from a variable transformer. The blocked rotor tests are conducted with the RDFIG rotor determining the rated current. The results from the blocked rotor test are shown in Table 6.6.

6.3.2. RDFIG equivalent circuit parameters

To determine the equivalent circuit parameters the two equivalent circuits of the DFIG and RT are combined. The full RDFIG circuit is shown in Figure 6.18. Although this circuit is complex, it can easily be solved with the

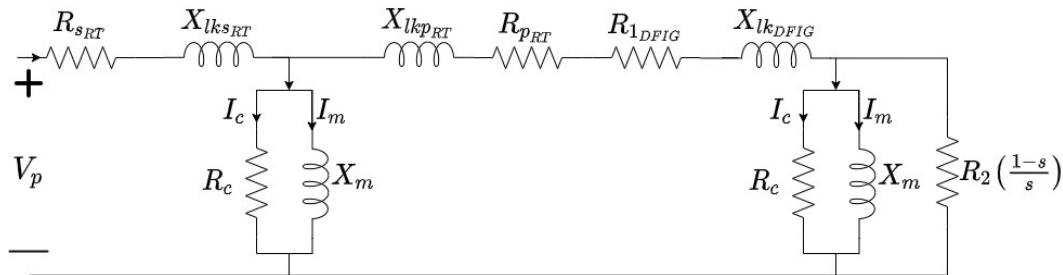


Figure 6.18: RDFIG with RT per phase full equivalent circuit

Table 6.7: DFIG with RT equivalent circuit parameters

Parameter	Value	Unit
$R_{s_{RT}}$	0.482	Ω
$R_{p_{RT}}$	0.286	Ω
$R_{1_{DFIG}}$	1.85	Ω
$R_{2_{DFIG}}$	1.89	Ω
$X_{lk_{s_{RT}}}$	1.08	Ω
$X_{lk_{p_{RT}}}$	1.08	Ω
$X_{lk_{DFIG}}$	6.25	Ω
$X_{m_{RT}}$	140.9	Ω
$X_{m_{DFIG}}$	96.55	Ω
$R_{c_{RT}}$	962	Ω
$R_{c_{DFIG}}$	776.8	Ω

aid of a computer software package. The RDFIGs and the RTs equivalent circuits are from previous tests and then run in a simulation to confirm the results obtained by the coupling test. The full set of parameters are given in Table 6.7, and these parameters compare well against tested results.

To simplify the analysis, the circuit is condensed into a shortened circuit with only one leakage reactance, series resistance, magnetizing branch, and R_2 which is still a function of slip. The resultant simplified circuit is shown in Figure 6.19. The resultant equivalent circuit has more inductance in series and a lower magnetizing inductance at no-load. The equivalent simplified circuit parameters are shown in Table 6.8. The RDFIG coupled to RT has some disadvantages compared to the RDFIG on its own namely: higher series inductance that will lower the power factor and increased magnetizing current and losses. The advantages are: a higher tolerance to grid faults, lower maintenance requirements, and increased mechanical inertia.

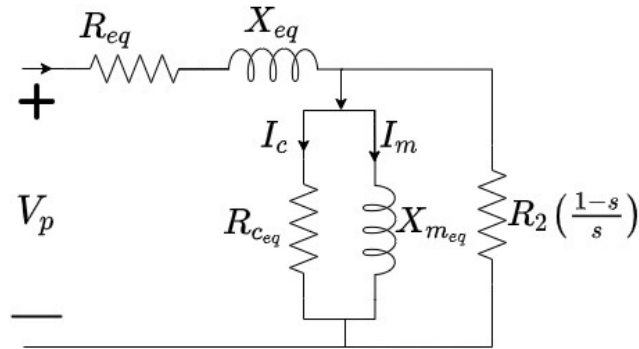


Figure 6.19: RDFIG with RT per phase simplified equivalent circuit

Table 6.8: DFIG with RT equivalent circuit parameters

Parameter	Value	Unit
R_{eq}	2.66	Ω
X_{eq}	8.41	Ω
$X_{m_{eq}}$	57.3	Ω
R_{ceq}	430	Ω

6.3.3. RDFIG load tests

There are two ways of connecting the RDFIG to a load. The first is the use of a resistive load, while the second is to grid-tie the RT and push power into the grid. Due to a lack of a controller, the testing is conducted on the rotor tied DFIG at its rated synchronous speed of 1500rpm. The DFIG was initially developed by [37]. The DFIG is tested under similar conditions to evaluate the use of the RT. The load chosen is a resistive load.

The maximum output of the DFIG shaft is 4.49kW of power, therefore, the RT is tested with that as its input. The rated output power after losses is then 4.2kW, which is below the rating of the RT, but demonstrates its ability to work in its intended role. Rotational losses such as additional friction and vibration from the RT are included in the efficiency calculation. The resultant output voltage and current waveforms to the load is shown in Figures 6.20 and 6.21 respectively.

A key factor for determining the viability of the proposed solution is the efficiency. The DFIG is tested with and without the RT to determine the efficiency at the same load point (full load). The efficiency for the RDFIG is 87% and for the RT-RDFIG 82%, as shown in Table 6.9. The core losses in the RT are less at full load than at no-load, which relates to a high total efficiency of the system. The system as tested experienced higher than ex-

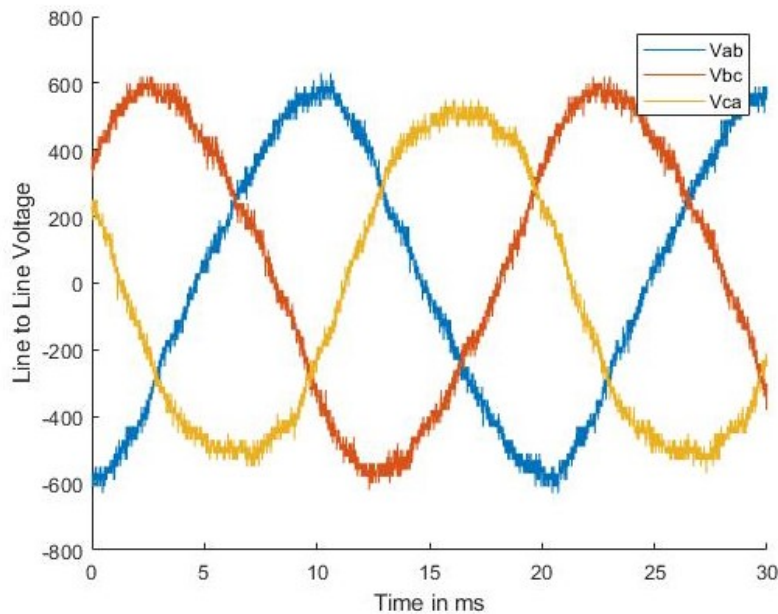


Figure 6.20: Output voltage of the rotor tied to RT-RDFIG

pected mechanical losses as would be with the combined mechanical losses for the RT and RDFIG which is 310W. The RDFIG itself has a lower mechanical losses. A better test setup could result in lower mechanical losses and therefore marginally higher efficiency.

The voltage and current waveform stability and total harmonic distortion (THD) is also of particular interest as this shows how stable the coupling of the DFIG is. The THD for the RT during DFIG coupling is 1.93% for the voltage which is better than the DFIG on its own at 3.83%. This is likely due

Table 6.9: RDFIG coupled testing

Parameter	Value		Unit
	Slip ring assembly	RT coupled	
I_{load}	6.37	5.98	A
V_{load}	235	226	V
$I_{DFIG_{stator}}$	8	9	A
$V_{DFIG_{stator}}$	30.4	34.2	V
P_{shaft}	5166	5010	W
P_{load}	4490	4110	W
n	87	82	%
PF	1	1	
V_{THD}	3.83%	1.93	%
C_{THD}	2.4%	1.85	%

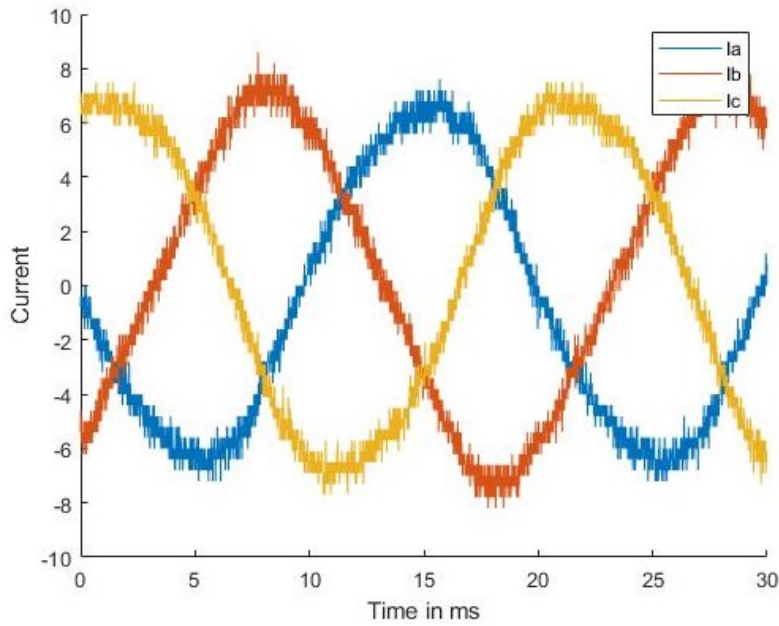


Figure 6.21: Output current of the RT coupled RDFIG

to added inductance that smooths out the voltage and current. The current THD is also lower at 1.85% compared to 2.4%. This shows that the coupling of the RT is indeed stable. The FFT of the output voltage is shown in Figure 6.22.

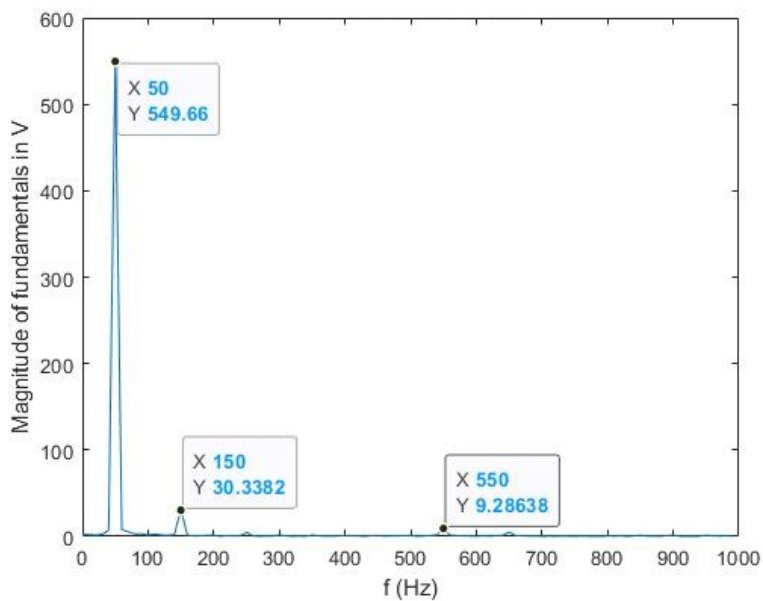


Figure 6.22: FFT of the output voltage (L-L) during DFIG coupled tests

Long term thermal testing was done in this configuration but was limited by the rotor power output of the DFIG and does not match the full load current expected by the RT. It is not expected to overheat at operation below full load. Thermal test results are shown in Chapter 6.4.

6.4. Thermal results

To determine the operating temperature of the RT, a thermal analysis has to be done. Since the RT is not an ideal transformer and has losses, it will heat up over time. The total losses in the RT as a function of output current is shown in Figure 6.13. As the losses increase, the temperature of the RT will also increase. The expected steady state temperature is dependent on the currents in the RT and it is shown in Figure 6.23.

To validate the thermal model, the RT was connected to the RDFIG and ran at the RDFIGs rotor's rated voltage and current for two and a half hours. The output current was 6A at $400V_{LL}$ resulting in 4.2kW of power. At 6A the RT is only experiencing less than half of its rated conduction loss as would be at 9A. This is a limitation of the setup, but the data can still be compared to the analytical model. The results of the thermal testing is shown in Figure 6.25. The RT was operating at its expected rotor temperature of 50

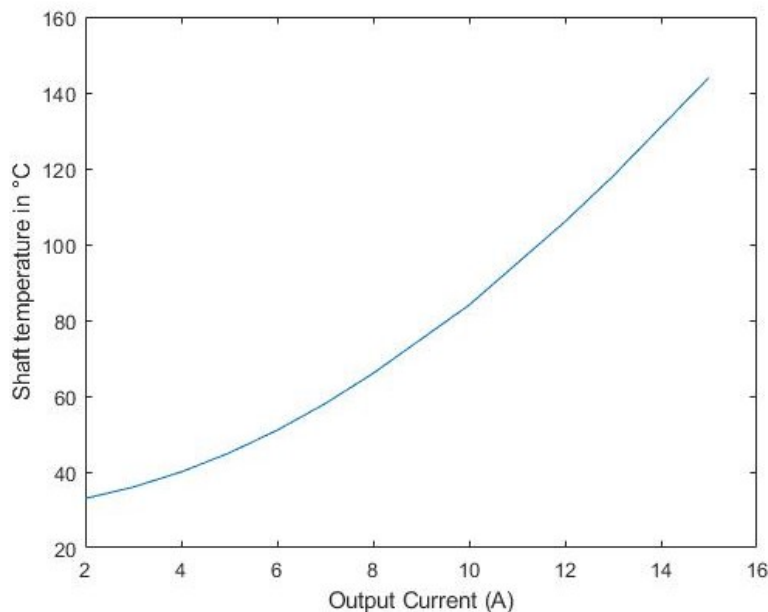


Figure 6.23: Simulated rotor shaft temperature at steady state without a fan for a given output current

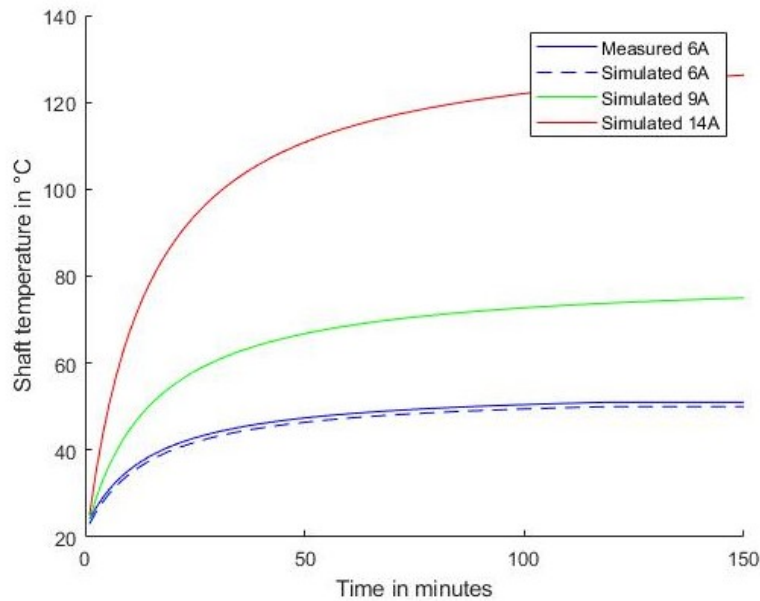


Figure 6.24: Measured and simulated rotor shaft temperature without a fan over time

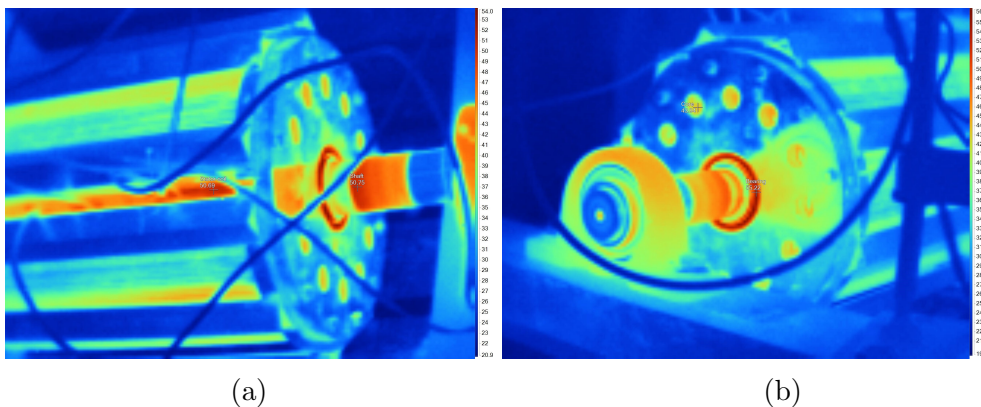


Figure 6.25: Thermal testing results of the RT after 2.5 hours at 6A

$^{\circ}\text{C}$. Due to the RT not being painted, the emissivity is low and infra-red (IR) measurements are difficult to obtain accurately. The shaft is partially covered by black insulation tape to increase the accuracy of the reading as the shaft was rotating during the measurement. The hot spot as shown in Figure 6.25a is measured on the insulation tape and the shaft appeared cooler around the spot which is not accurate due to the rotation.

The expected operating temperature of the RT will be higher when it is at full load. The thermal limit will be the middle coil on the rotor, since

it is difficult to cool directly. The inner part of the coil is estimated to be around 50°C hotter than the extruded part of the shaft due to the distance and insulation between them. The laminations will also be hotter than the shaft. At full load the shaft is estimated to be at 75°C . At 11A (1.2PU) the RT will effectively overheat as the resistance of the coils will increase and the external shaft temperature will be at 95°C . At loadings above rated the RT requires active cooling that can be achieved by mounting a fan on the shaft.

6.5. Summary

In this chapter the prototype three-phase RT is tested to evaluate its performance against the designed parameters. The RT is first tested stationary to determine its equivalent circuit parameters. The values compare well with the analytical and FEA results indicating that the design process was successful. The RT is then tested stationary to determine its full load efficiency. It manages to have an efficiency of 96% at a 5.8KW output to a resistive load at a power factor of 0.98. At 1.2PU the RT was able to deliver 7.4kW at an efficiency of 95.6% but at a much lower power factor of 0.94.

The RT is then connected to a RDFIG to evaluate the operation of the system. The standard RT-RDFIG was then tested at no-load, blocked rotor, and full load. The system has higher losses due to the increased resistance in the system but manages to deliver the full rated voltage and current of the RDFIGs rotor. The system manages an efficiency of 82% at full load compared to 87% for the RDFIG on its own. The RT-RDFIG performs better in terms of its voltage and current THD due to the increased inductance of the RT coils. The system will also be less sensitive to grid faults and will require less maintenance than a DFIG with slip rings.

Finally, the prototype RT is tested in its configuration with the RDFIG to determine its steady state thermal point. The test is done at the RDFIGs maximum current of 6A which is below the rated output of the RT. The RT shaft heated up to 50°C and the thermal testing correlates well with the analytical model. At rated load the RT's shaft is expected to be at 75°C and increased loads will require active cooling.

Chapter 7

Conclusion

The conventional DFIG is widely used due to its low cost, simplicity, and variable speed range. The main problem with using a DFIG is the reliability and high cost of maintenance when slip ring and brush assemblies are used. To increase the reliability, research is being done on brushless generator topologies. The BDFIG is an alternative to the DFIG but results in a more complex machine. The use of a standard DFIG with an RT is a proposed alternative to the standard BDFIG. To be a viable replacement for slip rings and other brushless topologies, the DFIG with an RT needs to be of comparable size and efficiency.

To reduce the size of the RT at a given power rating, a higher frequency can be used. This is achieved by the use of a RDFIG. The RDFIG has its power windings on the rotor and has an output frequency of 50Hz. This requires the RT to handle most of the power of the DFIG. The advantage is that the DFIG has both variable speed and variable power factor. A lower power factor range will be achieved when coupled with a RT.

The main focus of this study was to develop a design procedure for a 50Hz, rotor-tied, three-phase RT. An analytical model is developed from the conventional transformer model and adapted to include the effects that are only present in a RT. Specific emphasis on correction factors such as a reducing fill factor in a radially laminated core. This poses several difficult design challenges due to an inconsistent fill factor at the air gap, where the stator has a much higher amount of magnetic material present.

Using this model, a design procedure is presented that reduces the core size and increases the winding area for a given power rating. This results in a better magnetic coupling of the RT that is not very sensitive to air gap changes and therefore resilient to vibrations. An increased number of turns also increases the magnetizing inductance of the RT and improves its performance when not fully loaded. The design procedure produces first a single core RT that can be used in a three-phase configuration.

The single core topology is then evaluated in a single-lamination, three-phase configuration with and without shared inner limbs. Both designs are viable, with the shared limb offering better power density, and the separated limb design being easier to cool and more resilient to manufacturing problems such as an inconsistent air gap length. The analytical model is used in conjunction with finite element analysis to determine the optimal RT parameters. A design is presented with the separated limb topology.

A three-phase prototype was constructed and compared to the analytical and FEM simulations to verify the accuracy of the proposed design procedure. The prototype did not achieve the designed air gap distance of 0.4mm, instead an air gap of 0.6mm was achieved. The RT is compared to the design with a 0.6mm air gap and parameter testing showed that the design was successful, and the RT had the expected parameters. The RT did have higher leakage inductance which is attributed to the stator coil construction not being perfect.

The three-phase RT is capable of delivering an output power of 5.8kW at 96% efficiency and a 0.98 power factor. The RT is able to handle an output of up to 1.3PU at a 95.6% efficiency. At such high currents the less than desirable leakage inductance reduces the power factor to 0.94. Due to the high impedance percentage of the RT it is not well suited to driving loads above its rated output.

The three-phase RT was then connected in its designed configuration, rotor-tied to a RDFIG. Parameter testing of the system is done and compared to the equivalent parameters of the RDFIG with slip rings. The RT-RDFIG has a lower power factor and efficiency than the RDFIG with slip rings. The concept of using a RT with a RDFIG has some advantages namely its ability to be a contact-less solution, and the increased series inductance indicates that it is more resilient to grid faults. The RT-RDFIG proves that the concept of replacing the slip rings is a viable option even though it has drawbacks.

Bibliography

- [1] IEA, “World Energy Outlook 2019,” *World Energy Outlook 2019*, p. 1, 2019.
- [2] J. Lee and F. Zhao, “Global Wind Report 2021,” *Glob. Wind Energy Counc.*, p. 75, 2021.
- [3] GWEC, “Global Wind Report 2018,” *Wind energy Technol.*, no. April, p. 61, 2019.
- [4] IRENA, “FUTURE OF WIND Deployment, investment, technology, grid integration and socio-economic aspects,” tech. rep., International Renewable Energy Agency, Abu Dhabi, 2019.
- [5] SEWEA, “SOUTH AFRICA’S UTILITY-SCALE WIND & RE INDUSTRY Key data as at March 2019,” Tech. Rep. March, 2019.
- [6] T. C. Morphology, “Integrated Resource Plan (IRP2019),” tech. rep., South African Department of Mineral resources and energy, 2019.
- [7] H. Polinder, J. A. Ferreira, B. B. Jensen, A. B. Abrahamsen, K. Atallah, and R. A. McMahon, “Trends in wind turbine generator systems,” *IEEE J. Emerg. Sel. Top. Power Electron.*, vol. 1, no. 3, pp. 174–185, 2013.
- [8] M. D. Reder, E. Gonzalez, and J. J. Melero, “Wind Turbine Failures - Tackling current Problems in Failure Data Analysis,” *J. Phys. Conf. Ser.*, vol. 753, no. 7, 2016.
- [9] Y. X. Wenping Cao and Z. Tan, “Wind Turbine Generator Technologies,” *Intech*, vol. i, no. tourism, p. 13, 2016.
- [10] P. J. Tavner, J. Xiang, and F. Spinato, “Reliability analysis for wind turbines,” *Wind Energy*, vol. 10, no. 1, pp. 1–18, 2007.
- [11] S. Pfaffel, S. Faulstich, and K. Rohrig, “Performance and reliability of wind turbines: A review,” *Energies*, vol. 10, no. 11, 2017.
- [12] J. López, P. Sanchis, X. Roboam, and L. Marroyo, “Dynamic behavior of the doubly fed induction generator during three-phase voltage dips,” *IEEE Trans. Energy Convers.*, vol. 22, no. 3, pp. 709–717, 2007.

- [13] L. G. Meegahapola, T. Littler, and D. Flynn, "Decoupled-DFIG fault ride-through strategy for enhanced stability performance during grid faults," *IEEE Trans. Sustain. Energy*, vol. 1, no. 3, pp. 152–162, 2010.
- [14] C. Wessels, F. Gebhardt, and F. W. Fuchs, "Fault ride-through of a DFIG wind turbine using a dynamic voltage restorer during symmetrical and asymmetrical grid faults," *IEEE Trans. Power Electron.*, vol. 26, no. 3, pp. 807–815, 2011.
- [15] U. Hoffmann, "Direct grid connection and low voltage ride-through for a slip synchronous-permanent magnet wind turbine generator," no. March, 2012.
- [16] M. Alizadeh, R. Ghazi, E. E. Haghani, and M. E. Rad, "Improving Analysis of Low Voltage Ride Through Capability in Turbines Connected to The Brushless Doubly Fed Induction Generator (BDFIG) under Fault Conditions," *34th Int. Power Syst. Conf. PSC 2019*, pp. 655–661, 2019.
- [17] N. L. Zietsman and N. Gule, "Design and evaluation of a 1.2 kVA single phase rotary transformer," *Proc. - 2016 22nd Int. Conf. Electr. Mach. ICEM 2016*, pp. 1466–1472, 2016.
- [18] Y. Xu, *Kilowatt Three-phase Rotary Transformer Design for Permanent Magnet DC Motor with On-rotor Drive System*. PhD thesis.
- [19] M. Ruviaro, F. Rüncoş, and N. Sadowski, "Wound Rotor Doubly Fed Induction Machine with Radial Rotary Transformer," *J. Microwaves, Optoelectron. Electromagn. Appl.*, vol. 12, no. 2, pp. 411–426, 2013.
- [20] M. Ruviaro and F. Runcos, "A brushless doubly fed induction machine with flat plane rotary transformers," *Proc. - 2012 20th Int. Conf. Electr. Mach. ICEM 2012*, pp. 23–29, 2012.
- [21] H. Zhong, C. Wu, and Y. Wang, "Design and analysis of rotary transformer for brushless doubly fed induction generators," *Proc. 13th IEEE Conf. Ind. Electron. Appl. ICIEA 2018*, no. May, pp. 1416–1419, 2018.
- [22] H. R. Mohabati, J. S. Moghani, and S. T. Boroujeni, "Fully laminated shell-type three-phase rotating transformer for brushless applications," *IET Electr. Power Appl.*, vol. 9, no. 5, pp. 349–357, 2015.
- [23] H. Zhong, L. Zhao, and X. Li, "Design and Analysis of a Three-Phase Rotary Transformer for Doubly Fed Induction Generators," *IEEE Trans. Ind. Appl.*, vol. 51, no. 4, pp. 2791–2796, 2015.
- [24] T. A. Lipo, D. Panda, and D. Zarko, "Design and Test of DC Voltage Link Conversion System and Brushless Doubly-Fed Induction Generator

- for Variable-Speed Wind Energy Applications: August 1999–May 2003,” no. November, 1999.
- [25] R. A. McMahon, E. Abdi, P. D. Malliband, S. Shao, M. E. Mathekga, and P. J. Tavner, “Design and testing of a medium-speed 250 kW Brushless DFIG,” *Eur. Wind Energy Conf. Exhib. 2012, EWEC 2012*, vol. 1, pp. 207–212, 2012.
- [26] R. Carlson, H. Voltolini, F. Rüncoş, P. Kuo-Peng, and N. J. Batistola, “Performance analysis with power factor compensation of a 75 kW brushless doubly fed induction generator prototype,” *Proc. IEEE Int. Electr. Mach. Drives Conf. IEMDC 2007*, vol. 2, pp. 1502–1507, 2007.
- [27] H. Liu and L. Xu, “Design and performance analysis of a doubly excited brushless machine for wind power generator application,” *2nd Int. Symp. Power Electron. Distrib. Gener. Syst. PEDG 2010*, pp. 597–601, 2010.
- [28] P. Tavner, E. Abdi, M. Tatlow, and R. McMahon, “Design and performance analysis of a 6 MW medium-speed brushless DFIG drivetrain,” *Eur. Wind Energy Conf. Exhib. EWEC 2013*, vol. 2, pp. 977–983, 2013.
- [29] M. Tosi, *Rotary Transformer Design for Brushless Electrically Excited Synchronous Machines*. PhD thesis, 2014.
- [30] H. Krupp and A. Mertens, “Rotary Transformer Design for Brushless Electrically Excited Synchronous Machines,” *2015 IEEE Veh. Power Propuls. Conf. VPPC 2015 - Proc.*, pp. 1–6, 2015.
- [31] A. M. Knight, R. E. Betz, and D. G. Dorrell, “Design and analysis of brushless doubly fed reluctance machines,” *IEEE Trans. Ind. Appl.*, vol. 49, no. 1, pp. 50–58, 2013.
- [32] M. Bhawalkar, G. Narayan, and Y. Nerkar, “Optimal Design of Brushless Doubly Fed Reluctance Machine,” *Intech*, vol. i, no. Optimization and Control of Electrical Machines rated, p. 13, 2018.
- [33] M. Moazen, R. Kazemzadeh, and M. R. Azizian, “Mathematical modeling and analysis of brushless doubly fed reluctance generator under unbalanced grid voltage condition,” *Int. J. Electr. Power Energy Syst.*, vol. 83, pp. 547–559, 2016.
- [34] R. E. Betz, M. G. Jovanovic, and M. G. Jovanovic, “The brushless doubly fed reluctance machine and the synchronous reluctance machine - a comparison,” *IEEE Trans. Ind. Appl.*, vol. 36, no. 4, pp. 1103–1110, 2000.
- [35] D. G. Dorrell and M. Jovanovic, “On the possibilities of using a brushless doubly-fed reluctance generator in a 2 MW wind turbine,” *Conf. Rec. - IAS Annu. Meet. (IEEE Ind. Appl. Soc.)*, 2008.

- [36] Y. M. You, T. A. Lipo, and B. I. Kwon, "Design and analysis of a novel grid-connected to rotor type doubly fed induction machine," *IEEE Trans. Magn.*, vol. 48, no. 2, pp. 919–922, 2012.
- [37] O. I. Olubamiwa and N. Gule, "The optimal design and autonomous testing of a rotor-tied DFIG," *2017 IEEE AFRICON Sci. Technol. Innov. Africa, AFRICON 2017*, pp. 1378–1383, 2017.
- [38] R. Gibson, "Rotary transformers developed to replace slip rings and brushes," *Electr. Eng.*, vol. 80, no. 6, pp. 469–471, 1961.
- [39] E. E. Landsman, "Rotary transformer design," *1970 IEEE Power Electron. Spec. Conf.*, pp. 139–152, 1970.
- [40] T. Raminosa and R. Wiles, "Contactless Rotor Excitation for Traction Motors," *2018 IEEE Energy Convers. Congr. Expo. ECCE 2018*, pp. 6448–6453, 2018.
- [41] J. Duan, B. Lin, Q. Yang, and Y. Luan, "Design and testing of a novel rotary transformer for rotary ultrasonic machining," *IEICE Electron. Express*, vol. 14, no. 23, pp. 1–9, 2017.
- [42] N. L. Zietsman and N. Gule, "Evaluation of a single-phase 50-Hz axial rotary transformer for DFIG systems," *IEEJ Trans. Electr. Electron. Eng.*, vol. 13, pp. 311–321, feb 2018.
- [43] M. Ruviaro, F. Rñncos, N. Sadowski, and I. M. Borges, "Analysis and test results of a brushless doubly fed induction machine with rotary transformer," *IEEE Trans. Ind. Electron.*, vol. 59, no. 6, pp. 2670–2677, 2012.
- [44] S. Botha and N. Gule, "Design of a contact-less energy transfer system for electrically excited synchronous machines," *2020 Int. Symp. Power Electron. Electr. Drives, Autom. Motion, SPEEDAM 2020*, pp. 460–465, 2020.
- [45] C. McLyman, *Transformer and Inductor Design Handbook, Fourth Edition*. 2011.
- [46] K. D. Papastergiou and D. Ewen Macpherson, "An airborne radar power supply with contactless transfer of energy - Part II: Converter design," *IEEE Trans. Ind. Electron.*, vol. 54, no. 5, pp. 2885–2893, 2007.
- [47] J. P. Smeets, L. Encica, and E. A. Lomonova, "Comparison of winding topologies in a pot core rotating transformer," *Proc. Int. Conf. Optim. Electr. Electron. Equipment, OPTIM*, no. 1, pp. 103–110, 2010.

- [48] J. P. Smeets, D. C. Krop, J. W. Jansen, M. A. Hendrix, and E. A. Lomonova, "Optimal design of a pot core rotating transformer," *2010 IEEE Energy Convers. Congr. Expo. ECCE 2010 - Proc.*, pp. 4390–4397, 2010.
- [49] M. Ruviaro, F. Rüncoş, N. Sadowski, and I. M. Borges, "Design and Analysis of a Brushless Doubly Fed Induction Machine with Rotary Transformer," *Int. Conf. Electr. Mach. -ICEM*, pp. 1–6, 2010.
- [50] M. J. Martin, "Smart Grid: Energy Harvesting," 2015.
- [51] B. A. Potter and S. A. Shirsavar, "Design, implementation and characterisation of a contactless power transfer system for rotating applications," *IECON Proc. (Industrial Electron. Conf.)*, pp. 2168–2173, 2006.
- [52] S. Zurek, "Air gap - Encyclopedia Magnetica."
- [53] N. L. Zietsman and N. Gule, "Optimal design methodology of a three phase rotary transformer for doubly fed induction generator application," *Proc. - 2015 IEEE Int. Electr. Mach. Drives Conf. IEMDC 2015*, pp. 763–768, 2016.
- [54] Y. Qiu, W. Zhang, M. Cao, Y. Feng, and D. Infield, "An electro-thermal analysis of a variable-speed doubly-fed induction generator in a wind turbine," *Energies*, vol. 8, no. 5, pp. 3386–3402, 2015.
- [55] W. G. Hurley, W. H. Wölflé, and J. G. Breslin, "Optimized transformer design: Inclusive of high-frequency effects," *IEEE Trans. Power Electron.*, vol. 13, no. 4, pp. 651–659, 1998.
- [56] R. R. Kumar, S. K. Singh, R. K. Srivastava, and R. K. Saket, "Dynamic reluctance air gap modeling and experimental evaluation of electromagnetic characteristics of five-phase permanent magnet synchronous generator for wind power application," *Ain Shams Eng. J.*, vol. 11, no. 2, pp. 377–387, 2020.
- [57] J. Mühlenthaler, J. W. Kolar, and A. Ecklebe, "A novel approach for 3D air gap reluctance calculations," *8th Int. Conf. Power Electron. - ECCE Asia "Green World with Power Electron. ICPE 2011-ECCE Asia*, pp. 446–452, 2011.
- [58] J. C. Olivares-Galvan, P. S. Georgilakis, E. Campero-Littlewood, and R. Escarela-Perez, "Core lamination selection for distribution transformers based on sensitivity analysis," *Electr. Eng.*, vol. 95, no. 1, pp. 33–42, 2013.
- [59] C. P. Steinmetz, "On the law of hysteresis," *Proc. IEEE*, vol. 72, no. 2, pp. 197–221, 1984.

Appendix A

Transformer equations

This chapter consists of the general transformer theory that is used in the design of the three-phase RT. The equations listed is for a general transformer, with the layout specific derivations for the RT done in Chapter 3.

A.1. General transformer theory

The basic law of operation of a transformer is the creation of magnetic field by current flowing through a wire. The magneto motive force (MMF) applied to the core is a function of the Ampere turn product

$$\mathcal{F} = N_p \underline{i} = \oint \underline{H}.d\mathbf{l} \quad (\text{A.1})$$

where \mathcal{F} is the MMF, \underline{H} is the magnetic field intensity and \underline{i} is the current flowing through the conductor. The differential element $d\mathbf{l}$ is the length along the path of integration.

The total flux ϕ in an enclosed area A is

$$\phi = \int B.dA \quad (\text{A.2})$$

where B is the flux density. If the flux density is considered to be constant throughout the area, the integral can be solved and the Equation (A.2) becomes

$$\phi = BA \quad (\text{A.3})$$

Faraday's law can be used to determine the induced voltage e_{ind} as a function of the flux ϕ and number of primary turns N_p by

$$e_{ind} = N_p \frac{d\phi}{dt}. \quad (\text{A.4})$$

From the duality principle, the MMF is analogous to the voltage in an electric circuit. The relationship between the flux and MMF is described by

$$\underline{\mathcal{F}} = \phi \mathcal{R} \quad (\text{A.5})$$

where \mathcal{R} is the reluctance of the magnetic path. The reluctance is analogous to the resistance in an electric circuit and is given by

$$\mathcal{R} = \frac{\ell}{\mu_o \mu_r A}, \quad (\text{A.6})$$

with μ_o being the permeability of free space, μ_r being the relative permeability of the material, ℓ the length of the magnetic path and A the area of the path.

Assuming that all of the flux induced by the primary coil reaches the secondary coil, the voltage ratio can be described by the turns ratio of the primary and secondary coil by

$$a = \frac{V_p}{V_s} = \frac{N_p}{N_s}. \quad (\text{A.7})$$

A.2. Inductance of a transformer

A.2.1. Magnetizing inductance

The inductance L of any winding can be described as

$$L = \frac{N^2}{\mathcal{R}} \quad (\text{A.8})$$

where N is the number of turns in the winding.

Since not all of the flux that is developed by the primary winding passes through to the secondary winding, the flux can be expressed as two separate entities. The flux that flows in both windings is known as the mutual flux ϕ_m . The other developed flux is known as leakage flux and is separate for each winding. The total flux in each of the windings can be described by

$$\phi_p = \phi_m + \phi_{lkp} \quad (\text{A.9})$$

$$\phi_s = \phi_m + \phi_{lks} \quad (\text{A.10})$$

where ϕ_{lkp} and ϕ_{lks} are the primary and secondary leakage flux. The terminal voltages can be expressed as a differential equation and it is a function of the resistances and inductances

$$\begin{bmatrix} \underline{v}_p(t) \\ \underline{v}_s(t) \end{bmatrix} = \begin{bmatrix} L_{11} & L_{12} \\ L_{21} & L_{22} \end{bmatrix} \frac{d}{dt} \begin{bmatrix} \underline{i}_p(t) \\ \underline{i}_s(t) \end{bmatrix} + \begin{bmatrix} R_p \\ R_s \end{bmatrix} \begin{bmatrix} \underline{i}_p(t) \\ \underline{i}_s(t) \end{bmatrix} \quad (\text{A.11})$$

with L_{11} and L_{22} being the self inductances of the primary and secondary windings. $L_{12} = L_{21}$ and represents the mutual inductance between the two windings. R_p and R_s are the primary and secondary winding resistances.

The self inductances of the windings are derived in a similar manner to the flux. They are divided into two components, the magnetizing and leakage inductance. These are the inductances used by the equivalent circuit model in Figure 3.4. The primary and secondary self inductances can be written as

$$L_{11} = L_{mp} + L_{lkp}, \quad (\text{A.12})$$

$$L_{22} = L_{ms} + L_{lks}. \quad (\text{A.13})$$

The magnetizing inductance L_m is directly proportional to the energy required to magnetize the transformer core and is a function of the geometry and material of the transformer. L_{mp} and L_{ms} are the magnetizing inductance when the transformer is magnetized from the primary and the secondary side respectively. L_{12} is the mutual flux that links the two windings. The inductance is a function of the turns ratio of the transformer and can be expressed as

$$L_{mp} = \frac{N_p}{N_s} L_{12}, \quad (\text{A.14})$$

A.2.1. Leakage inductance

As it is nearly impossible to determine the leakage flux lines of the RT, reluctance modeling can not be utilized due to inaccuracies. To achieve an accurate model the leakage inductance can be calculated from the amount of energy stored in the windings and in the air gap [45, 57]. The stored energy W_m can be determined by evaluating the flux density B and the field intensity H in the windings within the volume of the core v so that

$$W_m = \int \frac{1}{2} \underline{H} B \, dv \quad (\text{A.15})$$

can be expressed as a function of the current $\underline{i}(t)^2$ and leakage inductance L_{lk} so that

$$W_m = \frac{1}{2} L_{lk} \underline{i}(t)^2 \quad (\text{A.16})$$

From the primary side the leakage flux can be evaluated by determining the field intensity in the air gap as

$$\underline{H}_{ag} = \frac{N_p \underline{i}(t)}{l_{ag}} \quad (\text{A.17})$$

with l_{ag} being the air gap distance. Using the geometry presented in Figure 3.5b, Equation (A.17) becomes

$$\underline{H}_{ag} = \frac{N_p \underline{i}(t)^2}{r_4 - r_3} \quad (\text{A.18})$$

To determine the field intensity in the primary winding, the length of the coil affects the field intensity so that the axial (z-direction) field intensity becomes:

$$\underline{H}_p(z) = \frac{N_p \underline{i}_p(t)}{2l_1} \frac{z}{r_3 - r_2}, \quad (\text{A.19})$$

and similarly for the secondary winding;

$$\underline{H}_s(z) = \frac{N_s \underline{i}_s(t)}{2l_1} \frac{z}{r_5 - r_4}, \quad (\text{A.20})$$

Assuming that there is no saturation, Equation (A.15) can be re-evaluated with the field intensities so that the average energy stored becomes

$$W_m = \frac{1}{2} \mu_0 \underline{H}^2 \times v. \quad (\text{A.21})$$

Appendix B

RT coupled RDFIG

The RDFIG is tested in two configurations namely: with a slip ring and brush assembly and with the three-phase RT. The test conditions are otherwise unchanged for both configurations. The test setup is shown in Figures 6.16 and 6.17.

B.1. RDFIG testing procedure

During the no-load test the stator of the RDFIG is shorted. The 11kW induction motor is spun up to the rated 1500rpm. For the test without the RT, the slip rings are used and the RT is not connected. By the use of an external variac the input voltage on the rotor is increased to the rated line-to-line voltage of 400V. The current and voltage waveforms are then captured by the oscilloscope. The power readings are done by both the watt-meters and the oscilloscope for validation. In all the tests the analog measurements are used in conjunction with the oscilloscope to ensure validity of the results.

The blocked rotor test is done in a similar manner. The shaft is clamped to stop the setup from rotating. The stator is still shorted during this test. The current on the rotor is increased to 6A and the measurements are taken. The test setup and location of the measuring equipment is shown in Figure 6.17.

For the RT-RDFIG the test conditions are exactly the same with the only variable being that the applied voltage and current levels are now tested before the input of the RT stator. Due to the lack of slip rings when the RT is connected, the measurements cannot be taken at the input to the RDFIG.

B.2. RDFIG parameter calculations

The resistance of the RDFIG rotor is measured first. Due to no neutral the resistance is measured in line-to-line in the form of

$$R_1 = \frac{1}{2}R_{LL}. \quad (\text{B.1})$$

For each of the tests the power measured is

$$P_{total} = P_1 + P_2. \quad (\text{B.2})$$

Due to the use of the external 11kW induction motor the windage and friction losses can be neglected and therefore the core loss is

$$P_{core} = P_{nl} - 3I_{nl}^2 R_1 \quad (\text{B.3})$$

The total apparent power for both the tests are calculated in the same way in the form of

$$S_{total} = \sqrt{3}V_{LL}I_1. \quad (\text{B.4})$$

The reactive power can be calculated from the real and apparent power as

$$Q_{total} = \sqrt{S_{total}^2 - P_{total}^2}. \quad (\text{B.5})$$

The equivalent core resistance for the RDFIG can be calculated in the form of

$$R_c = \frac{V_{nl}^2}{P_{core}} \quad (\text{B.6})$$

The no-load reactance can be calculated in the form of

$$X_{nl} = \frac{Q_{nl}}{3I_{nl}^2}. \quad (\text{B.7})$$

The blocked rotor parameters R_{bl} and X_{bl} can be calculated as

$$R_{bl} = \frac{P_{bl}}{3I_{bl}^2}, \quad (\text{B.8})$$

$$X_{bl} = \frac{Q_{bl}}{3I_{bl}^2}. \quad (\text{B.9})$$

Assuming that the induction machine has a distribution of its reactance in the form of $X_2 = X_1$, the values can be calculated in the form of

$$X_2 = (X_{bl} - X_2) \frac{X_{nl} - X_2}{X_{nl} - X_{bl}}. \quad (\text{B.10})$$

The magnetizing reactance can be calculated in the form of

$$X_m = X_{nl} - X_1. \quad (\text{B.11})$$

The equivalent load resistance R_2 can be calculated as

$$R_2 = (R_{bl} - R_1) \frac{X_m + X_2}{X_m}. \quad (\text{B.12})$$

The equivalent circuit for the RDFIG is shown in Figure B.1.

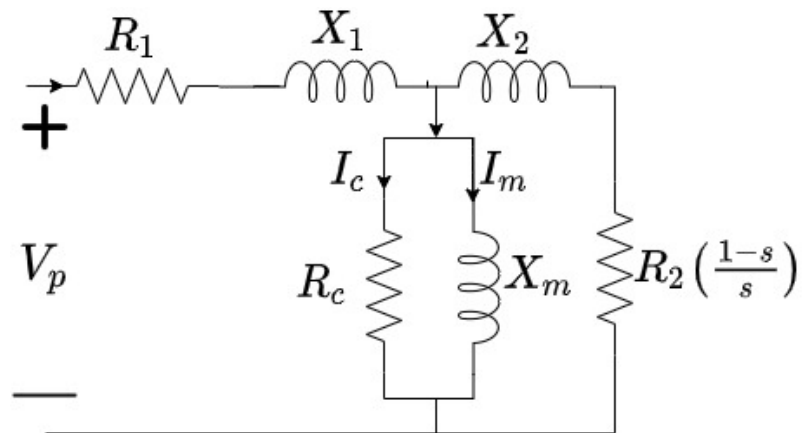


Figure B.1: RDFIG equivalent circuit

Appendix C

Thermal design

C.1. Natural convection

If the air temperature (T_∞) is assumed to be at 25 °C and we want a surface (T_s) temperature of less than 70 °C, we can approximate the film temperature of the air T_f to be

$$T_f = \frac{T_s + T_\infty}{2} \quad (\text{C.1})$$

The properties of air such as kinematic viscosity ν , coefficient of volume expansion β , thermal diffusivity k and Prandtl number Pr can all be obtained from standard air property tables. If the Rayleigh number

$$Ra = \frac{g\beta(T_s - T_\infty)D^3}{\nu^2} Pr \quad (\text{C.2})$$

is lower than 10^{12} then we can assume that the RT is a horizontal cylinder. D is the diameter of the RT and g is the gravitational acceleration.

The natural convection Nusselt number Nu can then be determined from

$$Nu = \left(0.6 + \frac{0.387 Ra^{1/6}}{[1 + (0.559/Pr)^{9/16}]^{8/27}} \right)^2 \quad (\text{C.3})$$

The heat transfer coefficient h in $W/m \cdot K$ is then

$$h = \frac{k}{D} Nu \quad (\text{C.4})$$

C.2. Radiation heat transfer

The rate of which energy is absorbed is denoted by the absorptivity of the material β , the reflectivity by η and the transmissivity by κ . The sum of these is always equal to one.

$$\beta + \eta + \kappa = 1 \quad (\text{C.5})$$

Reflective surfaces are called opaque and if radiation can pass through the material it is called semi-transparent. Since steel is not semi-transparent the transformer will only have a value for reflectivity and absorption. Since regular air consists primarily of nitrogen and oxygen, it neither absorbs nor emits radiation. The radiation heat transfer can therefore be assumed to only be between two surfaces.

The heat flow density between any two surfaces is defined by the Stefan-Boltzmann equation

$$q_{th} = \frac{\phi_{th}}{S} = \epsilon_{thr} \sigma_{SB} (T_1^4 - T_2^4) \quad (\text{C.6})$$

where T_1 and T_2 is the temperatures of the two surfaces. σ_{SB} is the Stefan-Boltzmann constant at $5.67 \times 10^{-8} \text{W/m}^2 \text{K}^4$. The relative emissivity between the two surfaces ϵ_{thr} is a function of their position relative to each other and the surface characteristics. If all the radiation from surface S_1 meets surface S_2 then

$$\frac{1}{\epsilon_{thr}} = \frac{1}{\epsilon_{th1}} + \frac{S_1}{S_2} \left(\frac{1}{\epsilon_{th2}} - 1 \right) \quad (\text{C.7})$$

Since electrical machines are not true black bodies, $\epsilon_{th} = 1$, the relative emissivity will be less than one. For a gray painted electrical machine the relative emissivity can be estimated at $\epsilon_{thr} = 0.85$. Similarly to electrical resistance, the thermal resistance of radiation is

$$R_{th} = \frac{T_1 - T_2}{\phi_{th}} = \frac{T_1 - T_2}{\epsilon_{thr} \sigma_{SB} (T_1^4 - T_2^4) S} = \frac{1}{\alpha_r S}, \quad (\text{C.8})$$

where

$$\alpha_r = \epsilon_{thr} \sigma_{SB} \frac{T_1^4 - T_2^4}{T_1 - T_2}, \quad (\text{C.9})$$

is the heat transfer coefficient of radiation. This coefficient depends strongly on the temperatures of the two surfaces.

C.3. Internal forced convection

To determine if the air flowing through the inside of the shaft or casing is laminar or turbulent, we can compute the Reynolds number Re in the circular tube as

$$Re = \frac{\rho V_{avg} D}{\mu} = \frac{4\dot{m}}{\mu \pi D} \quad (\text{C.10})$$

with ρ and V_{avg} being the density and velocity of the air, D being the inner diameter of the hollow shaft. μ is the dynamic viscosity of air and \dot{m} is the

mass flow rate of the air. Since determining the Reynolds number accurately is often not achievable in practice, for inner pipe flows it is considered turbulent if the Reynolds number is higher than 4000. The entrance region length is not of concern if the flow is turbulent and it can then be assumed to be a fully developed flow.

In the case of a constant surface temperature the derived heat transfer is

$$\ln \frac{T_s - T_e}{T_s - T_m} = -\frac{hA_s}{\dot{m}c_p} \quad (\text{C.11})$$

with T_s being the surface temperature, T_i and T_e being the inlet and exit temperatures respectively. c_p is the specific heat of air and h is the heat transfer coefficient. Since we are interested primarily in the combined heat transfer \dot{Q} , we can substitute and obtain

$$\dot{Q} = -hA_s\Delta T_{lm} \quad (\text{C.12})$$

with the log mean temperature difference being

$$\Delta T_{lm} = \frac{T_i - T_e}{\ln[(T_s - T_e)/(T_s - T_i)]}. \quad (\text{C.13})$$

The average convection heat transfer coefficient h is yet unknown, but with the use of the Nusselt number for smooth tubes

$$Nu = 0.023Re^{0.8}Pr^{1/3} \quad (\text{C.14})$$

the average convection heat transfer coefficient can be calculated and becomes

$$h = \frac{k}{D}Nu \quad (\text{C.15})$$

with k being the heat capacity ratio of air. The mean fluid exit temperature T_e can be determined from

$$T_e = T_s - (T_s - T_i) \exp\left(\frac{-hA_s}{\dot{m}c_p}\right) \quad (\text{C.16})$$

which can be used to determine the log mean temperature difference in Equation (C.13). This allows us to calculate the overall heat transfer of the internal forced convection at a specific surface temperature.

Appendix D

RDFIG vs conventional DFIG operation

One of the most important aspects of a grid-coupled generator is to provide a constant voltage and frequency that matches the grid. An advantage of using a DFIG is that it can handle relatively large variations in wind speed while still maintaining the grid voltage and frequency. The output of the generator is controlled by the frequency and amplitude of the control winding. In the DFIG the magnetic field direction and frequency of the rotor determines the speed of the rotor if the grid voltage and frequency is to be retained.

The frequency that needs to be applied to the control winding to maintain grid frequency on the power winding while there are changes in the mechanical speed is

$$f_c = f_p - f_m \quad (\text{D.1})$$

with f_c being the frequency applied to the control winding, f_p being the frequency induced on the power winding and f_m is the rotors mechanical frequency, given by

$$f_m = \frac{n_m \times p}{120} \quad (\text{D.2})$$

where n_m is the mechanical speed and p is the number of poles in the machine.

The DFIG has two modes that it can operate in which is dependent on the speed of the rotor, sub- and super-synchronous. The slip concepts describe the relative motion between the mechanical speed and the rotating magnetic field and is given by

$$s = \frac{n_s - n_m}{n_s} = \frac{\omega_s - \omega_m}{\omega_s}, \quad (\text{D.3})$$

where n_s is the synchronous speed. ω_s and ω_m denotes the synchronous and mechanical angular velocities respectively. The synchronous speed for a machine with the frequency f is given by

$$n_s = \frac{120f}{p}. \quad (\text{D.4})$$

The power flow out of the generator can be expressed by

$$P_m = P_p + P_c \quad (\text{D.5})$$

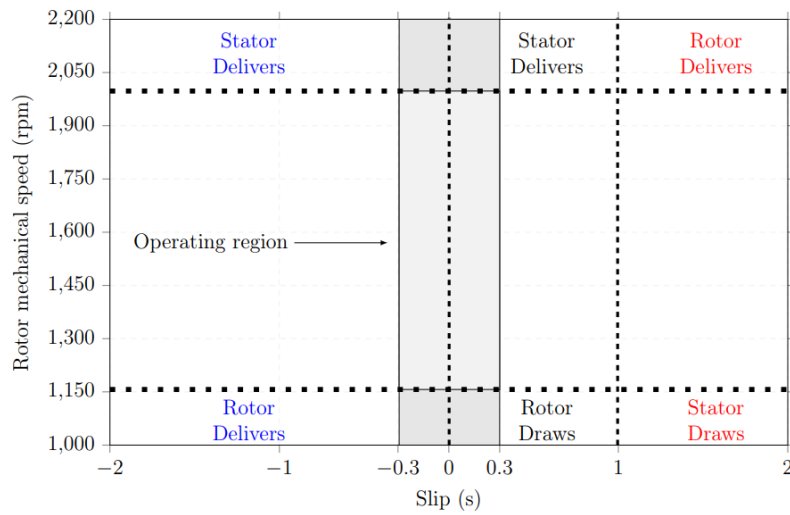


Figure D.1: Operating regions of a 50Hz, 4 pole DFIG

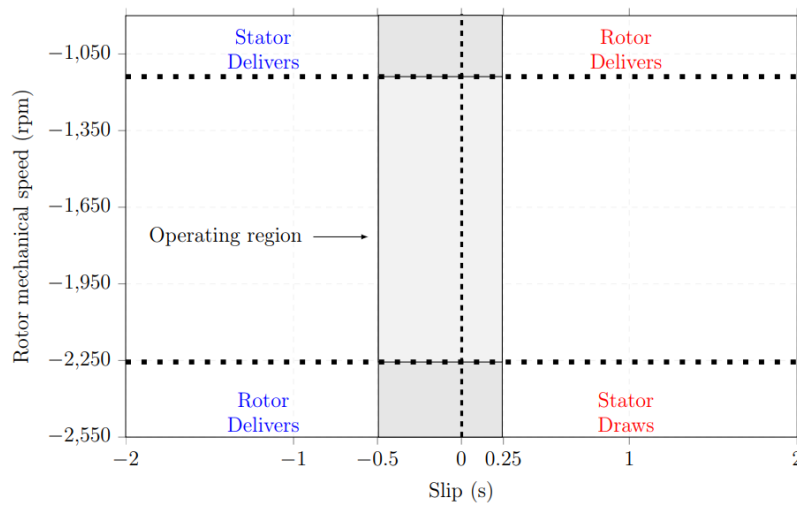


Figure D.2: The operating regions of a 4 pole, 50 Hz RDFIG, with the field and mechanical rotation in opposite directions

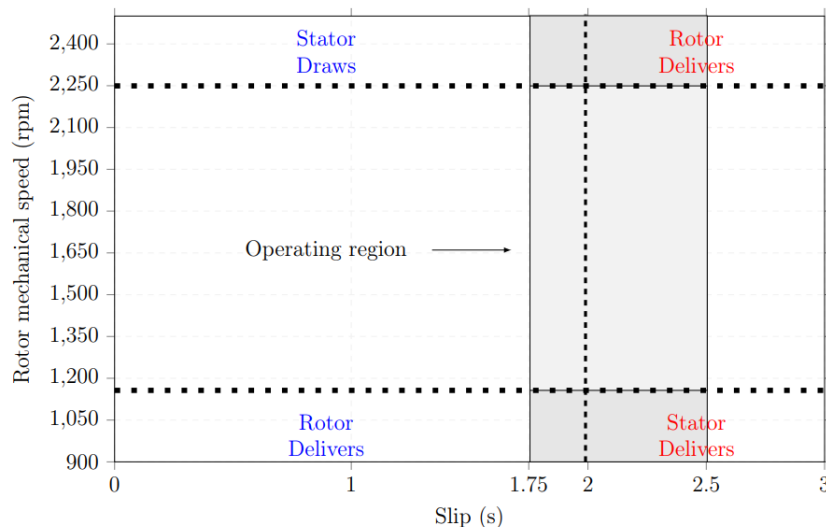


Figure D.3: The operating regions of a 4 pole, 50 Hz RDFIG, with the applied field and mechanical rotation in the same direction

with P_m being the mechanical power transferred to the rotor and P_p , P_c being the stator and rotor power respectively. Assuming that this is a loss-less machine the steady state equation for power can be further evaluated as

$$T_m \omega_m = T_{em} \omega_s + P_c \quad (D.6)$$

where T_m is the mechanical torque and T_{em} is the induced electro-mechanical torque. Assuming that the mechanical torque is equal to the electro-mechanical torque, rearranging the equation to make the subject of interest the control winding power yields

$$P_c = T_m (\omega_m - \omega_s). \quad (D.7)$$

Rearranging the expression for angular velocity, slip in Equation (D.3) gives

$$s \omega_s = \omega_s - \omega_m \quad (D.8)$$

which can be substituted into the control winding power equation to give an expression for the power as a function of slip as

$$P_c = -s P_p. \quad (D.9)$$

The equation for the power winding as a function of slip can be obtained by substituting Equation (D.5) into Equation (D.9).

$$P_p = \frac{P_m}{(1 - s)} \quad (D.10)$$

The equations are true for both the stator tied DFIG as well as the RDFIG when the mechanical rotation and rotor field is in opposite directions. When the RDFIG has the rotor magnetic field and the mechanical rotation in the same direction, Equation (D.1) becomes

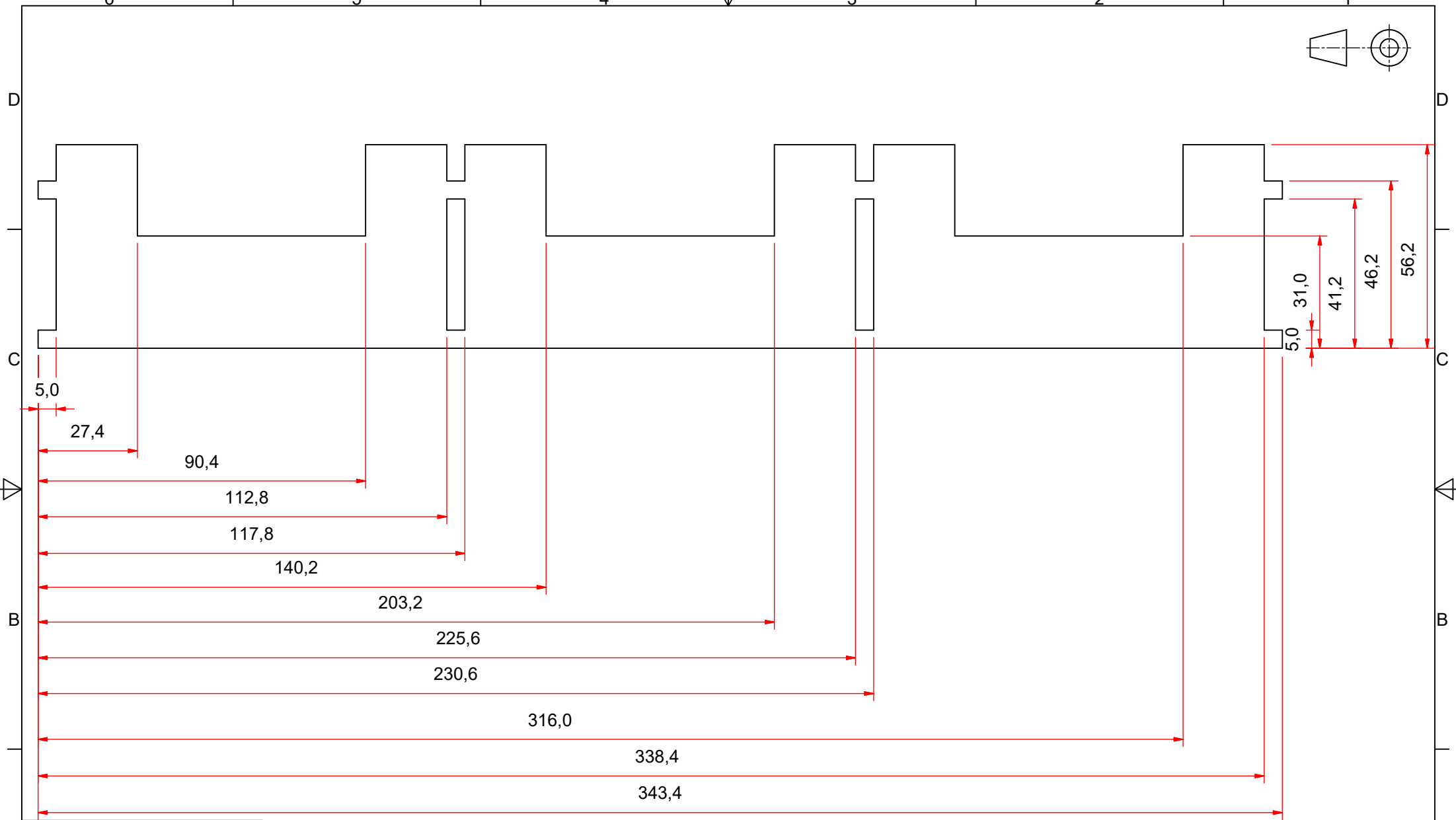
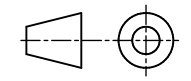
$$f_c = f_p + f_m \quad (\text{D.11})$$

and the slip at synchronous is now two as opposed to one for the stator tied.

Considering the slip regions as $\pm 30\%$ the operation of the DFIG is shown in Figure D.1 and the rotor-tied operation is shown in Figure D.2 for the mechanical speed in the opposite direction to the mechanical field and Figure D.3 for the same direction. The summarized operating regions are shown in Table 1.1.

Appendix E

Mechanical drawings



UNLESS OTHERWISE STATED
TOLERANCES $\pm 0,1$
ANGLES 0.5°

Parts List			
ITEM	DESCRIPTION	Qty.	MATERIAL / SPECIFICATIONS
1	PRIMARY LAMINATION	320	M400 - 50A ELECTRICAL STEEL
SCALE ON A3 1:1		TITLE: PRIMARY LAMINATION	
UNITS IN mm		SHEET Nr. 1 OF 1 SHEETS	
DATE 29/04/2021	Nr.		1

STELLENBOSCH UNIVERSITY

STUDENT Nr. 20012853 DRAWN BY S. BOTHA CHECKED

D

D

C

C

B

B

A

A

6

5

4

3

2

1

6

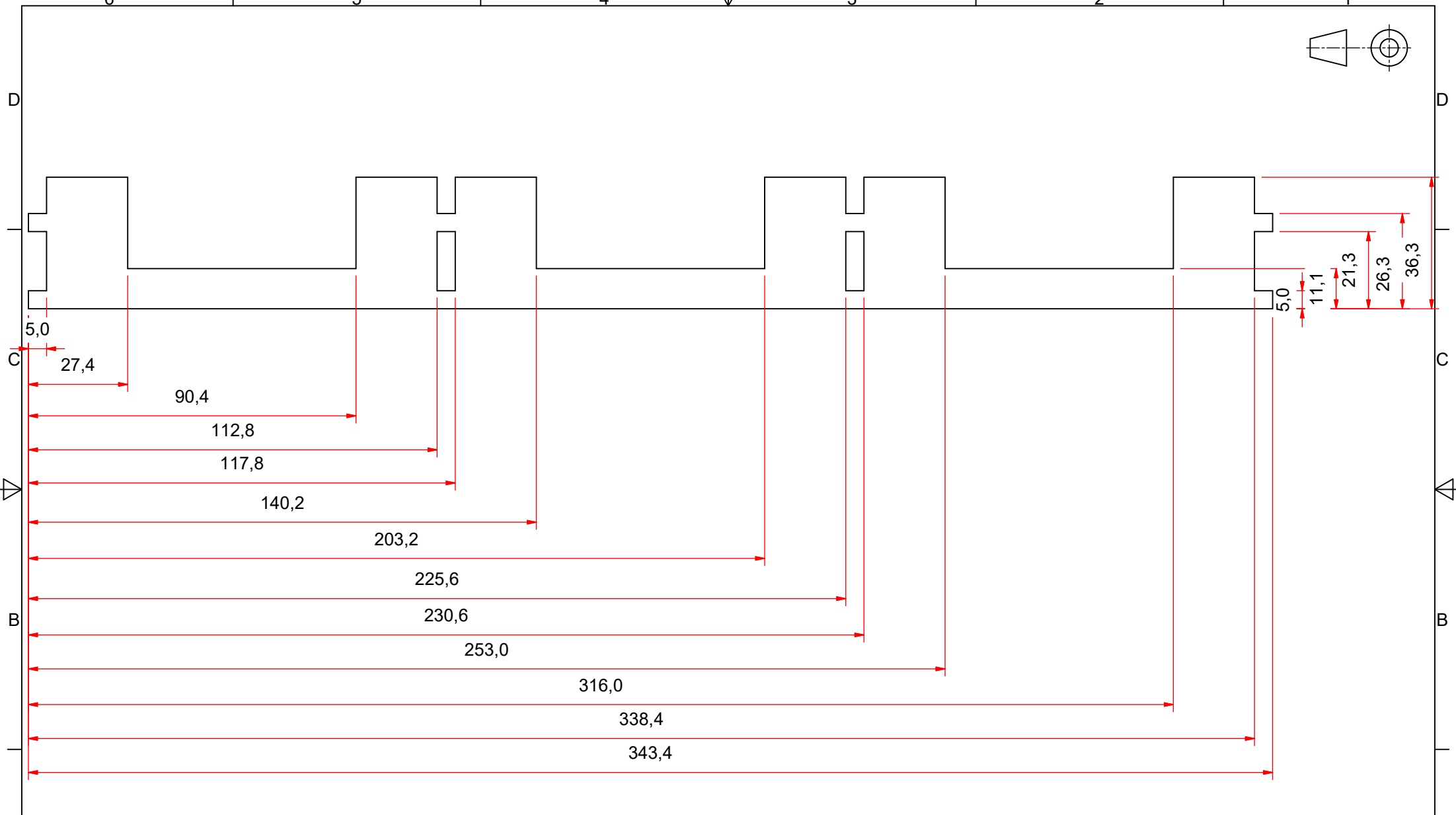
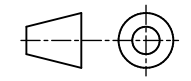
5

4

3

2

1

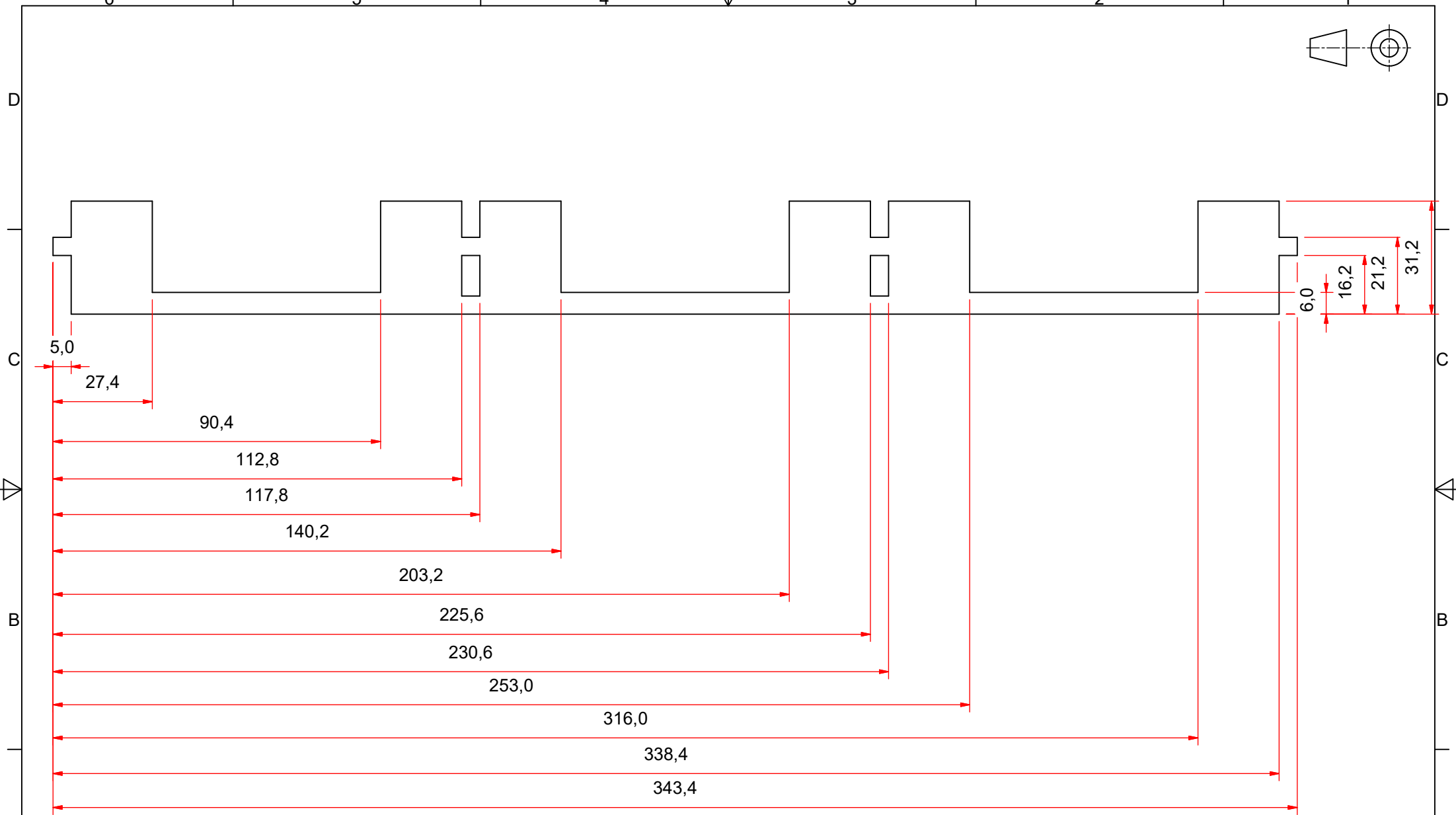
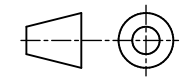


UNLESS OTHERWISE STATED
TOLERANCES $\pm 0,1$
ANGLES 0.5°

Parts List			
ITEM	DESCRIPTION	Qty.	MATERIAL / SPECIFICATIONS
1	SECONDARY LAMINATION	1020	M400 - 50A ELECTRICAL STEEL
SCALE ON A3 1:1		TITLE: SECONDARY LAMINATION	
UNITS IN mm		SHEET Nr. 1 OF 1 SHEETS	
DATE 29/04/2021	CHECKED	Nr.	1

STELLENBOSCH UNIVERSITY

STUDENT Nr. 20012853 DRAWN BY S. BOTHA CHECKED



UNLESS OTHERWISE STATED
TOLERANCES $\pm 0,1$
ANGLES 0.5°

Parts List			
ITEM	DESCRIPTION	Qty.	MATERIAL / SPECIFICATIONS
1	FILLER LAMINATION	320	M400 - 50A ELECTRICAL STEEL
SCALE ON A3 1:1		TITLE: FILLER LAMINATION	
UNITS IN mm		SHEET Nr. 1 OF 1 SHEETS	
DATE 29/04/2021	Nr.		

STELLENBOSCH UNIVERSITY

STUDENT Nr. 20012853 DRAWN BY S. BOTHA CHECKED

A

A

D

D

C

C

B

B

A

A

6

5

4

3

2

1

6

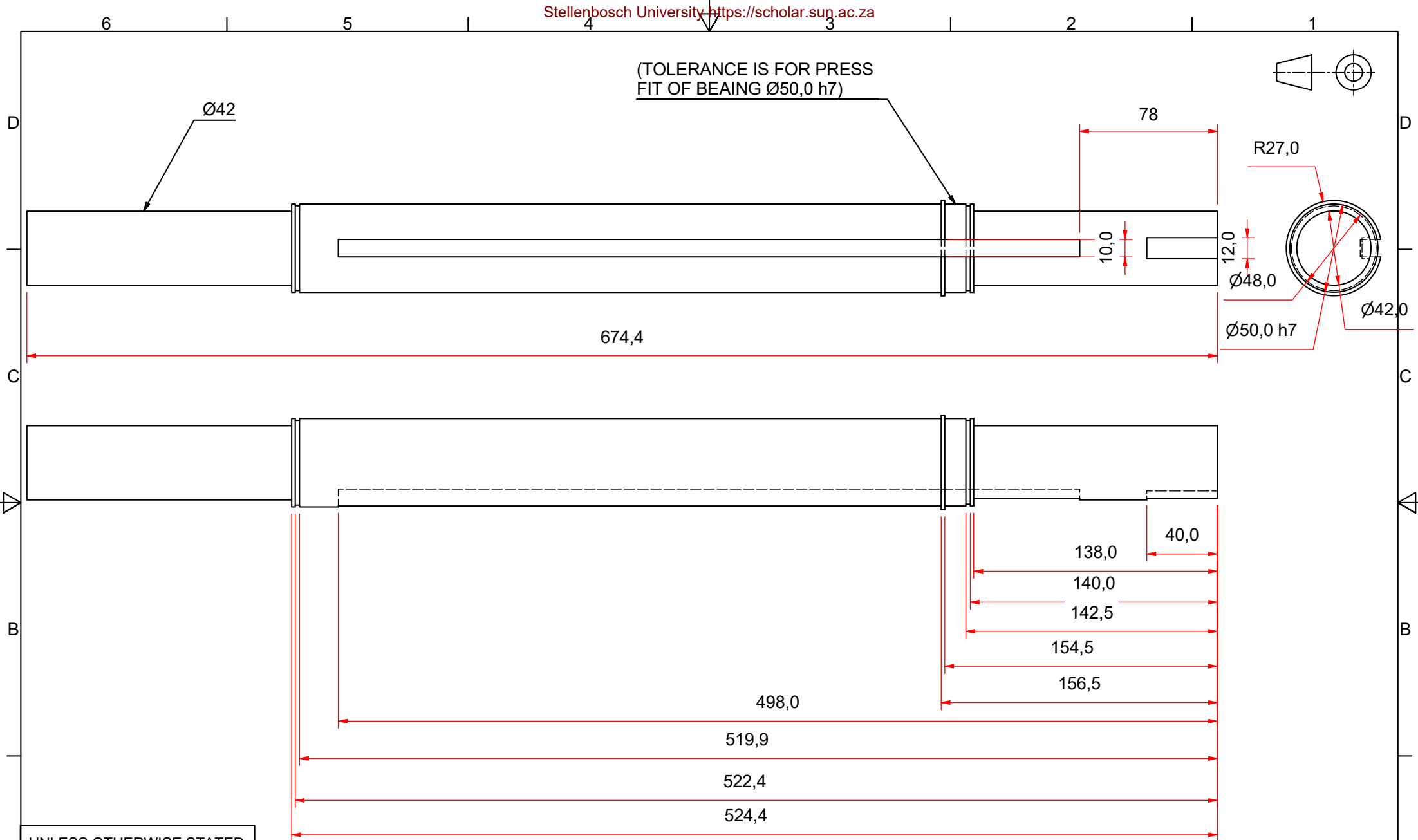
5

4

3

2

1

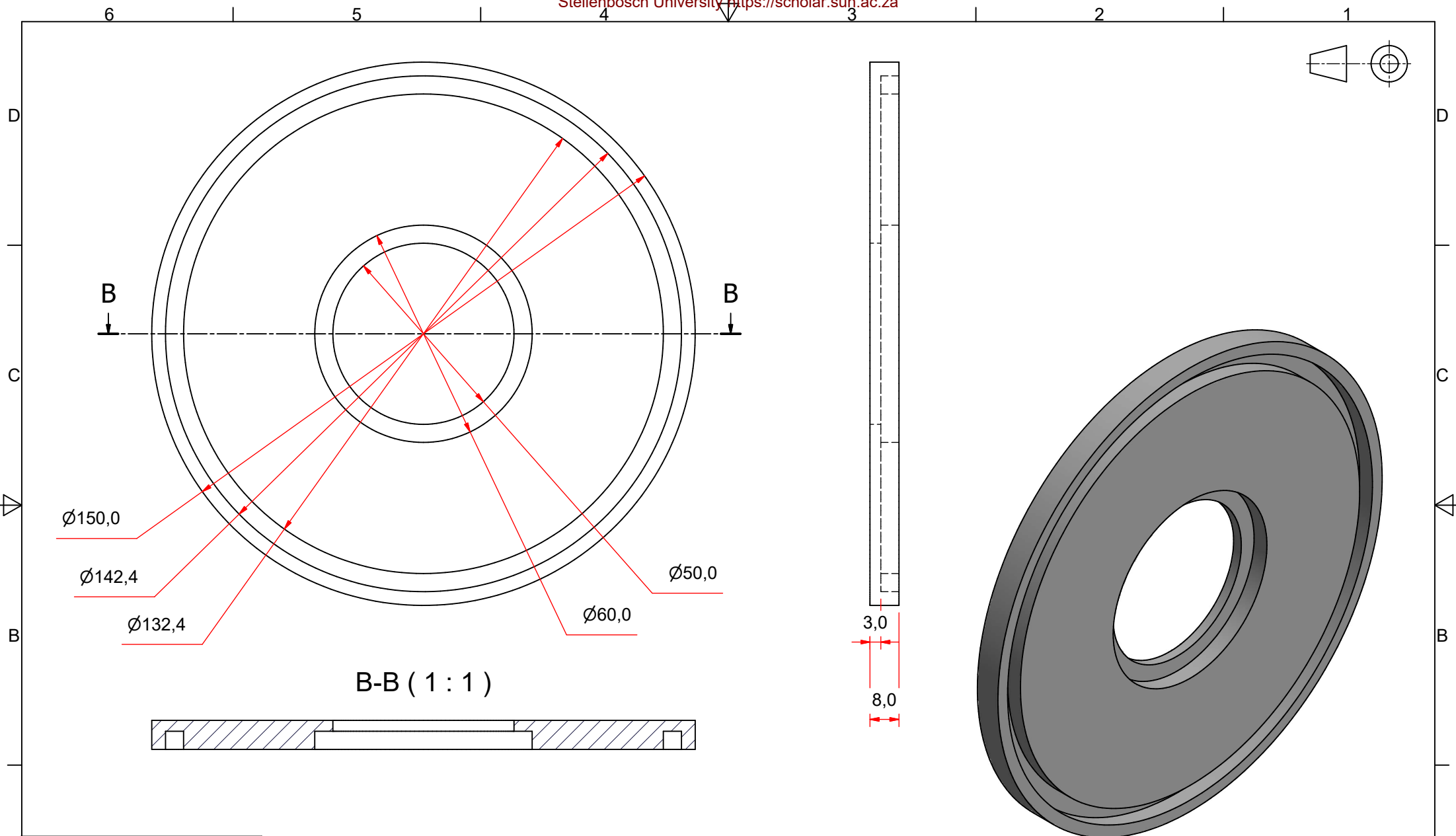
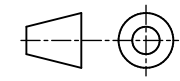


UNLESS OTHERWISE STATED
TOLERANCES ± 0,1
ANGLES 0.5°

Parts List			
ITEM	DESCRIPTION	Qty.	MATERIAL / SPECIFICATIONS
1	Ø60 x 680	1	STAINLESS STEEL
SCALE ON A3 1:2 UNITS IN mm		TITLE: SHAFT	
DATE 28/04/2021	SHEET Nr. 1 OF 1 SHEETS		Nr.

STELLENBOSCH UNIVERSITY

STUDENT Nr. 20012853 DRAWN BY S. BOTHA CHECKED

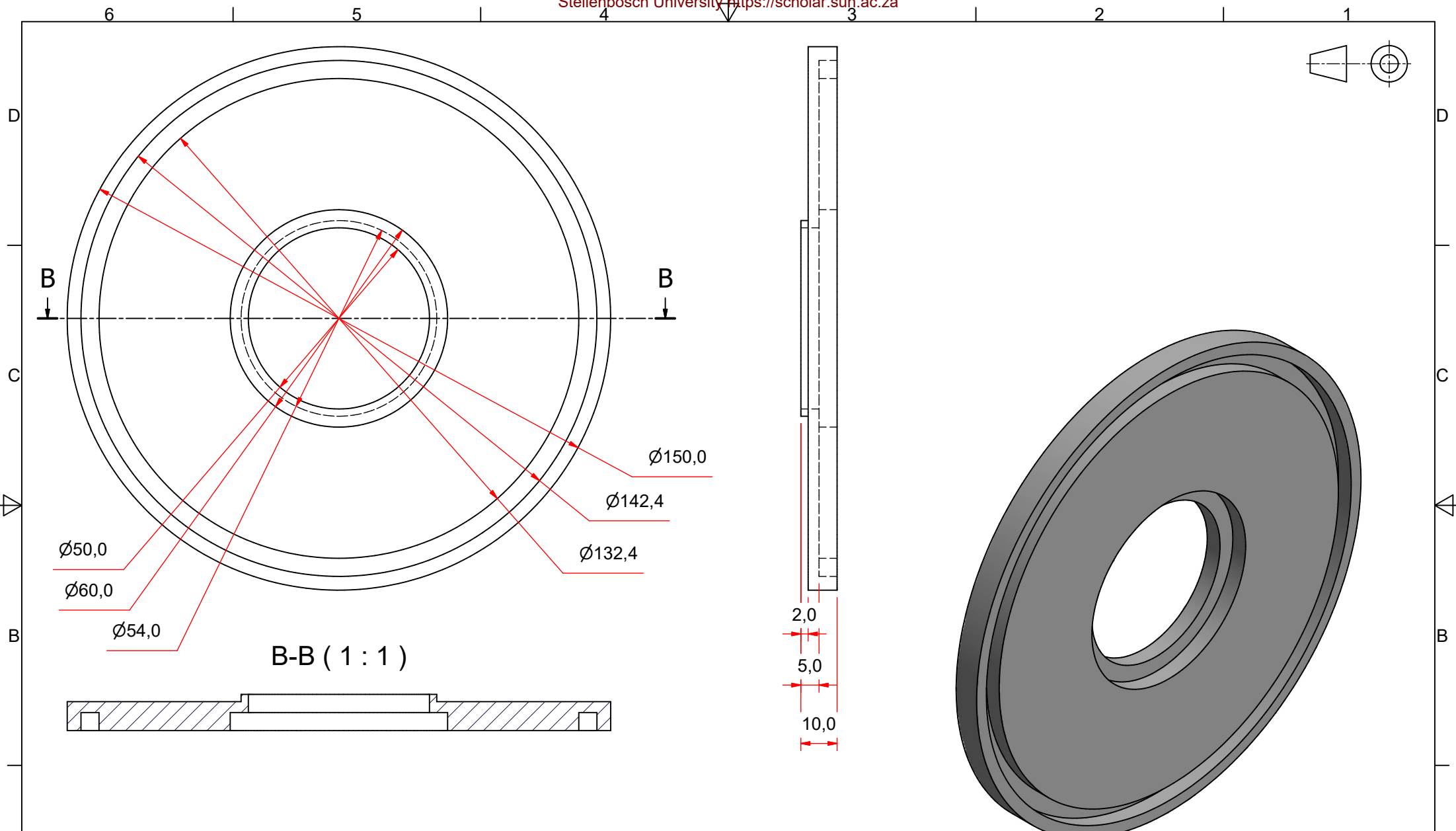


UNLESS OTHERWISE STATED
 TOLERANCES $\pm 0,1$
 ANGLES 0.5°

Parts List			
ITEM	DESCRIPTION	Qty.	MATERIAL / SPECIFICATIONS
1	Ø150 x 10	1	STAINLESS STEEL
SCALE ON A3 1:1		TITLE: PRIMARY END CAP 1	
UNITS IN mm		SHEET Nr. 1 OF 1 SHEETS	
DATE 29/09/2020	Nr.		1

STELLENBOSCH UNIVERSITY

STUDENT Nr. 20012853 DRAWN BY S. BOTHA CHECKED

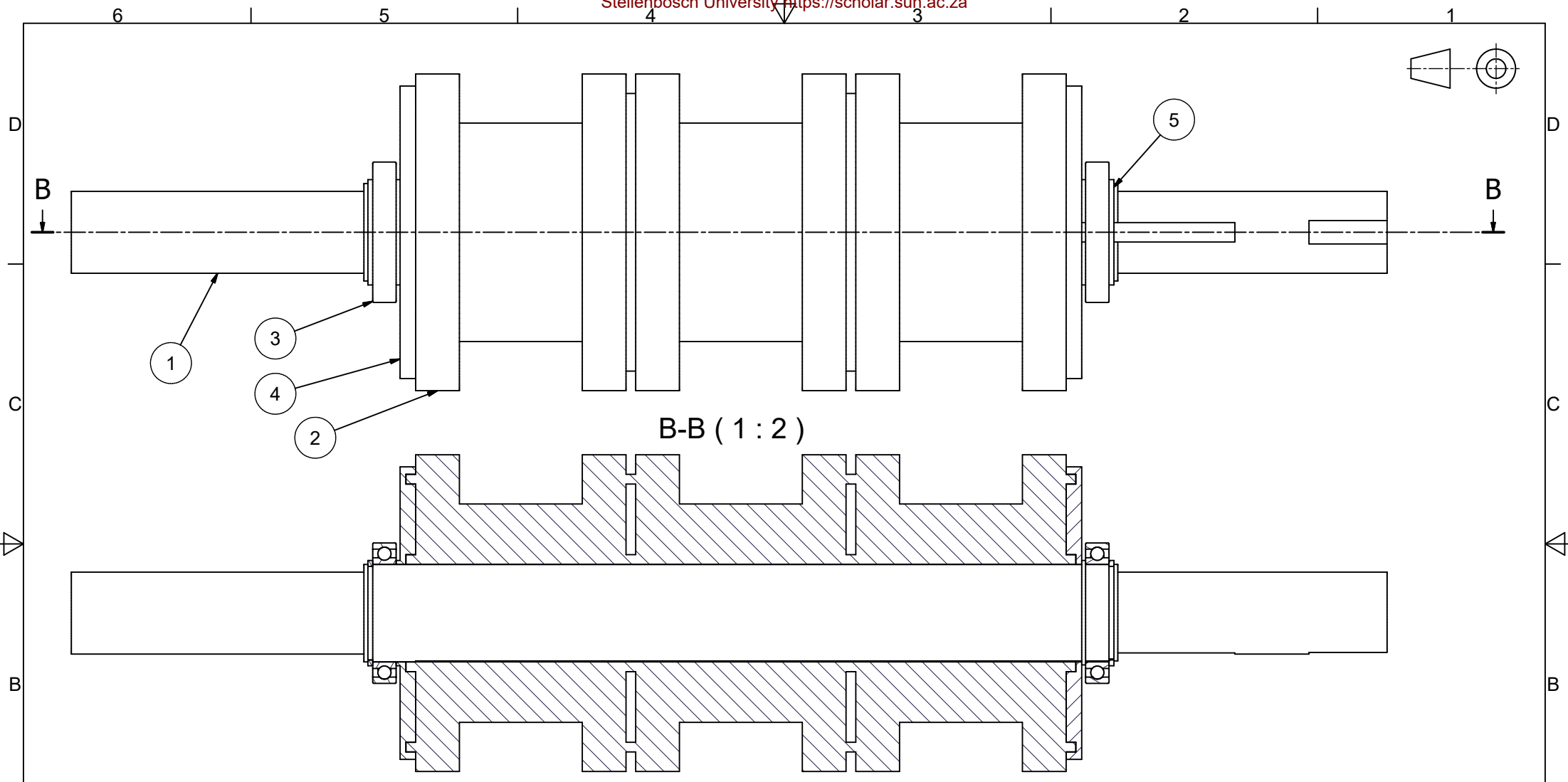


UNLESS OTHERWISE STATED
 TOLERANCES ± 0,1
 ANGLES 0.5°

Parts List			
ITEM	DESCRIPTION	Qty.	MATERIAL / SPECIFICATIONS
1	Ø150 x 10	1	STAINLESS STEEL
SCALE ON A3 1:1		TITLE: PRIMARY END CAP 2	
UNITS IN mm		SHEET Nr. 1 OF 1 SHEETS	
DATE 29/09/2020	Nr.		1

STELLENBOSCH UNIVERSITY

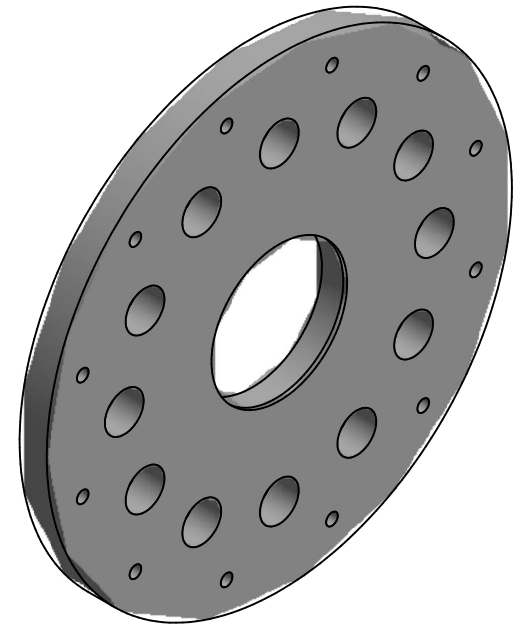
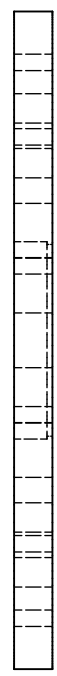
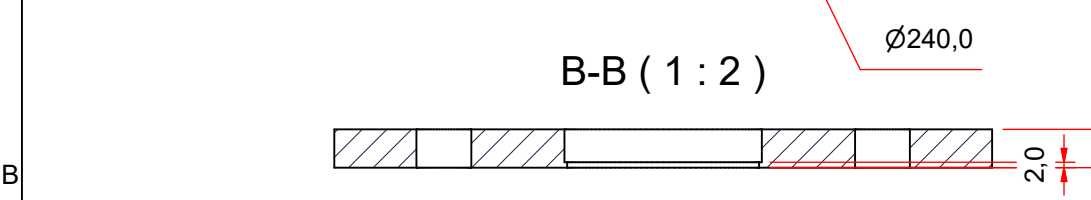
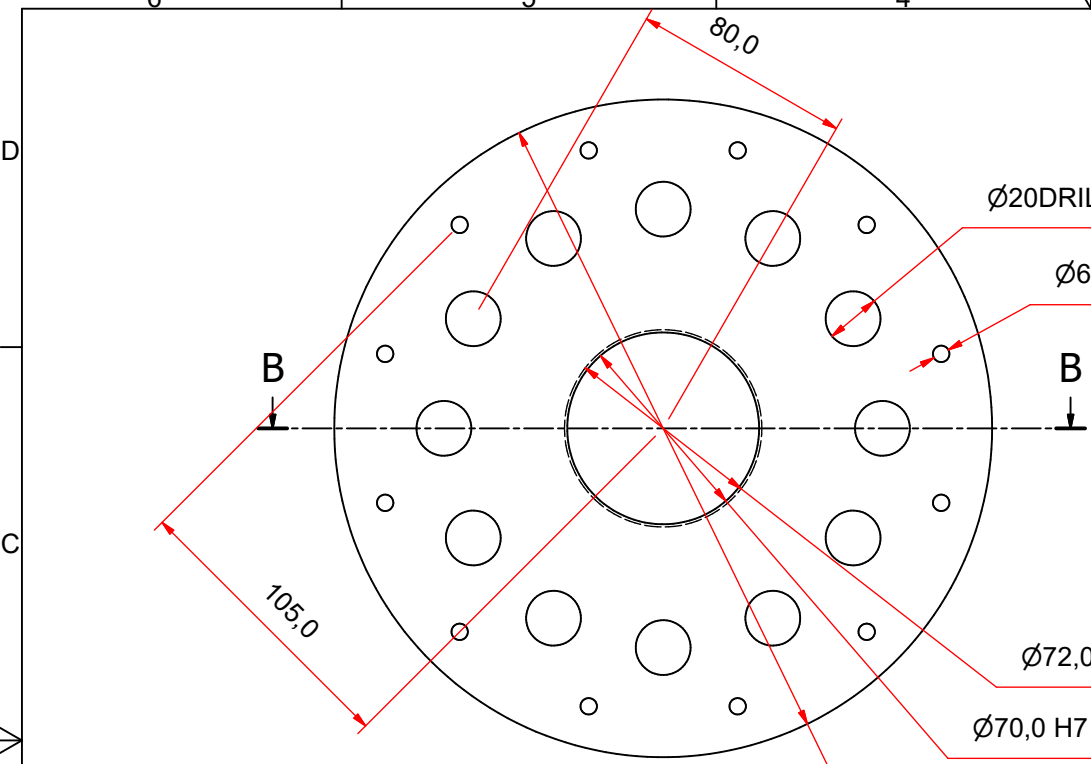
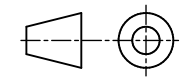
STUDENT Nr. 20012853 DRAWN BY S. BOTHA CHECKED



UNLESS OTHERWISE STATED
TOLERANCES $\pm 0,1$
ANGLES 0.5°

Parts List			
5	CIRCLIP	2	Ø48 STEEL
4	PRIMARY END CAP	2	
3	DEEP GROOVE BALL BEARING	2	SKF 61910
2	PRIMARY LAMINATION	1	
1	SHAFT	1	
ITEM	DESCRIPTION	Qty.	MATERIAL / SPECIFICATIONS

STELLENBOSCH UNIVERSITY			SCALE ON A3 1:2		TITLE: ROTATING ASSEMBLY	
			UNITS IN mm			
STUDENT Nr. 20012853	DRAWN BY S. BOTHA	CHECKED	DATE 29/09/2020	SHEET Nr. 1 OF 1 SHEETS	Nr. 1	

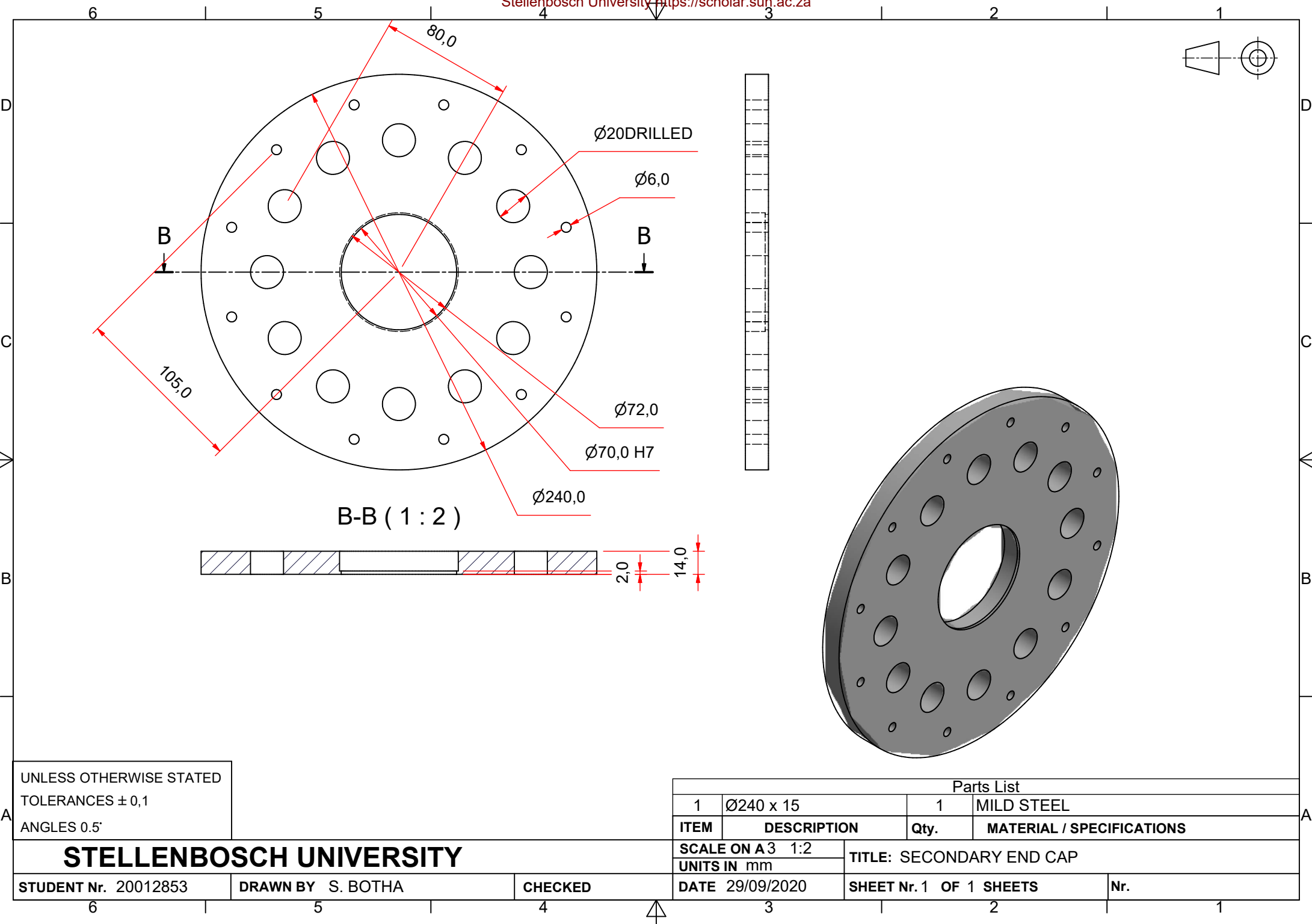


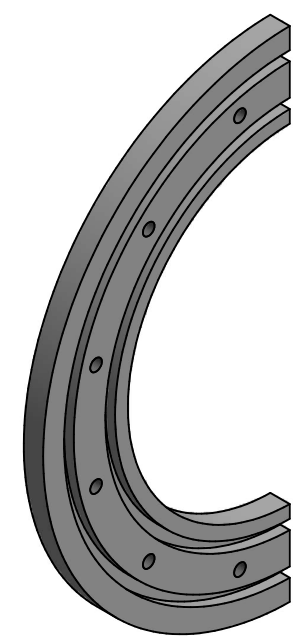
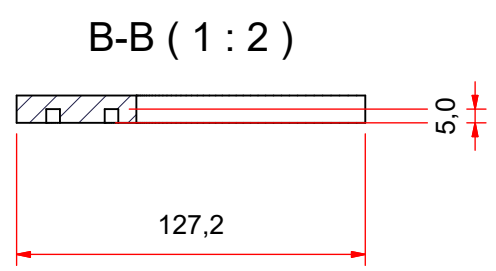
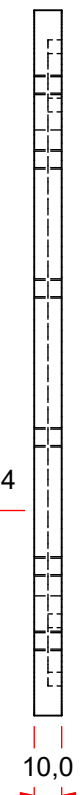
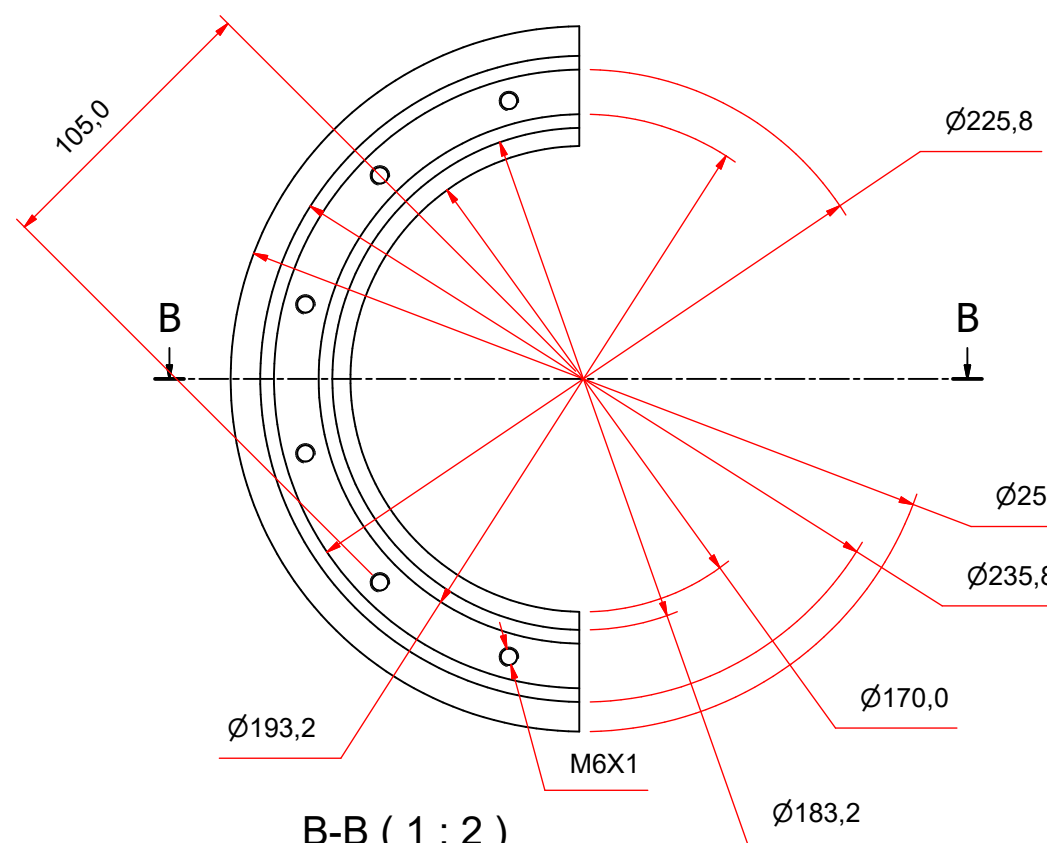
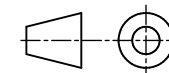
UNLESS OTHERWISE STATED
TOLERANCES $\pm 0,1$
ANGLES 0.5°

Parts List			
ITEM	DESCRIPTION	Qty.	MATERIAL / SPECIFICATIONS
1	$\varnothing 240 \times 15$	1	MILD STEEL
SCALE ON A3 1:2 UNITS IN mm		TITLE: SECONDARY END CAP	
DATE 29/09/2020	SHEET Nr. 1 OF 1 SHEETS	Nr.	

STELLENBOSCH UNIVERSITY

STUDENT Nr. 20012853 DRAWN BY S. BOTHA CHECKED





UNLESS OTHERWISE STATED
TOLERANCES $\pm 0,1$
ANGLES 0.5°

Parts List			
ITEM	DESCRIPTION	Qty.	MATERIAL / SPECIFICATIONS
1	Ø260X12	4	STAINLESS STEEL
SCALE ON A3 1:2		TITLE: SECONDARY LAMINATION HOLDER (HALF)	
UNITS IN mm		SHEET Nr. 1 OF 1 SHEETS	
DATE 29/09/2020	CHECKED	Nr.	

STELLENBOSCH UNIVERSITY

STUDENT Nr. 20012853

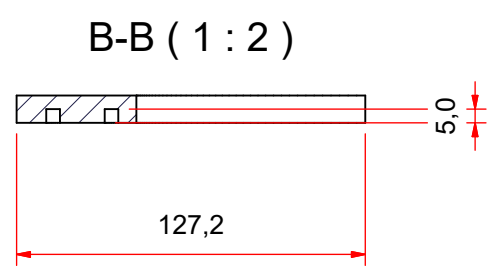
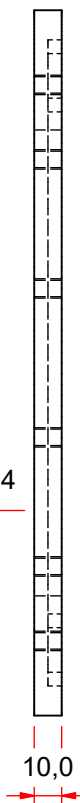
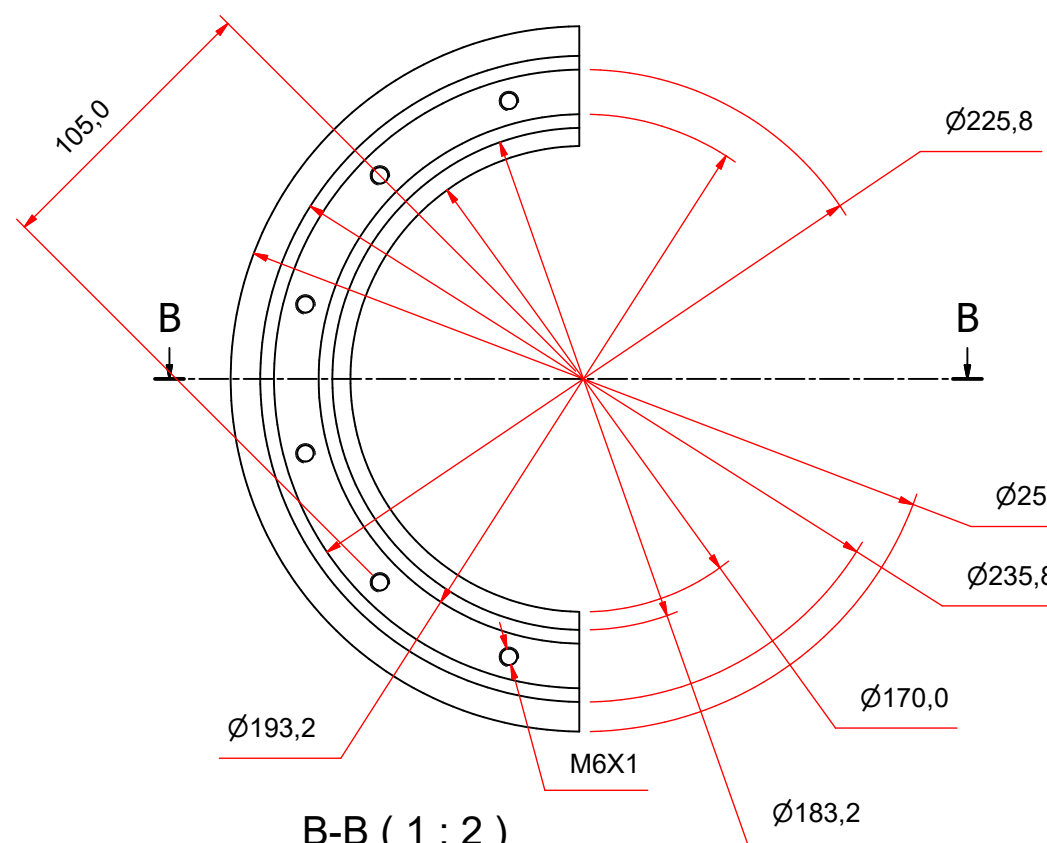
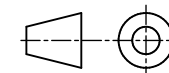
DRAWN BY S. BOTHA

CHECKED

DATE 29/09/2020

SHEET Nr. 1 OF 1 SHEETS

Nr. 1

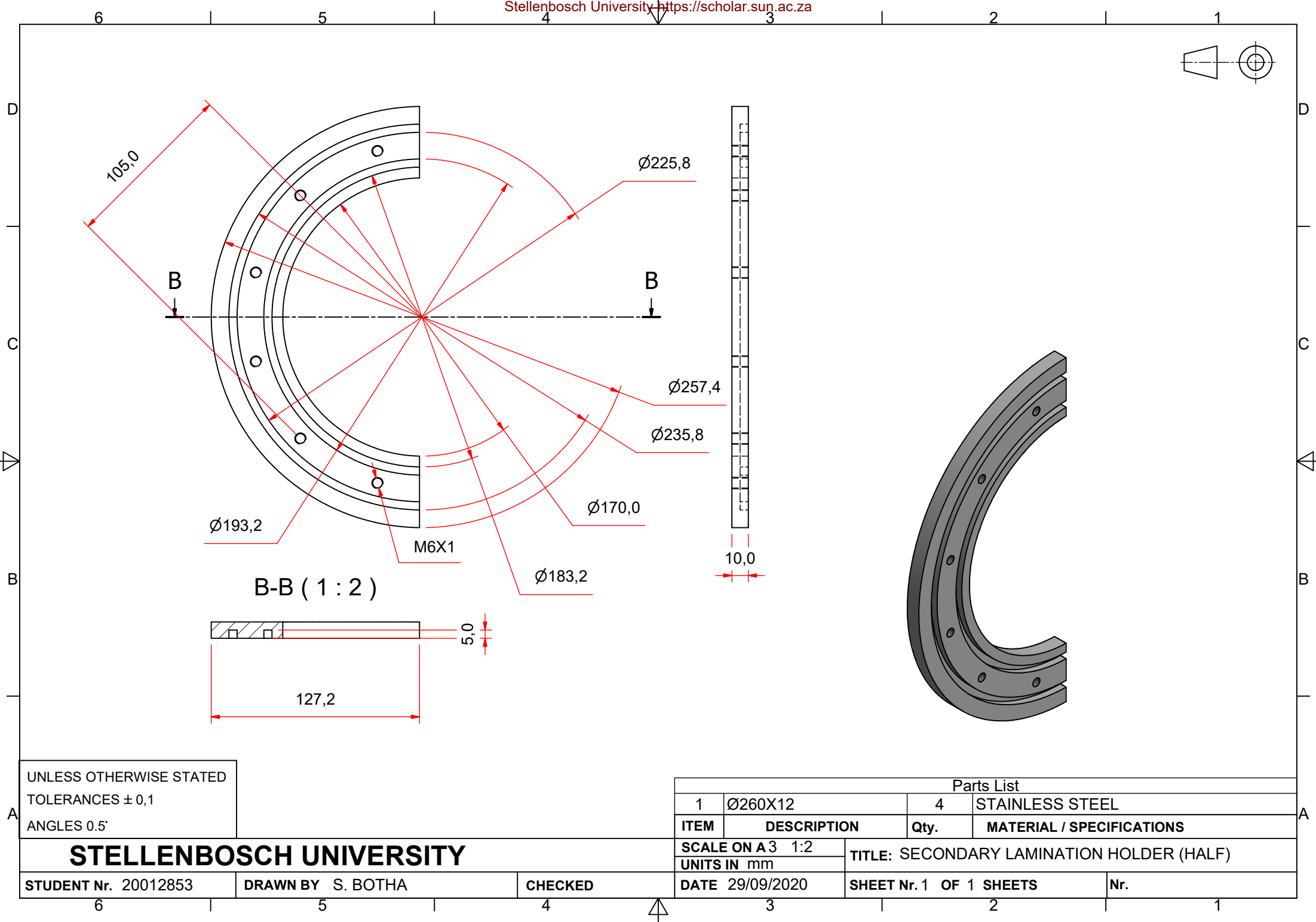


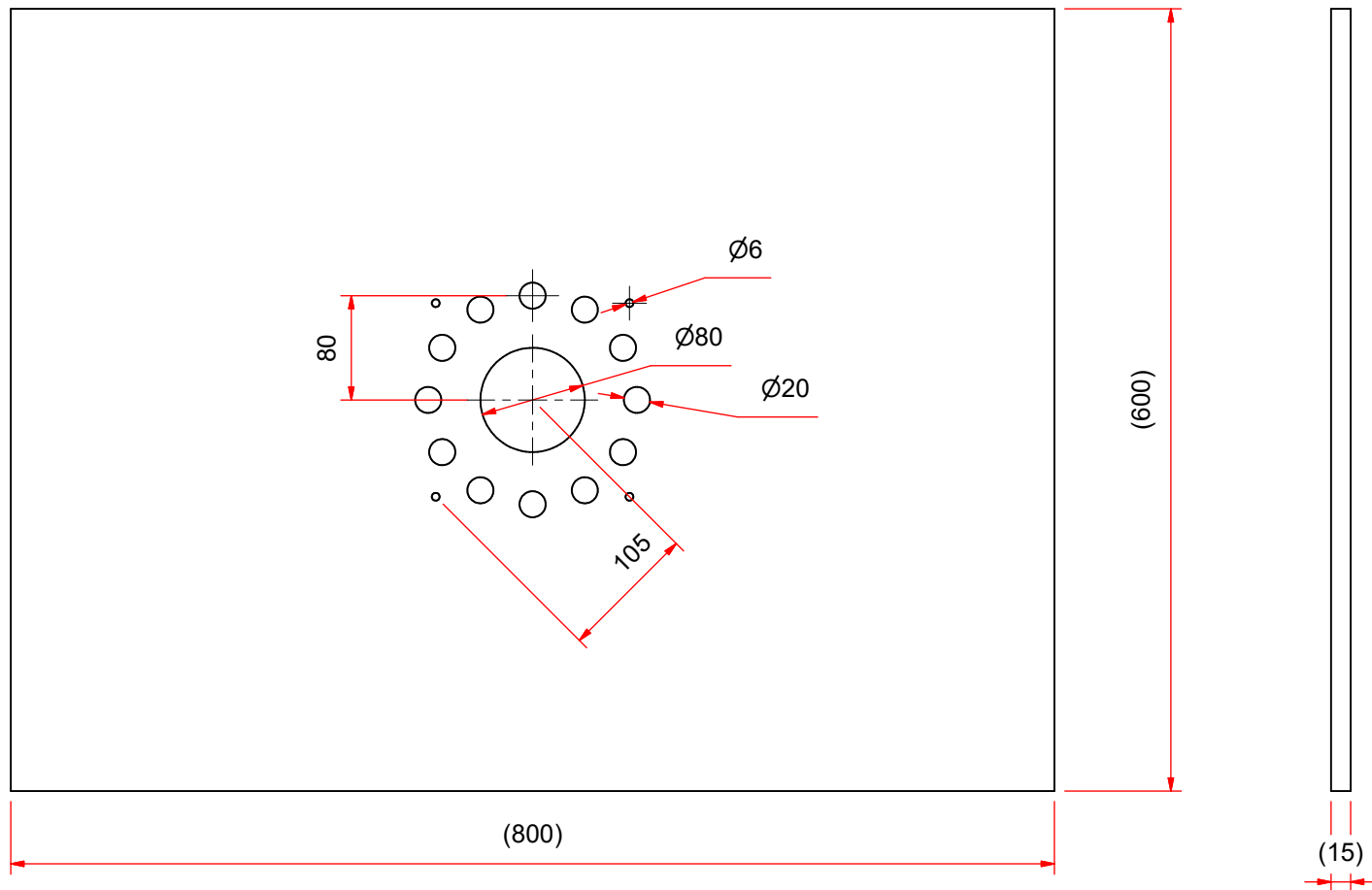
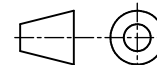
UNLESS OTHERWISE STATED
TOLERANCES $\pm 0,1$
ANGLES 0.5°

Parts List			
ITEM	DESCRIPTION	Qty.	MATERIAL / SPECIFICATIONS
1	Ø260X12	4	STAINLESS STEEL
SCALE ON A3 1:2 UNITS IN mm		TITLE: SECONDARY LAMINATION HOLDER (HALF)	
DATE 29/09/2020	SHEET Nr. 1 OF 1 SHEETS	Nr.	

STELLENBOSCH UNIVERSITY

STUDENT Nr. 20012853 DRAWN BY S. BOTHA CHECKED





UNLESS OTHERWISE STATED
TOLERANCES $\pm 0,1$
ANGLES $0,5^\circ$

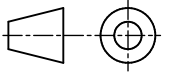
STELLENBOSCH UNIVERSITY

STUDENT Nr. 20012853

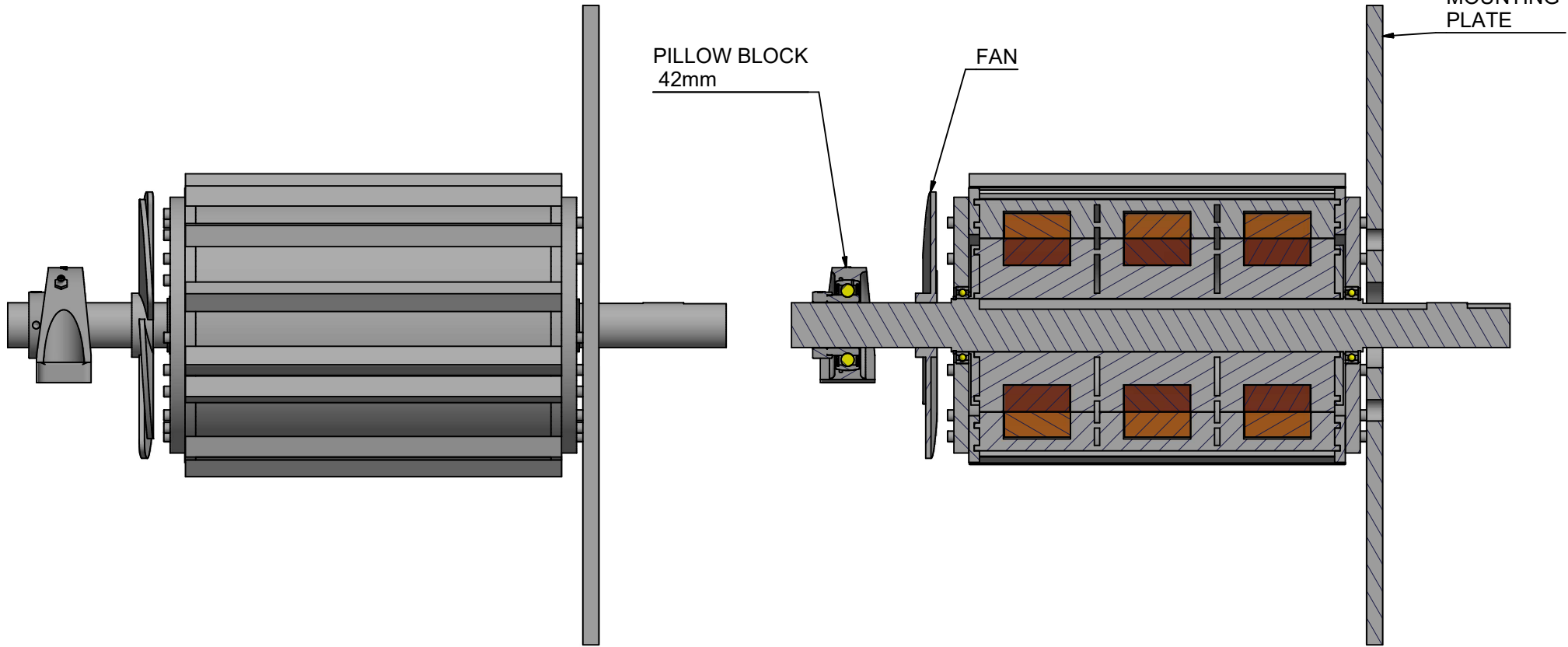
DRAWN BY S. BOTHA

CHECKED

ITEM	DESCRIPTION	Qty.	MATERIAL / SPECIFICATIONS
SCALE ON A3 1:2		TITLE: MOUNTING PLATE	
UNITS IN mm		SHEET Nr. 1 OF 1 SHEETS	
DATE 02/08/2021			Nr.



B-B (1 : 4)



UNLESS OTHERWISE STATED
TOLERANCES $\pm 0,1$
ANGLES 0.5°

ITEM	DESCRIPTION	Qty.	MATERIAL / SPECIFICATIONS
SCALE ON A3 1:4		TITLE: MOUNTING OF RT	
UNITS IN mm			
DATE 29/04/2021	SHEET Nr. 1 OF 1 SHEETS	Nr. 1	

STELLENBOSCH UNIVERSITY

STUDENT Nr. 20012853

DRAWN BY S. BOTHA

CHECKED

6

5

4

3

2

1